ALMA MATER STUDIORUM · UNIVERSITÀ DI BOLOGNA

SCUOLA DI SCIENZE
Dipartimento di Fisica e Astronomia
Corso di Laurea in Astrofisica e Cosmologia

Analytic modelling of the galactic fountain in the Milky Way potential

Tesi di Laurea Magistrale

Candidata:
Cecilia Bacchini

Relatore:
Chiar.mo Prof.
Filippo Fraternali

Correlatore:
Dott. Giuliano Iorio

Sessione II
Anno Accademico 2015-2016

A tutta la mia famiglia

Contents

Sommario

Le galassie a spirale, come la Via Lattea, sono caratterizzate dalla presenza di gas freddo e formazione stellare e vengono perciò chiamate *star-forming*. Per creare nuove stelle è necessaria una sufficiente riserva di gas, la cui disponibilità governa l'evoluzione della galassia stessa. Finora, non è stato individuato con certezza un meccanismo che possa alimentare la formazione di nuove stelle nelle galassie *star-forming*. Una delle possibili sorgenti di tale gas è l'alone galattico caldo (corona galattica) il cui raffreddamento e successivo accrescimento possono essere stimolati dal processo di *fontana galattica*. L'esplosione di supernovae porta nubi di gas freddo ($T \sim 10^4$ K) in orbita al di sopra del disco stellare; queste nubi raggiungono altezze dell'ordine del kiloparsec, interagendo con la corona di gas caldo. Il moto delle nubi all'interno di un mezzo meno denso comporta l'instaurarsi dell'instabilità di Kelvin-Helmholtz, che 'strappa' gas dalle nubi e causa la condensazione di materia coronale. Quest'ultima viene quindi accresciuta e, ricadendo sul disco, trasferisce nuovo materiale alla galassia e ne alimenta la formazione stellare. Lo scopo di questa tesi è derivare un modello analitico di fontana galattica che consenta di ottenere una formulazione analitica per il tempo orbitale, cioè il tempo richiesto alle nubi per ricadere sul disco galattico. Infatti, più tempo le nubi impiegano per attraversare il materiale coronale caldo e ricadere sul disco, più materiale viene accresciuto durante l'orbita. Conoscendo i tempi orbitali sarebbe possibile calcolare il tasso di accrescimento legato al fenomeno di fontana e studiarne l'andamento con il raggio del disco. Per prima cosa, è stato costruito un modello per l'accelerazione gravitazionale verticale nel potenziale della Via Lattea, includendo un disco stellare esponenziale e un alone di materia oscura sferico con profilo Navarro-Frenk-White. I risultati analici sono poi stati confrontati con le accelerazioni numeriche calcolate grazie al software *Galforces* in modo da verificare che i modelli analitici potessero riprodurre l'andamento di quest'ultime. Successivamente, si è costruito un modello per la fontana galattica pura: le nubi percorrono orbite balistiche all'interno di un dato potenziale, sotto l'influenza della sola gravità e senza alcun tipo di interazione con la corona. Per semplicità, il moto di queste nubi è stato studiato solamente nelle direzione perpendicolare al disco galattico. Il moto delle nubi è risultato essere descritto in modo soddisfacente da un oscillatore armonico e la semplicità di questa trattazione ha permesso di ricavare facilmente una formulazione analitica per il tempo orbitale delle nubi di fontana pura. La semplicità del modello analitico ha consentito di inserire le decelerazioni dovute alle interazioni con la corona e di ricavare una prima stima del loro effetto sul tempo orbitale. Tuttavia, un'analisi approfondita di questi casi va oltre lo scopo di questa tesi ed è lasciata a sviluppi futuri. Utilizzando il modello analitico di fontana pura, è stato possibile riprodurre con successo l'andamento dei tempi orbitali calcolati numericamente con il software *Extragas*. In conclusione, la trattazione proposta in questa tesi consente di stimare il tempo orbitale delle nubi di fontana pura dato un potenziale galattico semplice. Proprio grazie alla sua semplicità, questo modello potrebbe rivelarsi utile per lo studio del fenomeno

su tempi più lunghi, in modo da investigare l'impatto della fontana nell'evoluzione globale del disco galattico. Inoltre, il materiale coronale è caratterizzato da metallicità e momento angolare bassi ed è quindi molto differente dal gas presente nei dischi galattici. Di conseguenza, questo canale di accrescimento può assumere un ruolo chiave nell'instaurazione di moti radiali nel disco e nell'evoluzione chimica dell'intera galassia.

Chapter 1

Introduction

In this chapter we introduce the main topic of this thesis: the galactic fountain mechanism. In Section 1.1, we describe the problem of gas accretion in star-forming galaxies and some recent studies on the subject. Section 1.2 presents the observational evidence of the extra-planar gas and its connection to the galactic fountain. Section 1.3 concerns with the galactic corona and the open questions about its properties. In Section 1.4, we describe the mechanism that can trigger the accretion of coronal material. In Section 1.5, we report some examples of recent works on the evolution of galactic discs and the influence of gas accretion. Finally, Section 1.6 briefly draws an outline of the aims and the structure of this thesis.

1.1 The problem of gas accretion

The evolution of galaxies is regulated by the avaibility of cold gas, which is essential to form new stars. To date, how star-forming galaxies like the Milky Way can sustain star formation during cosmic time is still unclear. For example, it is well-know that the Milky Way star formation rate (SFR) is about 2 $\mathrm{M}_{\odot}\mathrm{yr}^{-1}$ (e.g. Misiriotis et al. 2006, Murray & Rahman 2010) and the cold gas in the inner Galactic disc would be exhausted in about 1 Gyr. On the other hand, the star formation history of our Galaxy (e.g. Cignoni et al. 2006, Aumer & Binney 2009) suggests that the SFR has been almost constant during the cosmic time. Therefore, continuous gas accretion is required to feed star formation but what is the reservoir of this gas is still unknown. The gas should be cold and, in addition, metal poor in order to conform to the results of chemical evolution models of spiral galaxies (e.g. Pagel 2009, Matteucci 2012) and to explain the observed metallicity gradients (e.g. Cavichia et al. 2014, Pezzulli & Fraternali 2016).

Over the years, several solutions have been proposed to explain the origin of this gas. Recent cosmological simulations suggest that the main accretion process for redshifts $z \gtrsim 2$ consists of filaments of cold gas which was not shock-heated to the virial temperature (Birnboim & Dekel 2003), the so-called cold flows (Kereš et al. 2009). However, this mechanism should not take place for $z \lesssim 1$ and indeed observations show that, at least in nearby galaxies, the number of intergalactic HI clouds is not sufficient to sustain the formation of new stars (e.g. Pisano et al. 2007). For many years, High Velocity Clouds (HVCs) (Figure 1.1) have been supposed to supply new cold and low-metallicity gas to the Milky Way disc. The most recent estimates suggest that this channel provides only about 0.08 $M_{\odot}yr^{-1}$ (Putman et al. 2012), which is at least one orders of magnitude lower than the Galactic star formation rate. Another channel for gas accretion could be merger events: galaxies are expected to experience a small number of major merger, mainly at high redshifts, and almost continuous minor mergers with gas rich dwarf satellites (Bond et al. 1991 and Lacey & Cole 1993). However, Di Teodoro & Fraternali (2014) found a firm upper limit for the accretion of cold gas from minor mergers in the Local Universe of 0.28 $M_{\odot}yr^{-1}$, which is an order of magnitude lower than required.

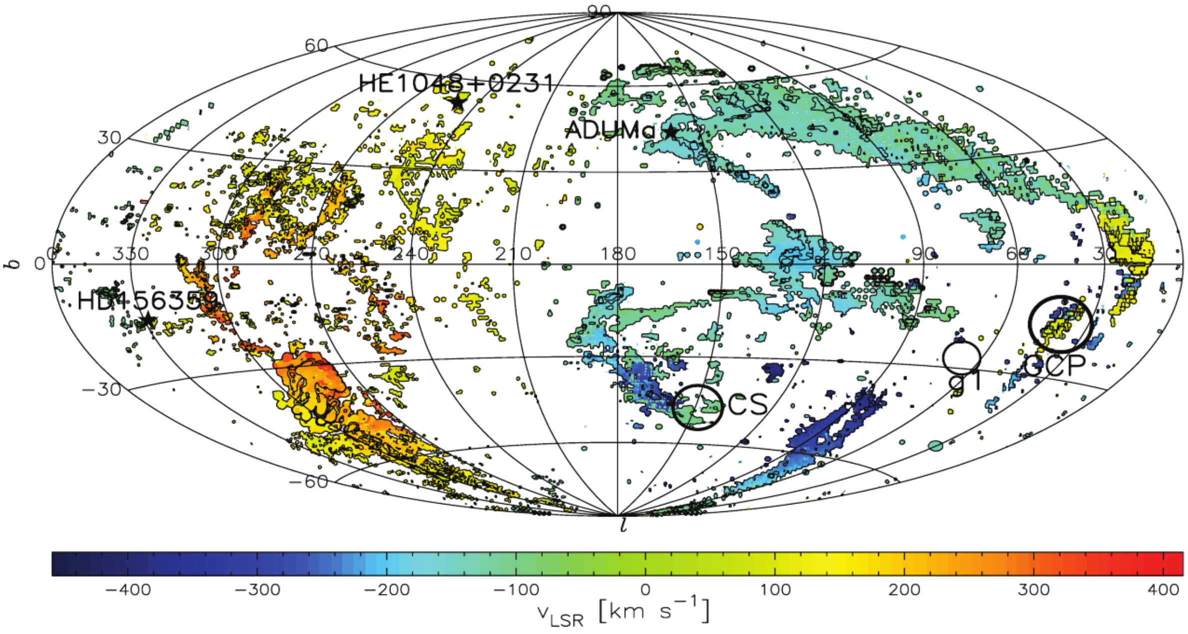

Figure 1.1: All-sky map of the High Velocity Clouds, based on the data of Hulsbosch & Wakker (1988) and Morras et al. (2000). Colors represent LSR (Local Standard Rest) velocities, as coded in the bottom bar.

As a consequence, another mechanism for gas accretion must be found in order to replenish the stock of cold gas in star-forming discs. Nearby galaxies are expected to be surrounded by cosmological hot coronae, suitable candidates for being the gas reservoir. Extended haloes of hot gas have been observed around some giant spirals (Dai et al. 2012, Anderson et al. 2016) and their mass seems to be of the order of the disc baryonic mass, contributing by 10-50 % to the missing baryons of those galaxies. Having cosmological origin (see Section 1.3), hot coronae fulfil the requirement of being metal-poor (e.g. Bogdán et al. 2013). As they are expected to be about at the virial-temperature ($T \gtrsim 10^6$ K) and rarefied, their cooling time is of the order of a gigayear in regions near the star-forming disc (e.g. Anderson & Bregman 2010). Therefore, some mechanism is needed to cool the coronal material and bring it into the disc.

In the following section, we present some observational and theoretical pieces of evidence that have helped understanding how star formation can be sustained.

1.2 Extra-planar gas and galactic fountains

Over the years, the increasing sensitivity of 21-cm observations has allowed to reveal that $\sim 10-20$ % of the neutral hydrogen in star-forming galaxies can be found a few kpc above the disc (Figure 1.2), building the so-called extra-planar gas layer (e.g Swaters et al. 1997 and Oosterloo et al. 2007). The Milky Way has extra-planar gas that includes also HVCs and Intermediate-Velocity Clouds (IVCs) (Wakker et al. 2001), which are disc-like metallicity complexes located around ~ 2 kpc from the Sun (e.g. Marasco & Fraternali 2011).

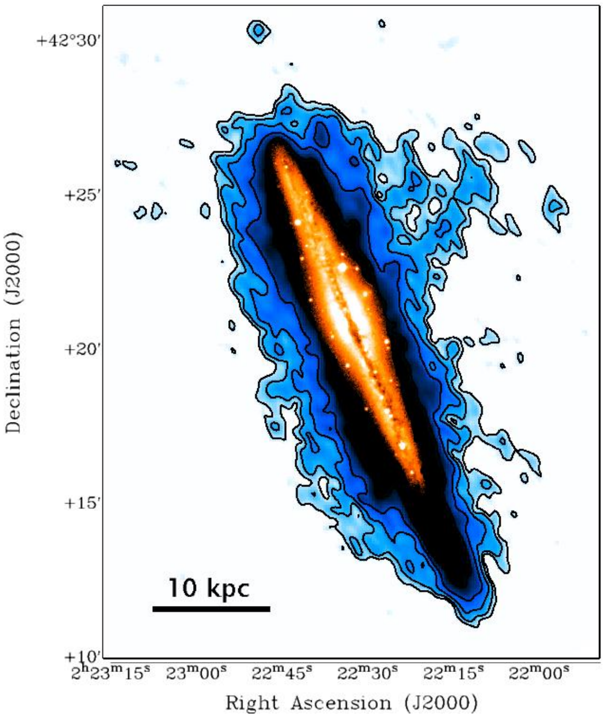

Figure 1.2: Optical DSS image (orange) and total HI map (contours + blue shade) of the edge-on galaxy NGC 891. HI contours are at $1, 2, 4, 8, 16 \times 10^{19}$ atoms cm^{-2} (Oosterloo et al. 2007).

High-sensitivity observations allowed to study the extra-planar HI distribution both in the Milky Way and in nearby galaxies and to determine its kinematical properties:

1. the extra-planar gas rotational velocity decreases in the vertical direction (e.g. Swaters et al. 1997);
2. there are vertical motions from and towards the disc (e.g. Boomsma 2007);
3. there is an overall radial inflow (e.g.Bregman 1980, Fraternali et al. 2001).

The origin of the extra-planar gas can be explained by the galactic fountain mechanism (Shapiro & Field 1976, Bregman 1980), which consists in a complex exchange of gas between the disc and the halo. In this scenario, cold gas is pushed up by stellar activity (superbubble blowout), moves through the halo and eventually falls back to the disc. Several clues support the hypothesis that the gaseous halo is due to stellar activity. Numerical simulations predict that the temperature of the majority of ejected gas in superbubble events must be much lower than the virial temperature (e.g. Melioli et al. 2009). In addition, observations of the extra-planar HI clouds, in both the Milky Way and external galaxies, have revealed that these complexes are found preferentially near the regions of high rate of star formation (Pidopryhora et al. 2007, Boomsma et al. 2008). Fraternali & Binney (2006) built a ballistic model of the galactic fountain and applied it to the observations of the HI extra-planar gas in the edge-on galaxy NGC 891 and in NGC 2403. They found that the model could reproduce the vertical distribution of the gaseous halo but not its kinematical properties because of an underestimate of the halo rotational lag with respect to the disc. However, Fraternali & Binney (2008) modified the ballistic fountain model and included the possibility for fountain clouds to sweep up low angular momentum material from the hot corona. The accretion of ambient material resolves the problems in the previous work (Figure 1.3): the clouds and the accreted coronal gas share their angular momenta, inducing a rotational lag comparable to the observed one and an inward motion of the fountain gas towards the disc. The authors found that the accretion rates needed for NGC 891 and NGC 2403 are very close to the cold gas depletion rates due to star formation.

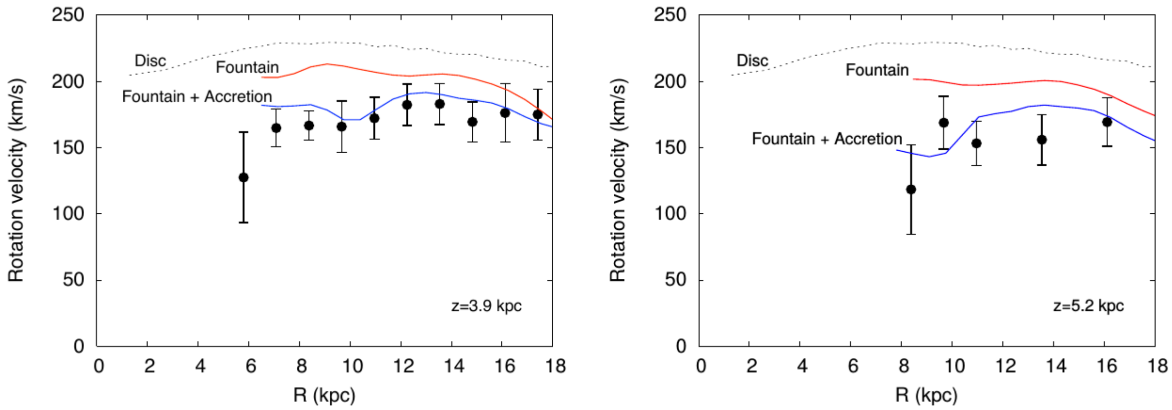

Figure 1.3: Rotational velocities (dots) obtained from the HI data at z =3.9 kpc (left panel) and z =5.2 kpc (right panel) from the plane of NGC 891 (Fraternali et al. 2005). The dotted line shows the rotation curve in the plane, while the other two curves show the azimuthal velocity predicted by the pure fountain (red) and fountain+accretion (blue) models in Fraternali & Binney (2008).

Before describing the physical phenomena which drive the interplay between the hot corona and fountain clouds, we discuss some of its physical properties.

1.3 Galactic coronae

As already mentioned, virial-temperature (T$\gtrsim 10^6$ K) cosmological coronae surround star-forming galaxies and they can extend up to hundreds of kpc from the galaxy center (e.g. Fukugita & Peebles 2006). In addition, they are expected to contain a significant fraction of the missing baryons (e.g. White & Rees 1978). Unfortunately, observing these hot haloes is quite problematic: because of their faint surface brightness, the X-ray instruments struggle to detect their extended emission (Bregman 2007) and most of the evidence is indirect. For example, Sembach et al. (2003) performed UV spectroscopy observations along lines of sight through the Galactic halo in directions toward 100 extragalactic sources, like QSOs, AGNs and BL Lac objects. They found OVI absorptions with high-velocity features, suggesting the presence of high temperature rotating corona. Putman et al. (2011), thanks to the HI Parkes All Sky Survey (HIPASS), showed that the head–tail shape of HVCs can be explained by the interaction with the diffuse halo medium, which compresses the head and creates a diffuse tail. Finally, Gatto et al. (2013) studied the ram pressure stripping of dwarf galaxies, estimating an average particle density of the corona of the Milky Way at $\mathrm{R} = 50 - 90$ kpc of $1.3 - 3.6 \times 10^{-4}\,\mathrm{cm}^{-3}$. More recently, Miller & Bregman (2015) observed OVII and OVIII emission lines from XMM-Newton/EPIC-MOS spectra, finding constrains for the mass of the hot corona: $3.8^{+0.3}_{-0.3} \times 10^9\,\mathrm{M}_\odot$ within 50 kpc and $4.3^{+0.9}_{-0.8} \times 10^{10}\,\mathrm{M}_\odot$ inside 250 kpc, accounting for $\sim 25 - 50$ % of the missing baryons of the Milky Way. They also constrained the metallicity of the hot gas, which should be $\approx 0.3\,\mathrm{Z}_\odot$ to be consistent with the pulsars dispersion measure toward the Large Magellanic Cloud. Recent observations allowed Hodges-Kluck et al. (2016) to measure the Doppler shifts of the OVII absorption-line centroids toward an ensemble of AGNs, finding a best-fit rotational velocity for the corona of 183 ± 41 km s^{-1} (assuming a rotation for the disc of 240 km s^{-1}).

The possibility that disc galaxies might be surrounded by an hot corona was first proposed by Spitzer (1956) as a medium to provide pressure confinement to the High-Velocity Clouds (Wakker & van Woerden 1997). Then, White & Rees (1978) pointed out that the hot coronae can have an important role in galactic formation: the collapse of gas onto dark matter haloes can build hot gas reservoirs through the heating by thermodynamic shocks and adiabatic compression. Alternatively, galaxies can accrete fresh gas directly from cold dense intergalactic filaments in the so-called *cold mode accretion* (Birnboim & Dekel 2003).

However, the detailed structure and kinematics of the hot coronae are still out of reach of the observations. As a consequence, only simple models have been used to interpret the data, in particular spherically symmetric hydrostatic equilibrium in the absence of rotation (e.g. Gatto et al. 2013, Miller & Bregman 2015). On the other hand, there is strong evidence suggesting that coronae should contain a large amount of angular momentum as well. Indeed, their angular momentum has a key role in the inside-out growth of star-forming discs (Pezzulli et al. 2015 and references therein). Therefore, some theoretical models of rotating hydrostatic coronae have been proposed and they belong to the following two categories (e.g. Tassoul 2000):

- Barotropic coronae: pressure depends only on density ($P = P(\rho)$) (e.g. Marinacci et al. 2011), so they are stratified on the same surfaces. These models predict that the rotational velocity does not depend on the vertical coordinate (Poincaré-Wavre theorem, e.g. Tassoul 2000). A class of barotropic models consists in polytropic models, which assume that pressure depends on the density as $P \propto \rho^{\gamma}$. In particular, isothermal profiles are described by $\gamma = 1$ while adiabatic models require $\gamma = 5/3$ (e.g. Binney et al. 2009, Nipoti 2010).

- Baroclinic models: pressure depends on density and temperature ($P = P(\rho, T)$), so P and ρ can be stratified independently (e.g. Amendt et al. 1989). For example, Barnabè et al. (2006) managed to obtain a vertical rotational velocity gradient similar to that observed in the gaseous haloes of NGC 891.

We can ask how such a hot and rarified medium can be cooled down and accreted. Originally, it was proposed that the onset of thermal instabilities in the corona could form cold clouds (e.g. Maller & Bullock 2004, Kaufmann et al. 2006). However, later works (e.g. Binney et al. 2009, Nipoti & Posti 2013) showed that spontaneous cooling and thermal instability are damped by heat conduction and buoyancy, and that cold clouds smaller than 10 kpc can form only further than 100 kpc from the disc in contradiction with the distances determined for HVCs ($\sim 5 - 20$ kpc, Wakker et al. 2001, Wakker et al. 2007). Given that the coronal material is hot and rarified, its cooling time is expected to be so large that the gas condensation is not efficient enough to feed star formation (e.g. Fukugita & Peebles 2006). As a consequence, another mechanism is required to fuel the formation of new stars.

In the following section, we present some recent results on the dynamical and hydrodynamical interaction between the cold fountain clouds and the hot corona.

1.4 Foutain-driven gas accretion

Fraternali & Binney (2006, 2008) explained the HI extra-planar distribution and kinematics by introducing the interaction between fountain clouds and the hot corona: the former accrete material from the latter and lose part of their angular momentum.

Some years later, Marinacci et al. (2010, 2011) performed a set of 2D hydrodynamical simulations in order to understand what mechanisms lie behind this interaction. They analised the motion of cold (T$\sim 10^4$ K) disc-like metallicity clouds through the hot (T $\sim 2 \times 10^6$ K) coronal medium, finding that the two gas phases blend together in a turbulent wake behind the clouds, which is created by the onset of the Kelvin-Helmholtz instability. The mixing causes the decrease of the clouds metallicity and the reduction of the corona cooling time, triggering its condensation. Therefore, the mass of the cold gas increases with time and, where they fall back onto the disc, new cold gas is accreted, being avaible for star formation.

Marasco et al. (2012) combined the model of Fraternali & Binney (2006, 2008) and the results of Marinacci et al. (2010, 2011) in order to simulate the HI emission of the Milky Way's halo, finding very good agreement between the prediction of the fountain model and the observations. In addition, they constrained the accretion rate due to fountain accretion to about 2 $M_{\odot}yr^{-1}$, which is consistent with that required to sustain the current star formation.

Recently, Armillotta et al. (2016) carried out parsec-scale hydrodynamical simulations in order to study the influence of thermal conduction in the motion of fountain clouds through the hot corona (Figure 1.4). They explored a range of coronal temperatures from 1×10^6 K to 8×10^6 K and found that this temperature plays a key role in coronal condensation. In particular, the condensation becomes less efficient for increasing virial temperature/mass of the haloes and it is completely ineffective for objects with virial masses larger than $10^{13}\,M_{\odot}$. Therefore, there could be a connection between the inefficiency of the accretion and the quenching of star formation in high-mass galaxies.

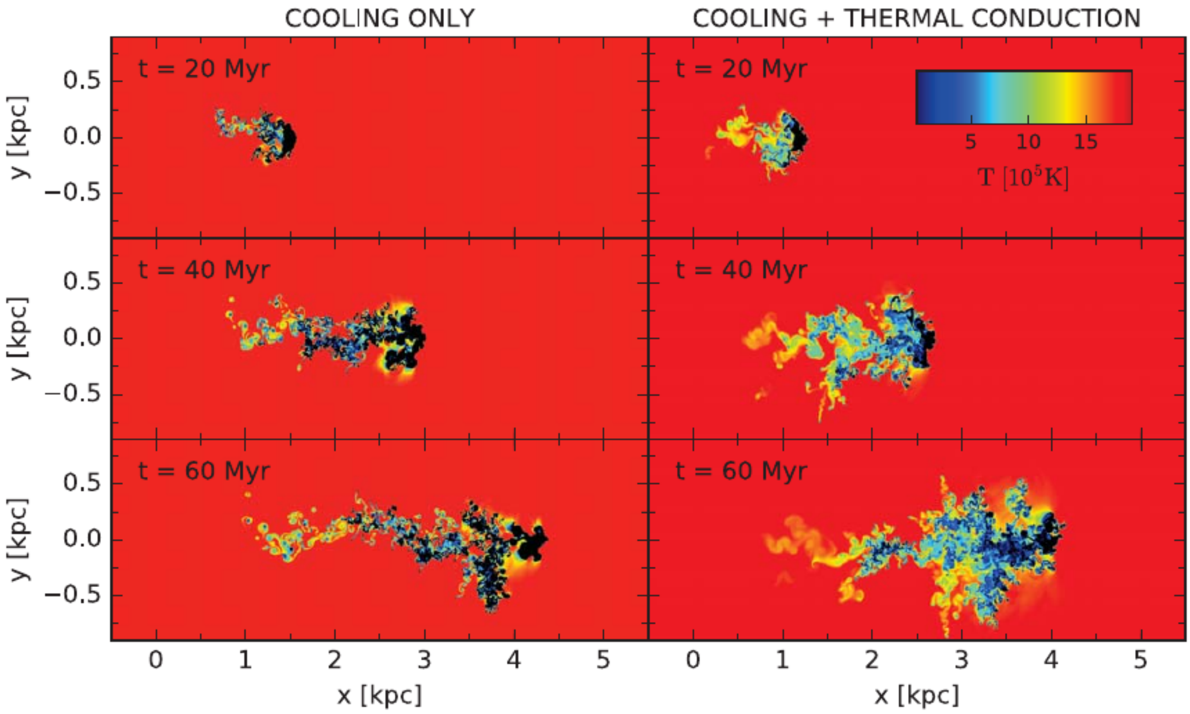

Figure 1.4: Temperature snapshot of the simulation performed by Armillotta et al. (2016) without (left panels) and with (right panels) thermal conduction. The coronal temperature is $T_{\rm cor} = 2 \times 10^6$ K and its density is $n_{\rm cor} = 10^{-3}\,{\rm cm}^{-3}$. The mass of the clouds is $M_{\rm cl} = 2.4 \times 10^4\,M_{\odot}$ and its temperature and radius are $T_{\rm cl} = 10^4$ K and 100 pc.

In conclusion, the galactic fountain can have a strong influence on the evolution of star-forming discs. Moreover, the hot coronal gas is more metal poor than the disc material, so the accretion of new gas onto the disc is expected to influence the metallicity gradients. In the following section, we outline some evolutionary models for galactic discs in order to understand the influence of gas accretion.

1.5 Modelling the evolution of galactic discs

Continuous accretion of cold and metal poor gas has a key role in the evolution of star-forming galaxies. However, observations of this process are quite challenging (Sancisi et al. 2008, Di Teodoro & Fraternali 2014), so the accretion rate and the spatial distribution of the accreting gas are still unknown, both for the Milky Way and in external galaxies. Therefore, these quantities have often to be assumed or indirectly inferred in order to build evolutionary models of discs. This is a common practice in all chemical evolution models of the Galactic disc (e.g. Mollá et al. 2016, Chiappini et al. 1997) A recent sofisticated version of these models was presented by Schönrich & Binney (2009), who built an evolving model of the Milky Way in order to study its chemical abundances throughout time. They included the evolution of stellar populations and stellar migration, obtaining a natural split of the disc in thick and thin. However, they had to assume an arbirary prescription for the distribution of the infalling material and did not include radial gas flows, which instead are expected to take place (e.g. Bilitewski & Schönrich 2012, Pezzulli & Fraternali 2016). As an alternative approach, Fraternali & Tomassetti (2012) proposed a simple method to derive the amount of gas needed for the star formation to proceed in a galactic disc, using the Kennicut-Schmidt law (Schmidt 1959, Kennicutt 1998). They found an accretion rate profile (as a function of the radius) very similar to that predicted by the fountain-driven accretion (Marasco et al. 2012) but the peak of the distribution occurs at a more internal radius. This difference could be due to the fact that their approach also neglects radial flows. Therefore, their model does not consider that the infall can take place at slightly larger radii and then move slowly inward before forming stars. The examples above point out that accretion has a significant influence on the results of disc models but it is forcedly introduced as a free parameter. Therefore, finding physical motivated 'recipes' for gas accretion is quite a desirable improvement. The aim of this thesis, which is described in the following section, can be set in this context. According to the galactic fountain model in Fraternali & Binney (2008), the longer the clouds travel through the hot corona, the larger they accrete mass. As a consequence, the orbital time of the clouds is fundamental to understand the accretion due to the fountain mechanism.

1.6 This thesis

The main purpose of this thesis is obtaining an analytical form for the orbital time of fountain clouds as a function of galactocentric radius, in a realistic galactic potential. As a first step, we analise the scenario without the interplay with the hot corona, the so-called pure fountain. In Chapter 2, we present two numerical codes: the first is *Galforces* (Fraternali & Binney 2006), which can calculate the gravitational potential given a mass distribution, and the second is *Extragas* (Marasco et al. 2012), that integrates the orbits of fountain clouds in a given galactic potential. We build a simple numerical model of a two-component (stellar disc and dark matter halo) potential for the Milky Way and we analise the shape of the vertical gravitational acceleration. Then, we study in detail the trajectories of fountain clouds in our potential and the shape of their orbits. In addition, we examine the influence of the coronal interactions on the orbits, which are implemented as in Marasco et al. (2012). In Chapter 3, we present an analytical model for the vertical acceleration of a galactic potential, aiming to reproduce the numerical trend obtained in Chapter 2. Then, we build an analytical model for the galactic fountain that allows to obtain a simple equation to calculate the orbital times, given a two-component potential. In Chapter 4, we compare the analytical orbital times and the numerical ones. Finally, Chapter 5 summarises our findings and draws some conclusions.

Chapter 2

Numerical models

In this chapter we describe the software that we employed to study fountain orbits in the Milky Way potential. Section 2.1 provides a brief explanation of *Galforces*, a dynamical code that calculates galactic potentials and accelerations given certain mass distributions. In Section 2.2, we outline the software *Extragas*, which performs integration of orbits for extra-planar gas clouds and creates a datacube of HI emission[1], and we analise the orbits of the galactic fountain.

2.1 Numerical potentials

In this section we build a numerical model of the Milky Way gravitational potential obtained using the software *Galforces* (Fraternali & Binney 2006). We are particularly interested in the Galaxy density profile, its rotation curve and vertical accelerations, which can be numerically evaluated by *Galforces*. The code relies on two main assumptions:

1. symmetry of the system with respect to the equatorial plane $z = 0$;
2. axisymmetry of the density profiles $\rho = \rho(R, z)$ (no dependence on the azimuthal angle). As a consequence, the integration is performed on a grid in the (R, z) meridional plane.

The vertical and radial gravitational accelerations are calculated as:

$$g_R = -\frac{\partial \Phi}{\partial R} \tag{2.1a}$$

$$g_z = -\frac{\partial \Phi}{\partial z} \tag{2.1b}$$

and the circular velocity is given by:

$$v_c = \sqrt{R \frac{\partial \Phi}{\partial R}} \tag{2.2}$$

---

[1] Datacubes of HI emission are not used in this thesis because our goal is to study the dynamical properties of fountain clouds (see Marasco et al. 2012 for further details)

It is possible to choose the shape (disc or spheroidal) and the number of mass components. The volume density profile of a disc component is given by:

$$\rho_{\rm disc}(R,z) = \rho_0 e^{-R/R_{\rm d}} \zeta(z/h_z) \tag{2.3}$$

where ρ_0 is the central density, $R_{\rm d}$ and h_z are the scale length and the scale height of the disc, and $\zeta(z/h_z)$ is the vertical density distribution, which can be an exponential, a gaussian or a square hyperbolic secant law. In these models, the scale height is indipendent of R. For a razor-thin disc, the potential is calculated by eq. 16 in Cuddeford (1993) and the first part of the r.h.s. of eq. 2.3 is proportional to the surface density. For a thick disc ($h_z > 0$) instead, the potential is obtained through eq. 2.170 in Binney & Tremaine (2008). The ellipsoid components in *Galforces*, suitable for bulges and dark matter haloes, have been modelled using a double-power law density profile (Dehnen & Binney 1998):

$$\rho_{\rm dpl}(R,z) = \rho_{0,{\rm dpl}} \left(\frac{m}{a}\right)^{-\gamma} \left(1 + \frac{m}{a}\right)^{\gamma-\beta} \tag{2.4}$$

where $\rho_{0,{\rm dpl}}$ is a characteristic density (it is equal to the central density if $\gamma = 0$), a is a scale length, γ and β are the inner and outer slopes respectively, and $m = \sqrt{R^2 + z^2/q^2}$ with q the axis ratio, related to the eccentricity e by $q = \sqrt{1-e^2}$. Note that when $q = 1$, m is equal to the spherical radius $r = \sqrt{R^2 + z^2}$. The potential and accelerations of the ellipsoidal components are calculated using formulae 2.125b and 2.129a in Binney & Tremaine (2008). The double power-law allows us to model matter distributions with different density profiles as reported in Table 2.1.

Table 2.1: *Galforces* double power-law profiles with different slopes.

Profiles	γ	β
Pseudo-isothermal (van Albada et al. 1985)	0	2
Modified isothermal (Binney & Tremaine 2008)	0	3
Navarro-Frenk-White (Navarro et al. 1996)	1	3
Hernquist (Hernquist 1990)	1	4
Jaffe (Jaffe 1983)	2	4
De Vaucouleurs (de Vaucouleurs 1948)	2	5

We model dark matter haloes using eq. 2.4 with (γ,β) equal to (1,3), which corresponds to a Navarro-Frenk-White (NFW) profile (see Section 2.3.1).

In order to build a simple model for the Milky Way potential, we have chosen only two mass components, a stellar disc and a dark matter halo. In fact, the stellar bulge occupies the inner parts of the Galaxy (out to 3-4 kpc) and its influence on the fountain orbits can be considered negligible. The gaseous disc significantly contributes to the potential only in the outer parts, where star formation is absent, so the fountain does not operate, and the dark matter halo potential is dominant. Therefore, we can safely neglect the effect of the gaseous disc to the overall potential.

2.1.1 The stellar disc

Galactic discs can be considered to be thin in the sense that the density falls off much faster perpendicular to the equatorial plane than in the radial direction. On the other hand, observations of the Galactic disc suggests that an accurate representation of the Milky Way disc vertical structure is obtained by superimposing two populations with densities described by a double exponential law:

$$\rho_\star(R,z) = \rho_{\star,0} e^{-\frac{R}{R_\star}} e^{-\frac{z}{z_\star}} \tag{2.5}$$

where $R_\star$ is the disc scale length and $z_\star$ is the vertical scale height. The two stellar populations form a thin disc with $z_\star \sim 300$ pc and a thick disc with $z_\star \sim 1$ kpc (Binney & Tremaine 2008). The stars of the thick disc and the thin disc differ for age, metallicity and $[\alpha/\mathrm{Fe}]$ enhancement. The surface density of the thick disc is about 10% of that of the thin one. As a consequence, we can build an approximate model of the Milky Way stellar disc by using the thin disc alone. Then, the surface brightness profile is approximately an exponential function of radius with a scale length $R_\star$ of about 2.5 kpc (e.g. McMillan 2011 and Klypin et al. 2002), and the stellar mass $M_\star$ of the Milky Way disc is about $4 \times 10^{10}\,\mathrm{M}_\odot$, so we can evaluate the central stellar surface density with:

$$\Sigma_{\star,0} = \frac{M_\star}{2\pi R_\star^2} \tag{2.6}$$

which returns $\Sigma_{\star,0} = 1.09 \times 10^9\,\mathrm{M}_\odot \mathrm{kpc}^{-2}$. With this choice, we have all the input parameters that *Galforces* needs to compute the Galactic potential, the rotation curve and the gravitational accelerations for the disc component.

Figures 2.1a and 2.1b show the disc isopotential contours and the rotation curve for our Milky Way model. The disc alone is not enough to reach a velocity of 220 km s^{-1} at solar radius because the dark matter contribution is also necessary for our Milky Way model. The circular velocity rises in the inner parts of the disc and reaches its peak at $R \approx 2R_\star$, where $v_c \approx 160$ km s^{-1} . Then, the velocity decreases because the disc density falls off at large radii.

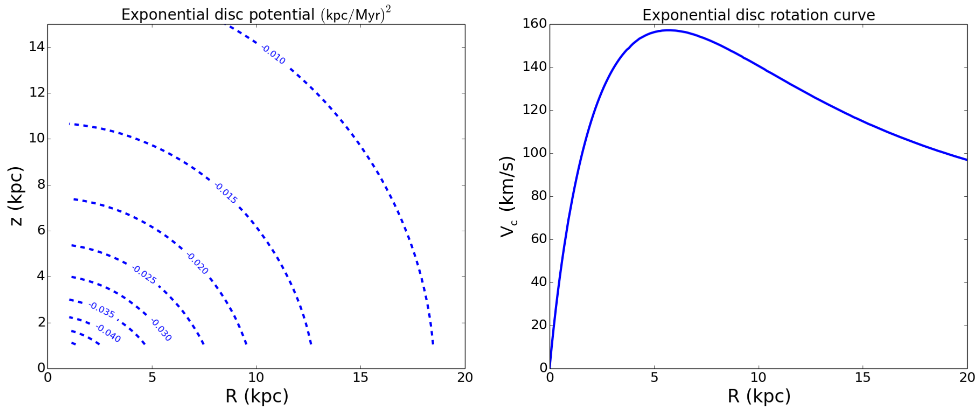

(a) Contours of the potential in units of (kpc/Myr)^2.

(b) Stellar disc rotation curve.

Figure 2.1: Gravitational potential and rotation curve for the Milky Way stellar disc adopted in this thesis (see text).

Figures 2.2a and 2.2b show the contours of the vertical and radial accelerations.

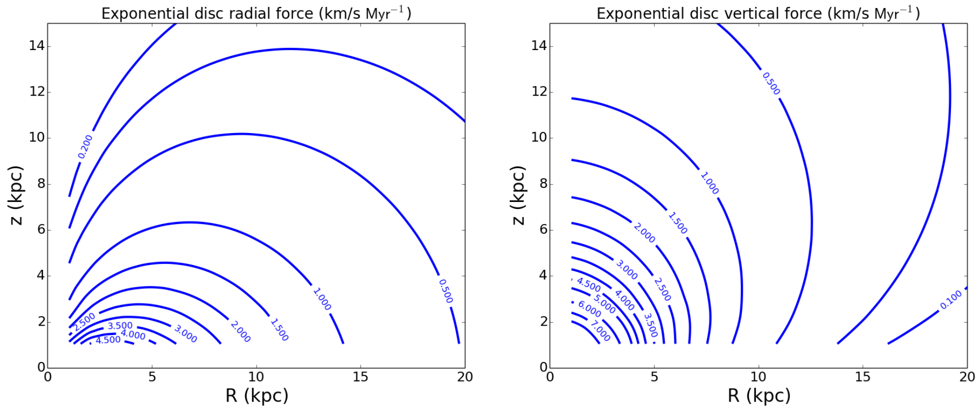

(a) Contours of the radial acceleration in units of km s^{-1} Myr^{-1}.

(b) Contours of the vertical acceleration in units of km s^{-1} Myr^{-1}.

Figure 2.2: Radial and vertical gravitational accelerations for the Milky Way stellar disc adopted in this thesis (see text).

Figure 2.3 shows how the vertical acceleration varies as a function of the distance from the midplane at four fixed radii. The gravitational pull is much stronger in the inner parts than in the outer parts. At 5 kpc the vertical acceleration has a clear peak, while beyond ~10 kpc it tends to becomes approximately constant at a certain height, which depends on the radius. For example, the acceleration at $R = 15$ kpc flattens from $z \approx 5$ kpc to $z \approx 25$ kpc while its variation with z is still evident at $R = 10$ kpc.

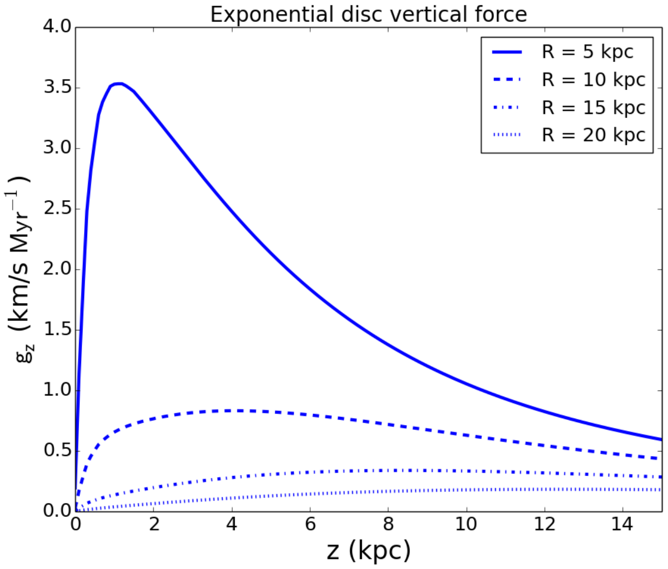

Figure 2.3: Vertical acceleration as a function of z at fixed radii for the Milky Way stellar disc adopted in this thesis (see text).

2.1.2 The dark matter halo

The dark matter halo is the least well understood of the Galaxy's components. We have only indirect constraints on its shape, size, mass and local density. Between 1995 and 1997 Navarro, Frenk and White (Navarro et al. 1996) performed a series of N-body collisionless simulations in order to study the density distribution of dark matter in the Cold Dark Matter (CDM) cosmology scenario. They showed that the haloes density profile is well approximated by the so-called Navarro-Frenk-White (NFW) law. Therefore, we built a numerical model for the halo potential by assuming spherical shape and NFW profile using eq. 2.4 (see Table 2.1). Several observations obtained using HI and other kinematics tracers suggest that the circular velocity of the Milky Way is about 220 km s^{-1} at the Solar radius and that the rotation curve remains flat at 220 km s^{-1} at least out to $\sim$ 25 kpc. The circular velocity due to the disc potential is not enough to reproduce these observations, so it is necessary to introduce the dark matter halo contribution.

In our simple two-component model, the total circular velocity at each radius results from the quadratic sum of the disc ($v_{c,\star}$) and the halo ($v_{c,\mathrm{DM}}$) contributions, so:

$$v_{c,\mathrm{DM}}(R) = \sqrt{v_{c,\mathrm{tot}}(R)^2 - v_{c,\star}(R)^2} \tag{2.7}$$

For our Milky Way model, the disc contribution to the circular velocity is 148.6 km s^{-1} at R = 8.5 kpc (see Figure 2.1b), so the halo one must be 162.2 km s^{-1} in order to reach 220 km s^{-1} . The gravitational attraction of a spherical density distribution on a unit mass at a given radius r is entirely determined by the mass interior to r (Binney & Tremaine 2008):

$$\vec{F}(r) = \frac{GM(r)}{r^2}\hat{e}_r \tag{2.8}$$

For a spherical halo, we may readily evaluate $v_{c,\mathrm{DM}}$ by equating the gravitational attraction $|\vec{F}|$ to the centripetal acceleration v_c^2/r:

$$v_c^2(r) = |\vec{F}|r = \frac{GM(r)}{r} \tag{2.9}$$

As a result, the halo mass inside $R_\odot$ is:

$$M_{\mathrm{DM}}(r < R_\odot) = \frac{R_\odot v_c^2(R_\odot)}{G} = 5.2 \times 10^{10}\,\mathrm{M}_\odot\,. \tag{2.10}$$

According to Binney & Tremaine (2008), the halo mass inside a given radius is given by:

$$M_{\mathrm{DM}}(r) = 4\pi G\rho_{0,\mathrm{DM}} r_s^3 \int_0^{r/r_s} \frac{x}{(1+x)^2}dx = 4\pi G\rho_{0,\mathrm{DM}} r_s^3 \left[\ln(1+x) - \frac{x}{1+x}\right] \tag{2.11}$$

where r_{s} is the halo scale length, x is the ratio of r to r_s and $\rho_{0,\mathrm{DM}}$ is the halo characteristic density. We assume a scale length of 21.5 kpc according to Klypin et al. (2002), so $\rho_{0,\mathrm{DM}}$ can be calculated by inverting eq. 2.11 and using M_{DM} from eq. 2.10 [2]. The resultant characteristic density is $8.33 \times 10^6\,\mathrm{M}_\odot\mathrm{kpc}^{-3}$. At this point, we use *Galforces* to numerically evaluate the potential (Figure 2.4a), the rotation curve (Figure 2.4b) and the gravitational accelerations of the dark matter halo. Like the stellar disc (see Section 2.1.1), the halo alone does not reach 220 km s^{-1} at the Solar radius but the rotation curve keeps on rising out to 25 kpc.

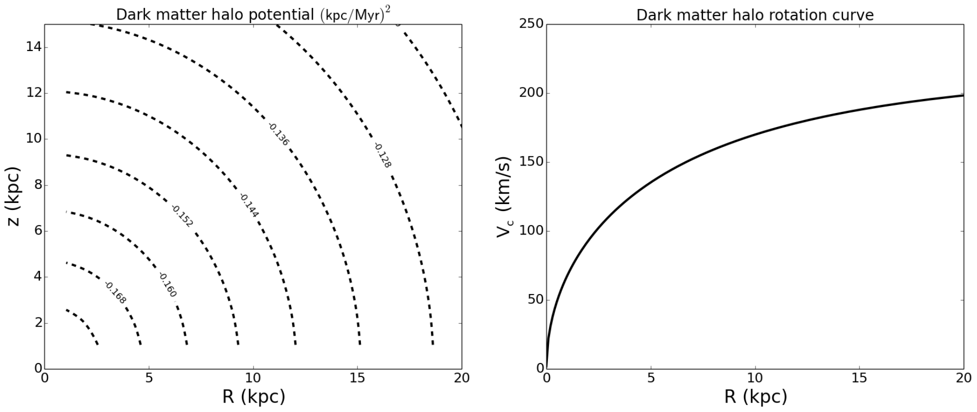

(a) Contours of the potential in units of $(\mathrm{kpc/Myr})^2$.

(b) Dark matter halo rotation curve.

Figure 2.4: Gravitational potential and rotation curve for the Milky Way dark matter halo (see text).

Figures 2.5b and 2.5a illustrate the contours of the vertical and radial accelerations due to the halo potential.

---

[2] Klypin et al. (2002) built a model of the Milky Way which includes also the bulge contribution. Our model with the stellar disc and the dark matter halo must reproduce the same rotation curve without the bulge component, so the halo central density must be slighly different.

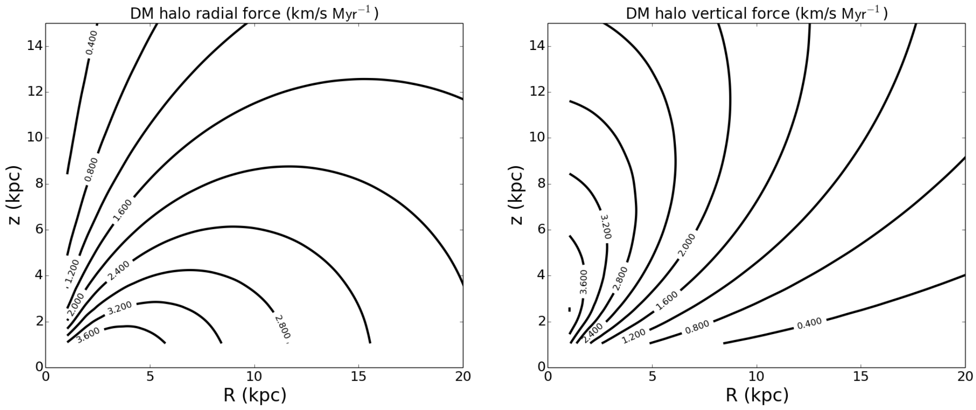

(a) Contours of the radial acceleration in units of km s^{-1} Myr^{-1}.

(b) Contours of the vertical acceleration in units of km s^{-1} Myr^{-1}.

Figure 2.5: Gravitational accelerations for the dark matter halo adopted in this thesis (see text).

The vertical profile of the gravitational pull $_z$ is shown in Figure 2.6. This acceleration is larger in the central regions but falls with radius much more gently than the acceleration of the disc alone (Figure 2.6) and it becomes less and less strong as we consider greater radii. Note that, at fixed radius, g_z linearly grows with z up to a certain height, which depends on the radius considered for the analysis. For example, the acceleration at $R = 5$ kpc is linear up to $z \approx 3$ kpc, while at $R = 10$ kpc the trend does not change until $z \approx 5$ kpc. After reaching its peak, the downward pull slighly decreases as the distance from the midplane grows. This linear trend of the vertical acceleration is of crucial importance for the analytic model of the galactic fountain that we describe in Chapter 3.

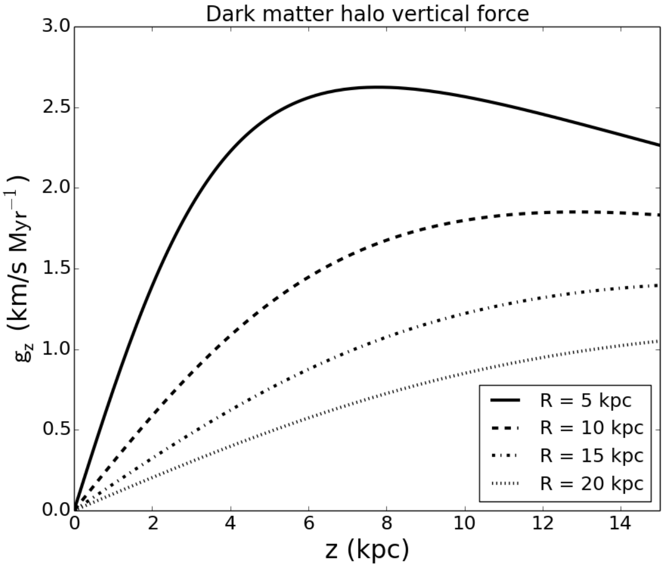

Figure 2.6: Vertical acceleration as a function of z at fixed radii for the dark matter halo adopted in this thesis (see text).

2.1.3 Two-component model

In the previous sections, we have derived the parameters of the single mass components, here we can build a two-component numerical model and evaluate its potential, its vertical and radial accelerations and its rotation curve with *Galforces*. To this end, we have chosen an exponential stellar disc and a spherical NFW halo as described in Sections 2.1.1 and 2.1.2 respectively. The parameters of each mass component are summarised in Table 2.2.

Table 2.2: Milky Way model: parameters for each mass component. The total mass of the Galaxy is $\mathrm{M_{tot}} \approx 1.68 \times 10^{12}\,\mathrm{M_\odot}$ and the circular velocity at the Solar radius is $v_c(R_\odot) \approx 220\,\mathrm{km\ s^{-1}}$.

Exponential stellar disc		Dark matter halo (NFW)	
$\mathrm{M}_\star$	$4 \times 10^{10}\,\mathrm{M_\odot}$	$\mathrm{M_{DM}}$	$1.64 \times 10^{12}\,\mathrm{M_\odot}$
$R_\star$	2.5 kpc	R_s	21.5 kpc
Σ_0	$1.02 \times 10^9\,\mathrm{M_\odot kpc^{-2}}$	ρ_0	$1.2 \times 10^9\,\mathrm{M_\odot kpc^{-3}}$
Vertical distribution	exp	Shape	spherical
h_z	0.3 kpc	c	11.3
$v_c(R_\odot)$	148.6 $\mathrm{km\ s^{-1}}$	$v_c(R_\odot)$	162.2 $\mathrm{km\ s^{-1}}$

Figures 2.7a and 2.7b show the total potential and the rotation curve respectively. Note that the disc is the dominant contributor to the circular velocity up to $R \sim 9$ kpc, while v_c at large radii is dominated by the dark matter distribution. As a whole, the rotation curve is flat at 220 $\mathrm{km\ s^{-1}}$ from 5 to 25 kpc.

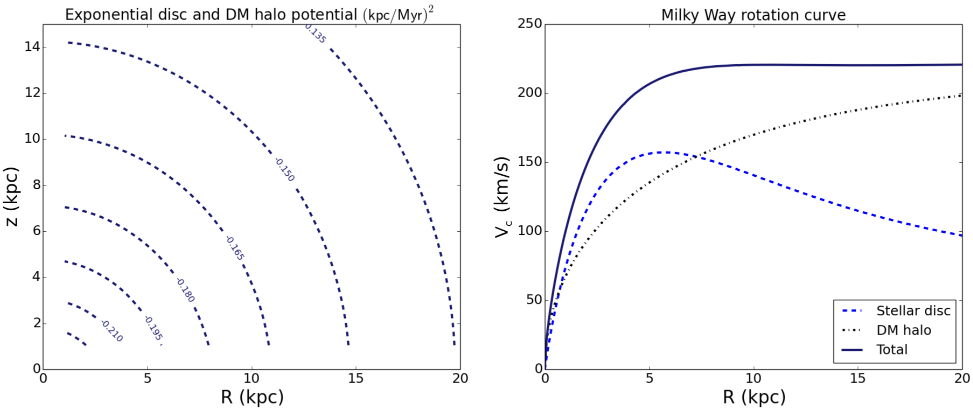

(a) Contours of the gravitational potential in units of (kpc/Myr)^2.

(b) Rotation curve.

Figure 2.7: Gravitational potential and rotation curve for the Milky Way model adopted in this thesis (see Table 2.2).

Figures 2.8a and 2.8b show the contours of the radial and vertical accelerations respectively.

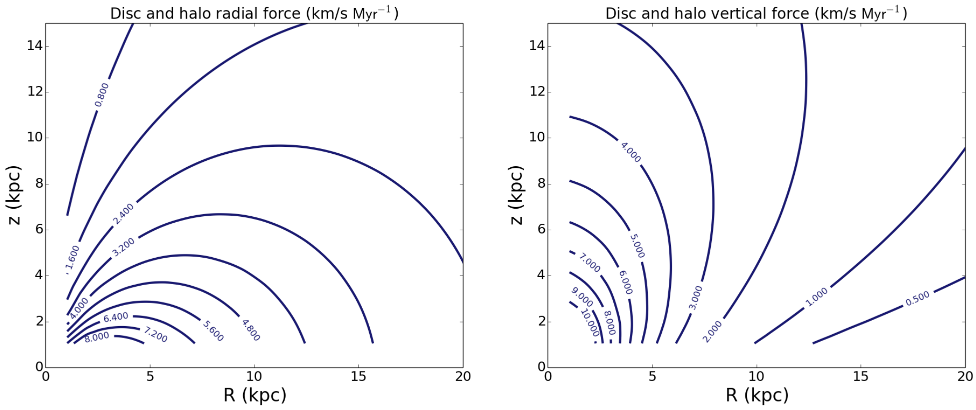

(a) Contours of the radial acceleration in units of km s^{-1} Myr^{-1}.

(b) Contours of the vertical acceleration in units of km s^{-1} Myr^{-1}.

Figure 2.8: Radial and vertical gravitational accelerations and rotation curve for the Milky Way model adopted in this thesis (see Table 2.2).

Figure 2.9 illustrates how the vertical acceleration changes according to the height above the midplane at different radii. Note that the profile at $R = 5$ kpc is a combination of between the disc g_z (Figure 2.3) and the halo one (Figure 2.6). On the other hand, the accelerations are very similar to the halo accelerations in the outer parts of the Galaxy, where the halo dominantes.

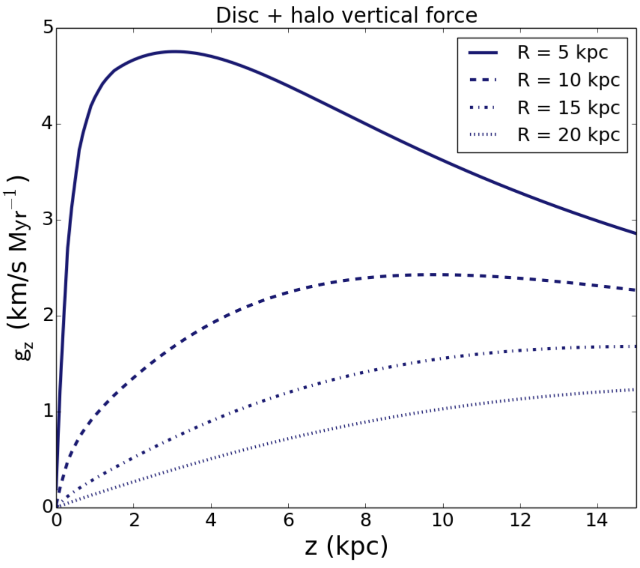

Figure 2.9: Vertical acceleration as a function of z at fixed radii for the Milky Way model adopted in this thesis (see Table 2.2).

Figures 2.10a, 2.10b,2.10c and 2.10d show the disc, the halo and the total vertical accelerations at R equal to 5 kpc, 10 kpc, 15 kpc and 20 kpc respectively. Note that the disc gravitational pull at $R = 5$ kpc exceeds the halo one up to $z \sim 4$ kpc, but this transition occurs at lower and lower z at larger radii.

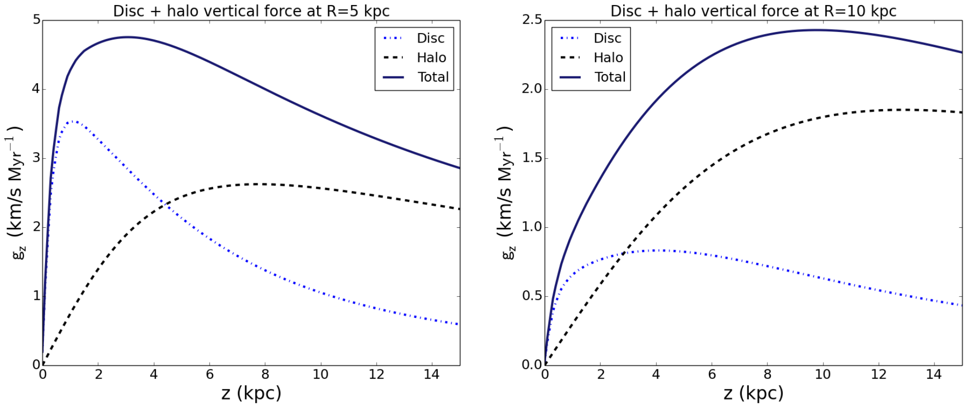

(a) Vertical acceleration at 5 kpc. **(b)** Vertical acceleration at 10 kpc.

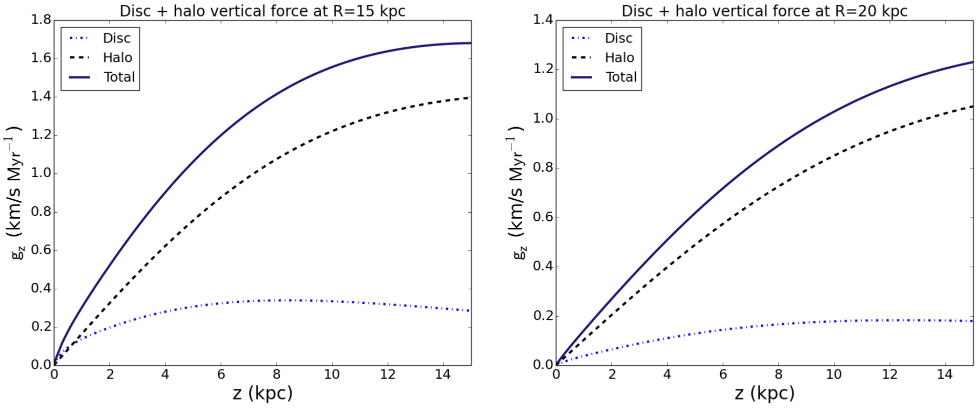

(c) Vertical acceleration at 15 kpc. **(d)** Vertical acceleration at 20 kpc.

Figure 2.10: Same as Figure 2.8: the graphics compare the disc (blue dotted lines), the halo (black dashed lines) and the total (dark blue solid line) vertical accelerations at fixed radii.

2.2 Numerical galactic fountain

In galaxies like the Milky Way, stellar activity and supernova explosions eject large amounts of cold gas ($T \approx 10^4$ K) out of the disc, triggering the so-called galactic fountain (Bregman 1980). An observational evidence of this mechanism is the presence of extra-planar neutral gas in several spiral galaxies (see Chapter 1). Early works (e.g. Collins et al. 2002, Fraternali & Binney 2006) proposed a ballistic model of the galactic fountain, the pure fountain scenario, that reproduces the observed distribution but not the kinematics of the extra-planar gas. Fraternali & Binney (2008) found that its kinematics could be reproduced by assuming that the neutral gas loses part of its angular momentum. Further studies, using analytical models, dynamical and hydrodynamical simulations (e.g. Marasco et al. 2012 and Melioli et al. 2008, 2009), explored the possibility that the decrease of angular momentum is due to the interaction of the cold gas with the hot galactic corona, which is made up of virial-temperature gas (T$\sim$ few 10^6 K) with low angular momentum. We can summarise the results as follows:

1. The Galaxy extra-planar gas emission is reproduced by numerical simulation of the galactic fountain and they suggest that the accretion rate of coronal gas is about $1.6\,\mathrm{M_{\odot}yr^{-1}}$ (Marasco et al. 2012). This is in excellent agreement with the amount of gas per year that is required to sustain the Galaxy's current star formation without depleting its reserve of interstellar gas.

2. There is a threshold velocity between the clouds and the corona, of about 75 km $\mathrm{s^{-1}}$, below which the hot gas ceases to absorb momentum from the cold clouds (Marinacci et al. 2011). The existance of this velocity threshold can explain the observed kinematics of the cold extra-planar gas.

3. The HI halo of the Milky Way is similar to that observed in other spirals and a galactic fountain origin is the most likely explanation for its origin. In this context, the Galactic HI halo would be made up of several thousand clouds with masses of $\sim 10^{4-5}\,\mathrm{M_{\odot}}$, of which the intermediate velocity clouds (IVCs) are the local counterpart.

Our numerical model of the galactic fountain is built using the code *Extragas* developed by Marasco et al. (2012). The authors performed a full dynamical modelling of the HI halo of the Milky Way using an improved version of the galactic fountain model of Fraternali & Binney (2006, 2008). In the code, gas clouds are modelled as particles that are initially considered to be in circular orbits in the $z = 0$ plane. In addition, they have isotropic random velocities with dispersion $\sigma_{ran} = 7.5$ km $\mathrm{s^{-1}}$. These particles are ejected from the disc into the halo with a kick velocity, whose direction is randomly chosen from a Gaussian distribution. Then, the code integrates the orbits of fountain particles until they fall back into the disc. The probability of ejection at velocity v with angle θ with respect to the vertical direction is (Fraternali & Binney 2006):

$$P(v, \theta) \propto \exp\left(-\frac{v^2}{2h_v^2 \cos^{2\Gamma}\theta}\right) \tag{2.12}$$

where h_v is the characteristic kick velocity. We choose $h_v = 80$ km $\mathrm{s^{-1}}$, which is, according to Fraternali & Binney (2006), the initial velocity of the fountain clouds required to reproduce the observed scale height of the extra-planar gas in NGC 891. Then, Γ is a constant that determines the extent to which clouds are ejected perpendicularly to the disc and it is fixed to a large value[3], which implies strong collimation of the ejecta along the normal axis to the plane. *Extragas* can also take into account the hydrodynamical interactions between the clouds and the corona. In the following sections, we describe the equations that the code solves and how the interactions with coronal gas are implemented. These results allow us to build a numerical model for the Milky Way galactic fountain which will be compared to an analytic approximation (Chapter 3).

---

[3] Fraternali & Binney (2006) found that a large values of Γ is required to reproduce the HI emission of NGC 891.

2.2.1 Pure fountain

If the interaction with the hot corona is not taken into account, the orbits of fountain clouds are affected only by gravity: this is called a *pure fountain* scenario. In this particular case, the equations that describe the motion of the fountain particles are:

$$\frac{d\vec{v}}{dt} = \vec{g} \tag{2.13a}$$

$$\frac{d\vec{x}}{dt} = \vec{v} \tag{2.13b}$$

where $\vec{g}$ is the gravitational acceleration:

$$\vec{g} = -\nabla\Phi \tag{2.14}$$

The potential Φ can be calculated through the software *Galforces* (see Section 2.1). Then, the accelerations are decomposed into three components in order to perform the integration in Cartesian coordinates:

$$g_x = \cos(\phi) g_R \tag{2.15a}$$

$$g_y = \sin(\phi) g_R \tag{2.15b}$$

$$g_z = g_z \tag{2.15c}$$

This model corresponds to the ballistic galactic fountain and it can be considered valid whenever the fountain clouds behave like bullets in the air (e.g. Collins et al. 2002). In more realistic conditions, we can include the interactions between fountain clouds and the hot corona. In the following sections, we describe which corrections to the gravitational acceleration allow us to take account of these effects.

2.2.2 Coronal drag

Fraternali & Binney (2008) suggested that fountain clouds feel a drag due to the ram pressure arising from their motion through the corona, so they experience a deceleration while the coronal gas gains angular momentum. The authors also introduced an analytical description of the drag interaction by assuming an high Reynolds number for the flow of the corona past a cloud. Thus, the drag effect is proportional to the square of the flow velocity v of the corona past the cloud and the acceleration can be written as:

$$g_{\text{drag}} = -\frac{Cv^2}{L} \tag{2.16}$$

where C is a dimensionless constant of order unity and v is the relative velocity between the cloud and the corona. L is the distance over which the clouds interacts with a portion of corona that contains a mass equal to its own mass and it is defined as:

$$L = \frac{m}{\rho\sigma} \tag{2.17}$$

where σ and m are the cloud cross-sectional area and mass and ρ is the coronal density. Following Fraternali & Binney (2008) and Marinacci et al. (2010), we can introduce a drag timescale as:

$$t_{\text{drag}} = \frac{m}{v_{\text{kick}}\sigma\rho} \tag{2.18}$$

Thus, the clouds velocity decreases due to the coronal drag as :

$$\vec{v} = \frac{\vec{v}_{\text{kick}}}{1 + Ctv_{\text{kick}}/L} = \frac{\vec{v}_{\text{kick}}}{1 + Ct/t_{\text{drag}}} \tag{2.19}$$

and the velocity halves in a time t_{drag}. Note that the drag effectiveness increases as the drag time shortens and it depends on the mass, the kick radius, the initial velocity v_{kick} of the clouds and on the coronal density.

2.2.3 Coronal condensation

In Milky Way-like galaxies the mixing of disc and coronal gas in the cloud's turbulent wake causes the condensation of material of the hot corona onto the clouds, so the mass of the cold (T $<$ few $\times$ 10^4 K) gas grows during the orbit. This condensation mechanism is described by Marinacci et al. (2010) and it occurs in the following stages:

1. the motion of the clouds through the hot corona onsets the Kelvin-Helmholtz instability;
2. each cloud developes a turbulent wake, whose material is stripped and mixed with the coronal one. This causes the blend of the hot gas of the corona with low angular momentum and the cold material of the clouds, whose momentum is higher.
3. Because of this mixing, the cooling time of the coronal gas dramatically decreases and becomes shorter than the orbital time. As a result, this material condenses into the wake, follows the clouds and it is accreted by the stellar disc. Therefore, the mass of the cold fountain gas grows and its angular momentum decreases.

From a dynamical point of view, the global effect of the condensation is a deceleration of the clouds velocity. Numerical simulations (Marinacci et al. 2010, 2011) show that the cold gas mass associated with any cloud grows as:

$$m(t) = m(0)e^{\alpha t} \tag{2.20}$$

where $m(0)$ is mass of the cloud at time $t = 0$ and α is the condensation rate. Thus, the mass accretion rate grows linearly with the mass and exponentially with the time:

$$\dot{m} = \alpha m(0)e^{\alpha t} = \alpha m \tag{2.21}$$

Following Marasco et al. (2012), coronal condensation slows down the clouds motion and this deceleration can be written as:

$$g_{\text{accr}} = -\alpha v \tag{2.22}$$

Finally, the total hydrodynamical deceleration that affects the orbits in *Extragas* is defined as:

$$g_{\mathrm{hydro}} = g_{\mathrm{accr}} + g_{\mathrm{drag}} \tag{2.23}$$

and the gravitational acceleration is corrected using the following three terms:

$$\begin{aligned} \vec{g}_x &= g_{\mathrm{hydro}} \frac{\vec{v}_x}{v_x} \\ \vec{g}_y &= g_{\mathrm{hydro}} \frac{\vec{v}_y}{v_y} \\ \vec{g}_z &= g_{\mathrm{hydro}} \frac{\vec{v}_z}{v_z} \end{aligned} \tag{2.24}$$

where v_x, v_y and v_z are the components of the relative velocity between the cloud and the corona. These interactions between the cold gas of the clouds and the hot gas of the galactic corona strongly influence the shape of the orbits. In the following section, we are going to study the orbits of single particles at fixed radii in order to understand the effect of these interactions.

2.3 Numerical orbits in the Milky Way potential

In this section we study the shape of the fountain orbits of clouds travelling through the potential of the Milky Way. We first focus on the pure fountain because, in this particular case, the trajectories of the particles are influenced only by the gravitational potential and the kick velocity. We will analise in detail the effects of choosing different forms of the potential or values of the drag timescale. Our aim is to understand these effects in order to build an analytical model which reproduces the numerical results. Then, we include the effects of the interaction with the galactic corona, the drag and the accretion. According to Marasco et al. (2012) and Marinacci et al. (2011), our fountain clouds and the hot corona are characterised as reported in Table 2.3.

Table 2.3: Fountain clouds and hot corona parameters: $v_{\rm lag}$ is the difference between the hot corona and the stellar disc rotation velocities.

Foutain clouds		Hot corona	
$T_{\rm cloud}$	10^4 K	$T_{\rm corona}$	2.7×10^6 K
Vertical kick velocity ($v_{\rm kick}$)	80 km $\rm s^{-1}$	Rotational velocity ($v_{\rm lag}$)	75 km $\rm s^{-1}$
$M_{\rm cloud}$	$2 \times 10^4\,\rm M_\odot$	$n_{\rm corona}$	$10^{-3}\,\rm cm^{-3}$
$R_{\rm cloud}$	100 pc		

Thus, the drag timescale is $t_{\rm drag} \simeq 530$ Myr. As already mentioned, the gravitational potential has a fundamental role in shaping the orbits, expecially in the pure fountain scenario. We build our model starting from a galactic potential for the Milky Way as described in Section 2.1, so three cases are going to be examined: double exponential disc, spherical NFW dark matter halo and a two-component model. Then, three orbits at different radii (5 kpc, 10 kpc and 15 kpc) will be selected in order to compare the effect of the potential and the influence of drag and accretion on their shapes.

2.3.1 Pure fountain

In this section, we examine the shape of the orbits in the absence of any interaction with the hot corona. This is not a fully realistic scenario for our Galaxy because the initial velocity of the clouds causes them to reach a significant height above the disc, so the interactions are unavoidable. On the other hand, the pure fountain scenario is an istructive example to understand how the orbits change according to the gravitational acceleration and which is the dominant acceleration that regulates the motion. In particular, the orbits in the meridional plane (R, z) are of great interest to our study because we aim to know how much time the clouds need in order to return to the disc. We can make some preliminary considerations about the expected characteristics of the orbits as follows. Consider a particle in the midplane, rotating on a circular orbit at the local circular velocity v_c and thus characterised by a given angular momentum. Let us now eject this particle out of the disc with an initial kick velocity v_{kick}: the total angular momentum is increased and we can see this kick as a perturbation of its trajectory. As a consequence, the particle moves outward in radius in order to conserve its angular momentum. We can foresee some qualitative characteristics of the pure fountain orbits:

1. Before the kick, the initial angular momentum of each particle is $L_{\text{tot}} = L_z = v_\phi R^2$, where L_{tot} is the total angular momentum and v_ϕ is equal to the circular velocity at radius R. The other two components of L_{tot} are null because $v_z = v_R = 0$. After the ejection, $v_z \neq 0$ and $v_R \neq 0$, so the total angular momentum has been increased. If the v_{kick} is much lower than the circular velocity, we can expect that the initial L_{tot} is much greater than the acquired angular momentum. For example, $v_\phi = 220$ km s^{-1} at the Solar radius while $v_{\text{kick}} = 80$ km s^{-1} . As a consequence, if the rotation curve is flat, the radial displacement should be a small fraction of the initial radius.

2. As reported in Fraternali & Binney (2006), we can expect that the order of magnitude of the orbital time is 10^8 yr and the radial displacement is small. As a consequence, we can infer that also the radial velocity is low.

3. In Section 2.1, we have shown that the vertical acceleration decreases with radius (Figure 2.3, 2.6 and 2.9), so we can foresee that the maximum height reached by the particles (at constant v_{kick}) will rise in the outer parts of the disc.

4. Let us consider the particle at two different times and radii: at $t = 0$, when the particle is in the midplane at the kick radius R_{kick}, and at $t = t_{\text{orb}}$, when the particle crosses the midplane at the landing radius R_{land}. If we consider the total energy in these two moments and we take into account that the radial displacement is small, we find that both the gravitational potential at $z = 0$ and the circular velocity have remained approximately the same. In fact, no energy is dissipated during the orbits, so we can expect that the final vertical velocity should be equal to the kick velocity.

The pure galactic fountain is well-described by these statements (see Figures 2.15 and 2.16) but the inclusion of coronal interaction will break the approximations and change the orbital characteristics. However, it is interesting to study how the shape of the orbits change according to the potential and the matter distribution, so we are going to analyse the clouds motion in the presence of the disc and the halo separetely, and then with the whole potential.

Orbits in the disc potential

In this section we describe in detail the orbits in the presence of the exponential disc potential. Figure 2.11 shows a three-dimensional representation of these orbits, note the huge difference between the distance travelled in the R and z direction as the kick radius increases. Figure 2.12a, 2.12c and 2.12e show their shape at 5 kpc, 10 kpc and 15 kpc respectively. Note that the maximum z reached by the particles considerably increases with radius because of the dramatic weakening of the gravitational pull (Figure 2.3). In addition, the displacement along R becomes more and more significant in the outer parts of the disc, exceeding 40 kpc at $R = 15$ kpc. Indeed, the circular velocity falls at large radii, so the particles must move to the outermost radii in order to conserve their angular momentum after the kick. Figures 2.12b, 2.12d and 2.12f show how the velocity components along R, ϕ and z vary during the motion. In the light of what we said before, it can be noticed that the vertical velocity v_z ranges from 80 km s^{-1} to -80 km s^{-1} for the orbits at 5 kpc, in perfect agreement with our expectations. On the other hand, the particles kicked at 10 kpc and 15 kpc fall back into the disc with about -40 km s^{-1} and -20 km s^{-1} respectively, as the radial displacement is highly significant and the rotation curve is not flat. Then, the tangential velocity (v_ϕ) gradient becomes more significant as the orbits move outward and the radial velocity peak grows with the ejection radius. Another important feature is that the initial v_R is null, while the final is positive.

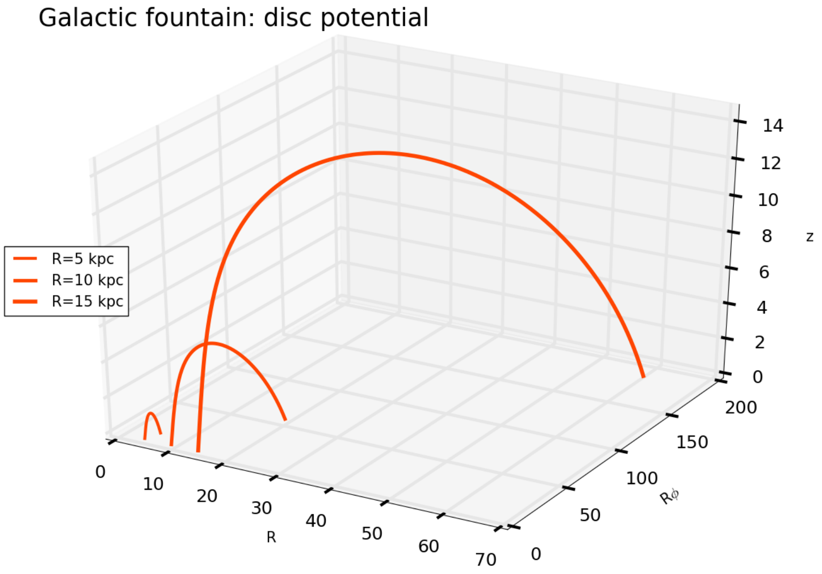

Figure 2.11: Pure fountain orbits for particles leaving the disc at $R_{\rm kick}$ =5 kpc, 10 kpc and 15 kpc, the kick velocities are $v_{\rm kick} = 80$ km s^{-1}. The particles travel in the potential of the stellar disc alone (see Section 2.1.1 for details).

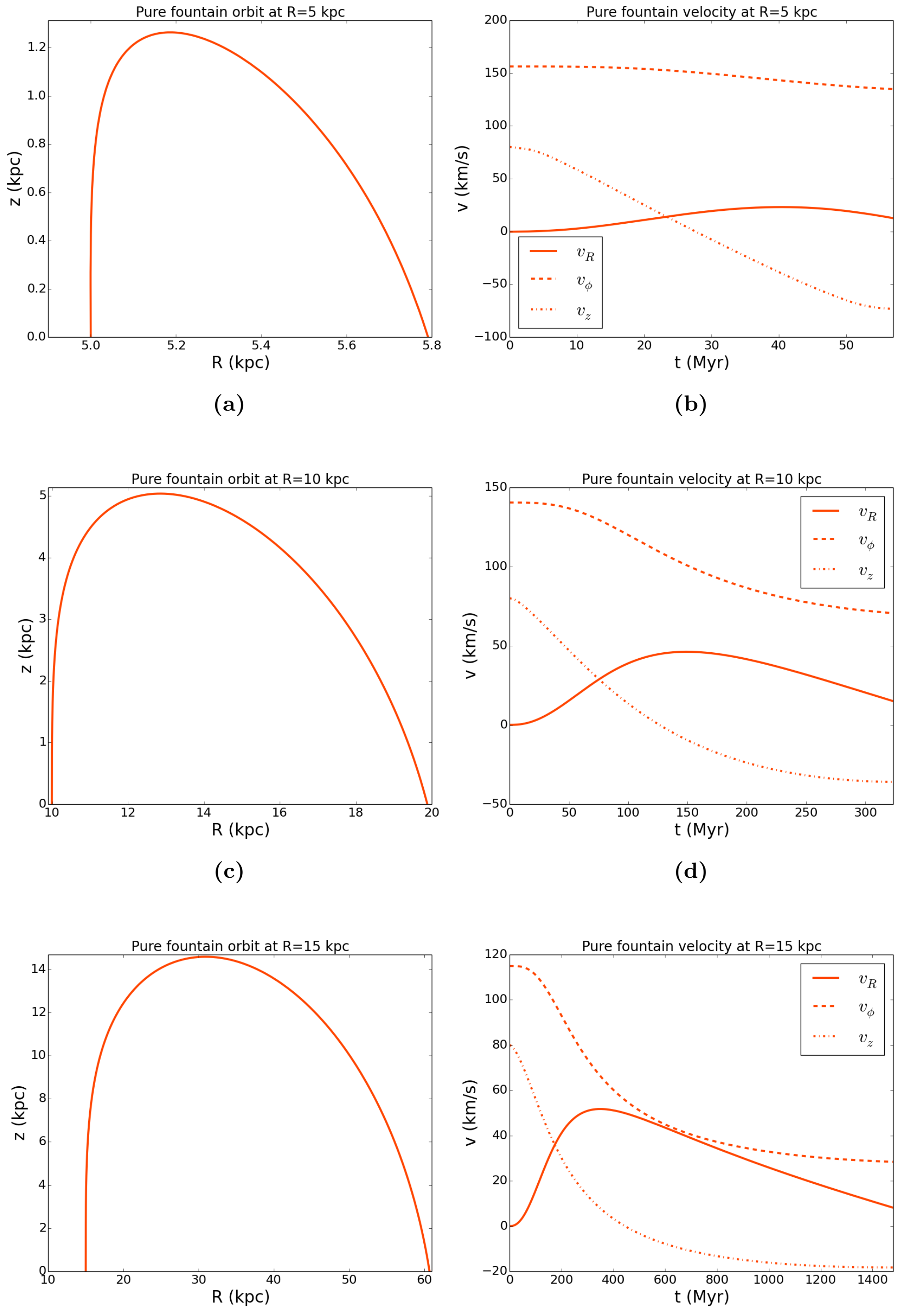

(a) **(b)**

(c) **(d)**

(e) **(f)**

Figure 2.12: *Left*: pure fountain orbits in the meridional plane (R, z), the kick velocity is $v_{\rm kick} = 80$ km s^{-1} and the kick radii are (from the top to the bottom) $R_{\rm kick}$ =5 kpc, 10 kpc and 15 kpc. *Right*: radial (v_R), circular (v_ϕ) and vertical (v_z) velocities as a function of time for the pure fountain scenario. The particles travel in the potential of the stellar disc alone (Section 2.1.1).

Orbits in the halo potential

The dark matter halo potential significantly differs from that of the disc, so we expect very different shapes of the orbits. Figure 2.13 shows a three-dimensional representation of the orbits in the presence of the halo potential, note that their shape does not change significantly as the kick radius increases. Figures 2.14a, 2.14c and 2.14e show the shape of the orbits at 5 kpc, 10 kpc and 15 kpc respectively. In this case, the vertical acceleration (Figure 2.6) is weaker in the outer parts of the galaxy than in the inner ones but the gradient is not so strong as for the disc potential. Figures 2.14b, 2.14d and 2.14f show how the velocity components along R, ϕ and z vary during the motion. The maximum z reached by the particles rises with radius but the growth is much lower than the case of the disc potential (see Figure 2.1a). In addition, the displacement along R increases in the outer parts of the disc, reaching $\sim$ 1 kpc at $R = 15$ kpc, so it is essentially negligible. Indeed, the radial variation of the circular velocity is small as the rotation curve mildly increases with radius, so particles must travel a small distance along R in order to conserve their angular momentum. Thus, the tangential velocity gradient is limited. Note that, the vertical velocity v_z ranges from 80 km s^{-1} to -80 km s^{-1} during the orbit, in excellent agreement with our expectations.

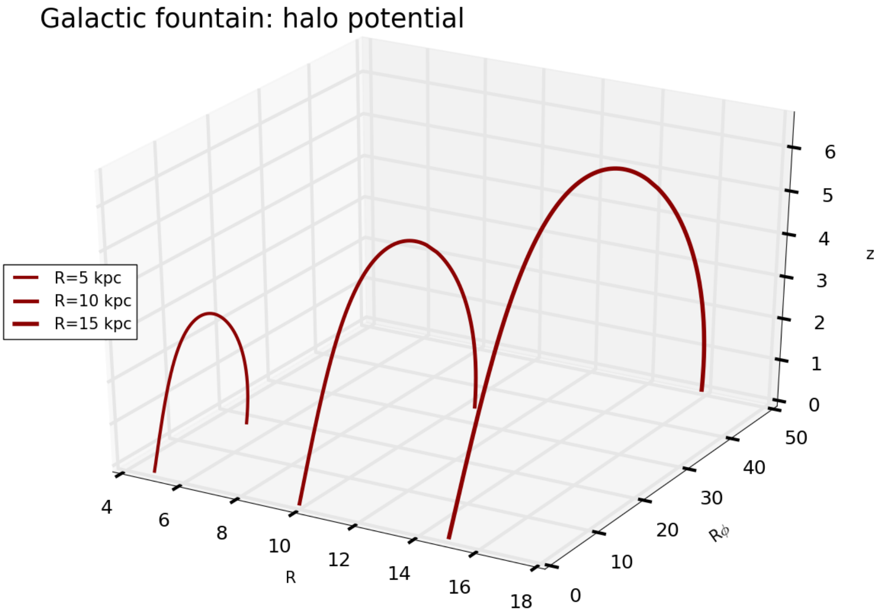

Figure 2.13: Same as 2.11 except that the particles travel in the potential of the dark matter halo alone (see Section 2.1.2 for details).

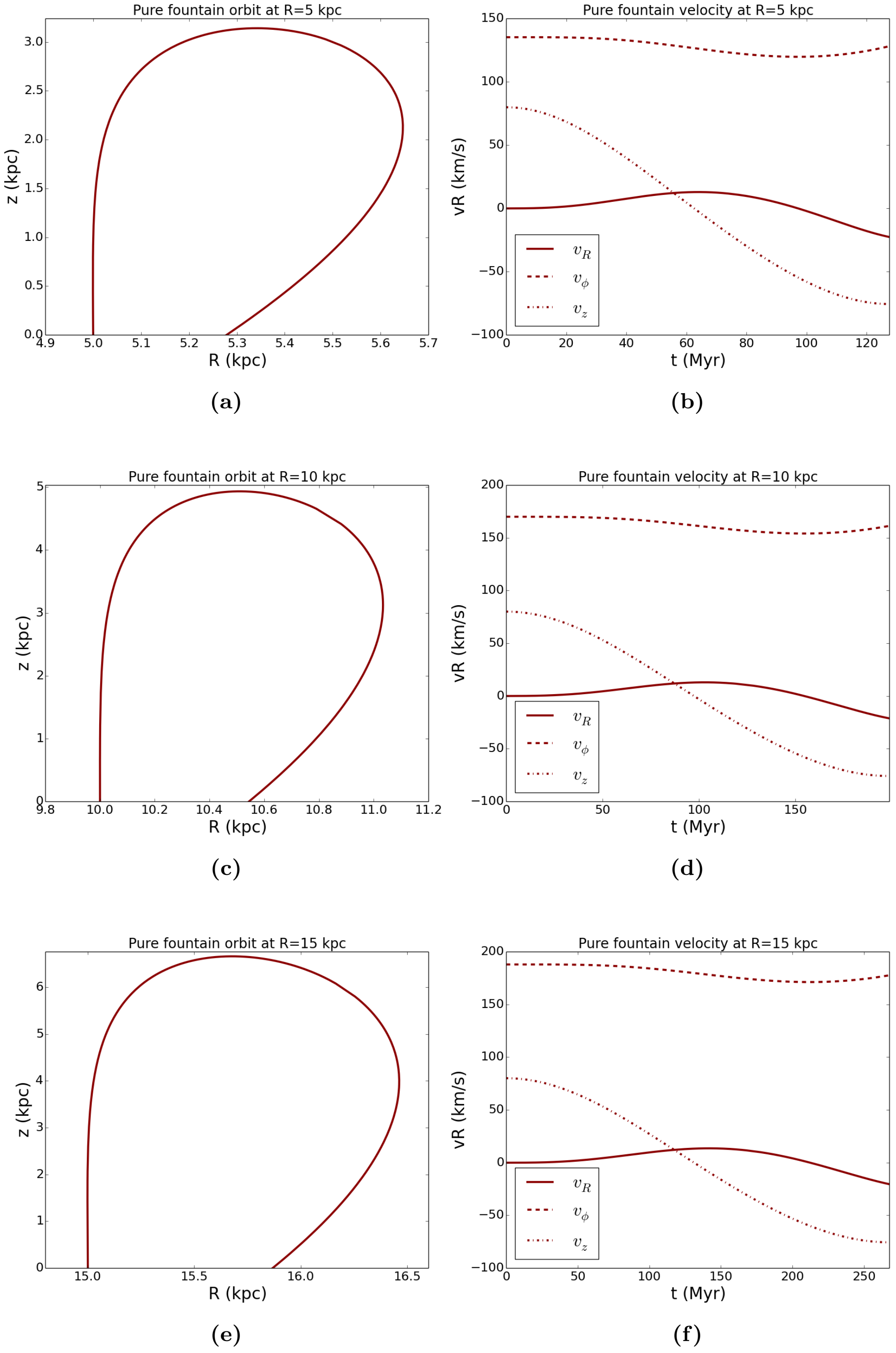

(a) **(b)**

(c) **(d)**

(e) **(f)**

Figure 2.14: Same as 2.12 except that the particles travel in the potential of the dark matter halo alone (see Section 2.1.2 for details).

Orbits in the Galactic potential

The following results concern the pure galactic fountain in the two-component model of our Galaxy (see Table 2.2). Figure 2.15 shows a three-dimensional representation of the orbits at 5 kpc, 10 kpc and 15 kpc, while Figures 2.16a, 2.16c and 2.16e provide their shapes in the meridional plane. We pointed out in Section 2.1.3 that the disc contribution to the vertical acceleration (Figure 2.10) is dominant in inner parts of the Galaxy, while the halo one prevails at outer radii. As a consequence, the vertical acceleration (Figure 2.6) is weaker in the outer parts of the galaxy than in the inner regions but the gradient is not so strong as for the disc alone. In addition, there is a transition height ($z_{\rm t}$) where the the halo starts outweighing the disc and it depends on R. As an example, the transition for the orbits at 5 kpc, 10 kpc and 15 kpc occurs at z about 4 kpc, 3 kpc and less than 1 kpc. If we compare the $z_{\rm t}$ and the maximum z ($z_{\rm max}$) reached by the particles a certain radius, we can infer which one of the two components is dominating the orbits. The orbit at 5 kpc is identical to that in the disc case (Figure 2.12a), in fact $z_{\rm t}$ is higher than $z_{\rm max}$. At 10 kpc, $z_{\rm t}$ and $z_{\rm max}$ are essentially equal, indeed the orbits shape is between the disc case and the halo one. Finally, the orbits at 15 kpc resembles that in Figure 2.14a because the particle reaches heights above $z_{\rm t}$, so the halo vertical acceleration is dominant. These fundamental differences can also be seen in Figure 2.15. Figures 2.16b, 2.16d and 2.16f show how the velocity components along R, ϕ and z vary during the motion. Like the previous case, the vertical velocity v_z ranges from 80 km s^{-1} to -80 km s^{-1} . Note that neither the radial velocity nor the tangential one experience a strong variation during the orbits, in fact the rotation curve is flat at 220 km s^{-1} and the radial displacement is small. In Appendix A, we provide the orbits in the meridional plane calculated for times up to 1 Gyr (Figure A.1), so the particles cross the midplane many times and we can see how the shape of the orbits changes over a longer period of time.

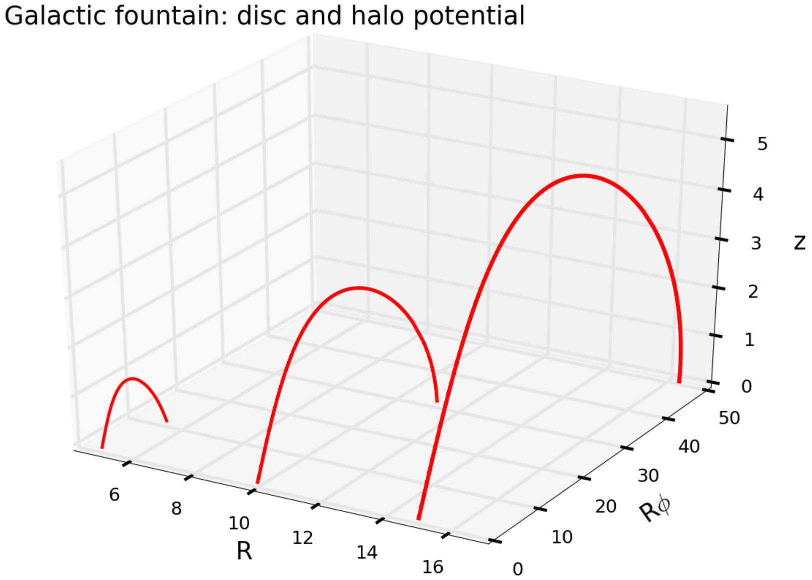

Figure 2.15: Same as 2.11 except that the particles travel in the two-component potential (Table 2.2).

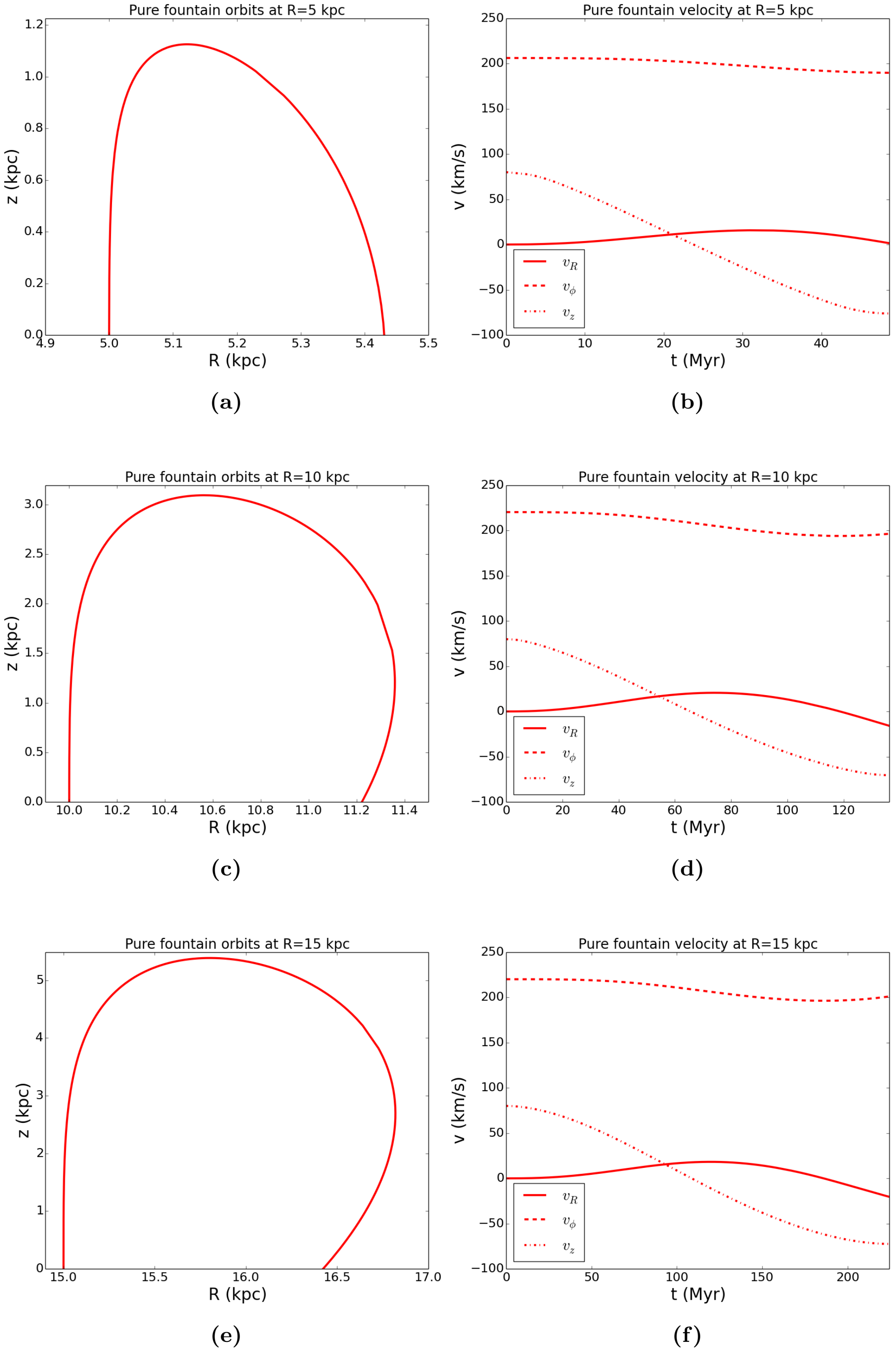

(a) **(b)**

(c) **(d)**

(e) **(f)**

Figure 2.16: Same as 2.12 except that the particles travel in the two-component potential (see Table 2.2).

2.3.2 Coronal drag

In this section we analise the drag effect on the pure fountain in the presence of both the stellar disc and the dark halo. The clouds experience the effect of a ram pressure and lose angular momentum as they move through the hot corona. As a result, they transfer momentum to the corona, which is supposed to have a lower angular momentum than the stellar disc (e.g Hodges-Kluck et al. 2016). We expect the shape of the orbits to change because the drag breaks the conservation of the angular momentum. In fact, the L_{tot} increment given at the moment of ejection is significantly reduced by the drag and the longer is the orbital time, the stronger is this decline. So, we can foresee that the outward motion along R-direction should be even less important than the pure fountain situation. In addition, the z-component of the deceleration $\vec{g}_{\text{drag}}$ also effects the vertical velocity. As a result, z_{max} reached by the clouds should be lower than in the previous case because part of the kinetic energy is dissipated. Figure 2.17 provides a three-dimensional comparison between the pure fountain orbits and those with drag, while Figures 2.18a, 2.18c and 2.18e represent their shapes at 5 kpc, 10 kpc and 15 kpc in the meridional plane. Note that the shapes of the orbits are in agreement with our expectations because the radial displacement and z_{max} are smaller than the ones in the pure fountain scenario. The particular trajectory in Figure 2.18e shows that, if a particle loses too much angular momentum, it moves inward along R and falls back onto the disc at a radius significantly smaller than that of ejection. However, an interesting feature of these orbits is that the vertical velocity trend (Figure 2.18b, 2.18d and 2.18f) is the same as the pure fountain. Concering the other velocity components, there are slight but important differences in v_R and v_ϕ that modify the radial and tangential motion. In Appendix A, Figure A.2 shows the orbits calculated up to 1 Gyr.

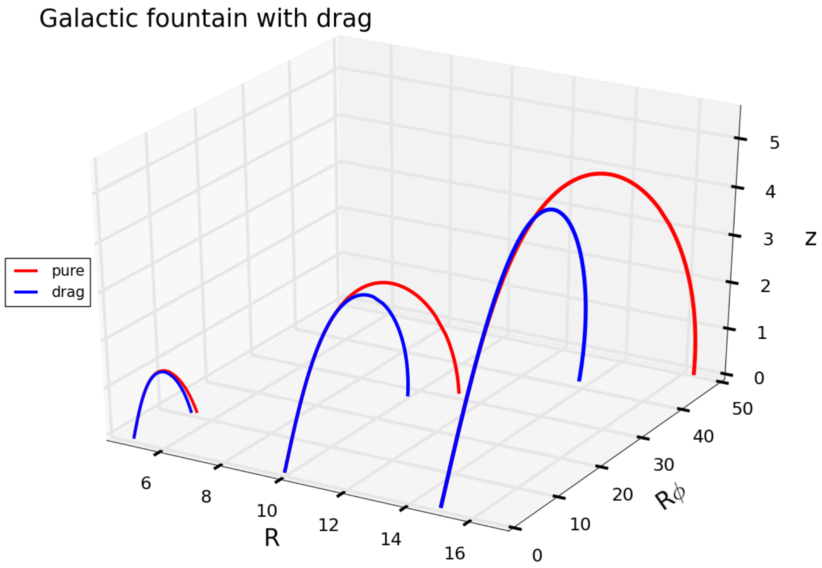

Figure 2.17: Fountain orbits with the drag effect (blue) (see Table 2.3) and in the pure fountain scenario (red). The particles are ejected from the disc at R_{kick} =5 kpc, 10 kpc and 15 kpc with kick velocity $v_{\text{kick}} = 80$ km s^{-1} and they travel in the two-component potential (see Table 2.2).

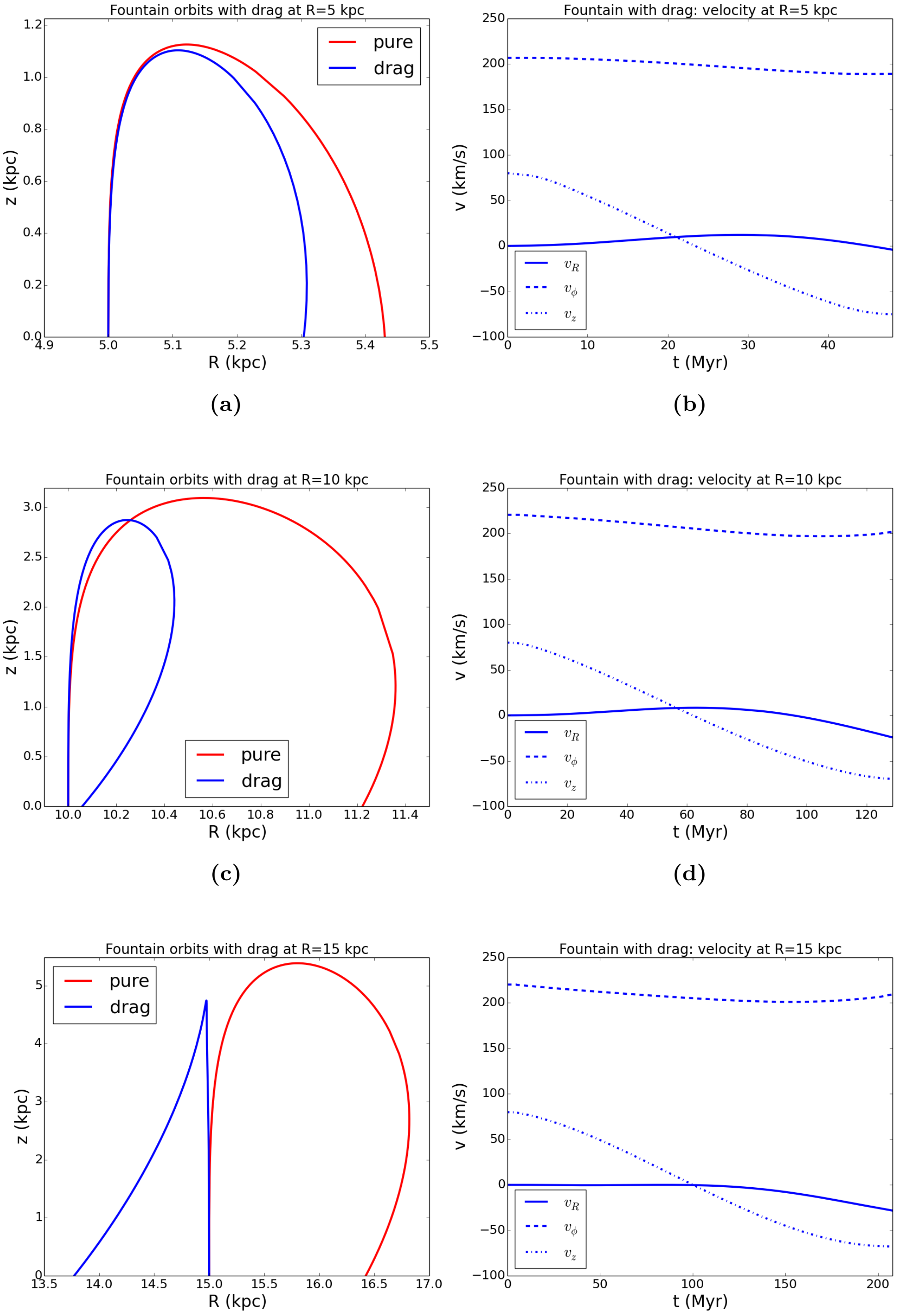

(a) (b)

(c) (d)

(e) (f)

Figure 2.18: *Left*: comparison of the orbits in the meridional plane (R, z) with the drag effect (blue) and those in the pure fountain case (red) in the two-component potential (Table 2.2). The kick velocities are $v_{\rm kick} = 80$ km s^{-1} and the kick radii are (from the top to the bottom) $R_{\rm kick}$ =5 kpc, 10 kpc and 15 kpc. The clouds and the hot corona are defined as reported in Table 2.3. *Right*: radial (v_R), circular (v_ϕ) and vertical (v_z) velocities as a function of time for the fountain with the drag.

As already mentioned, the drag is more effective the shorter its timescale. Therefore, it is interesting to analise how its efficiency changes as a function of $t_{\rm drag}$. We can infer from eq. 2.18 that the timescale is directly proportional to the mass of the cloud. So, we can study three cases with different $M_{\rm cloud}$:

- $M_{\rm cloud} = 10^4\,{\rm M}_\odot \Rightarrow t_{\rm drag} = 270$ Myr;
- $M_{\rm cloud} = 2 \times 10^4\,{\rm M}_\odot \Rightarrow t_{\rm drag} = 530$ Myr;
- $M_{\rm cloud} = 3 \times 10^4\,{\rm M}_\odot \Rightarrow t_{\rm drag} = 800$ Myr.

In Figure 2.19, we compare our model with $t_{\rm drag} = 530$ Myr and the others. Figures 2.20a, 2.20b and 2.20c represent the orbits at 5 kpc, 10 kpc and 15 kpc respectively. The radial displacement grows according to $t_{\rm drag}$ and it increases as the timescale shortens. There is a slight difference also in $z_{\rm max}$ reached by the particles because the drag deceleration also effects the vertical velocity.

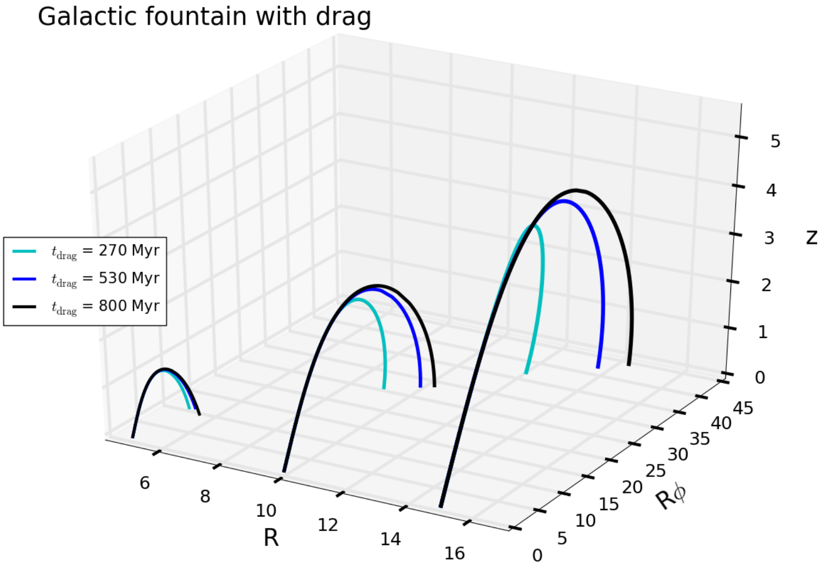

Figure 2.19: Fountain orbits with the effect of drag with timescales (see text): $t_{\rm drag} = 270$ Myr (light blue), $t_{\rm drag} = 530$ Myr (blue) and $t_{\rm drag} = 800$ Myr (black). The particles are kicked out of the disc at $R_{\rm kick}$ =5 kpc, 10 kpc and 15 kpc (from left to right) with $v_{\rm kick} = 80$ km s^{-1} and they travel in the two-component potential (see Table 2.2).

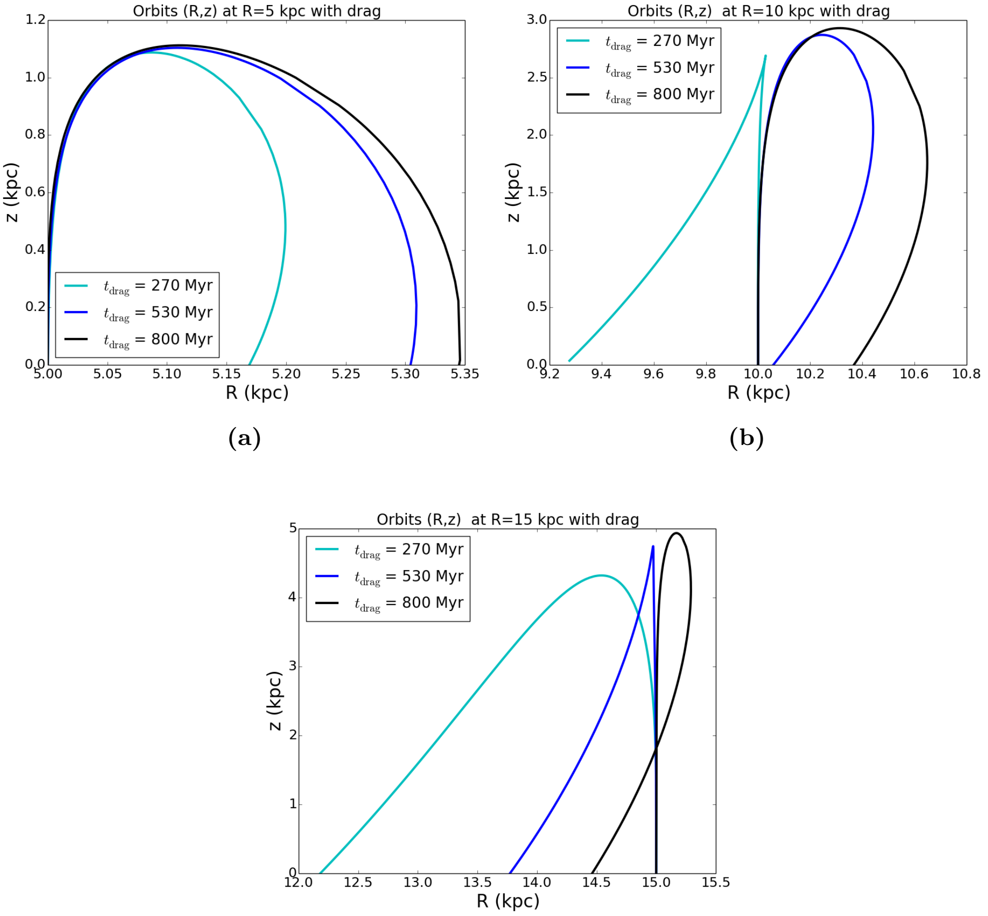

(a) **(b)**

(c)

Figure 2.20: Orbits in the meridional plane (R, z), same as 2.19.

2.3.3 Coronal condensation

The pure galactic fountain described in Section 2.2.2 is modified in order to include the condensation of material from the hot corona (Fraternali & Binney 2008, Marasco et al. 2012). The clouds experience a deceleration due to the accretion, so we can expect that its role in shaping the fountain orbits is similar to the drag force. Indeed, the angular momentum of the clouds is not conserved and the radial displacement should be smaller than the pure fountain case. In addition, the z-component of the deceleration $\vec{g}_{\rm accr}$ affects the vertical velocity. As a result, the maximum height reached by the orbits should be lower than in the pure case because kinetic energy is dissipated. Figure 2.21 provides a three-dimensional comparison between the pure fountain orbits and those with accretion. Figures 2.22a, 2.22c and 2.22e represent the orbits at 5 kpc, 10 kpc and 15 kpc respectively and their shape agree with our predictions. The orbits at 10 kpc and 15 kpc show a significant inward motion due to the considerable drop of the angular momentum, so the particles fall back onto the disc at a radius smaller than that of ejection. In this case, only the vertical velocity trend in Figure 2.22b is the same as the pure fountain. Indeed, Figures 2.22f and 2.22d show that v_z at the end of the orbits is about -60 km s^{-1} . Concerning the other velocity components, the trends are similar but more sizeable in values. The effectiveness of accretion in shaping the orbits is proportional to the condensation rate α, which depends on the volume density of the infalling material (Fraternali & Binney 2008). We have chosen $\alpha = 6.3\,\text{Gyr}^{-1}$ according to the numerical simulations perfomed by Marasco et al. (2012), who found that this is the best-fit value needed to reproduce the extra-planar HI emission of the Milky Way. However, the spatial variation of α along R and z is not known. In Appendix A, we provide the orbits in the meridional plane calculated up to 1 Gyr (Figure A.3).

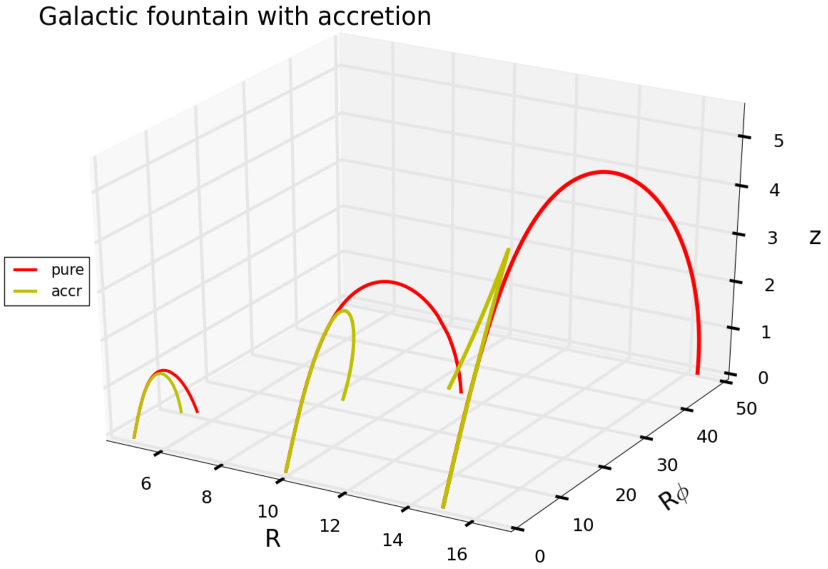

Figure 2.21: Fountain orbits with the condensation effect (yellow) (see Table 2.3) and in the pure fountain scenario (red). The particles are ejected from the disc at $R_{\rm kick}$ =5 kpc, 10 kpc and 15 kpc with kick velocity $v_{\rm kick}$ = 80 km s^{-1} and they travel in the two-component potential (see Table 2.2).

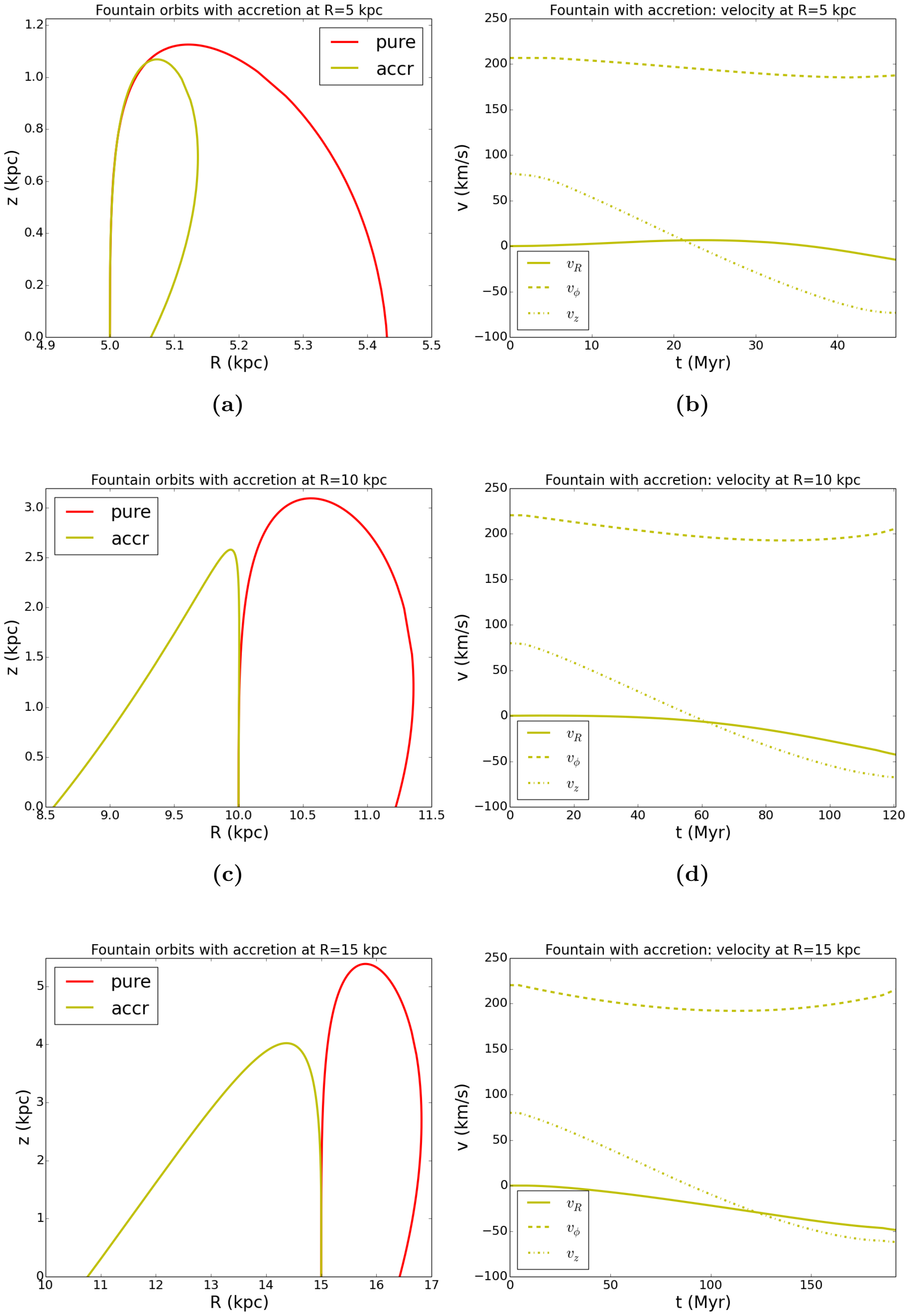

(a) (b)

(c) (d)

(e) (f)

Figure 2.22: Same as Figure 2.18 but with the effect of the coronal condensation (yellow) instead of the drag.

2.3.4 Realistic galactic fountain

In this section, we report the results of a numerical model for the galactic fountain which includes both drag and accretion. Clearly, the role of the coronal interactions in shaping the orbits is the same as described in Sections 2.3.2 and 2.3.3 but their effect is more significant. Figure 2.23 provides a three-dimensional comparison between the four cases while Figures 2.24a, 2.24c and 2.24e represent the orbits in the meridional plane at 5 kpc, 10 kpc and 15 kpc respectively. All orbits show a significant inward motion due to the loss of angular momentum, so the particles fall back onto the disc at a radius smaller than the ejection one. In addition, the $z_{\rm max}$ is reduced by a significant amount. However, it is clear that accretion is the dominant interaction because the shapes of the orbits resemble more the ones with accretion than those with drag. Once again, the vertical velocity trend in Figure 2.24b is the same as the pure fountain and v_z ranges from 80 km s^{-1} to about -80 km s^{-1}. On the other hand, this is not true in the outer parts of the disc, in fact the final downward velocity is about -60 km s^{-1} for the orbit at 10 kpc (Figure 2.24d) and -50 km s^{-1} at 15 kpc (Figure 2.24f). Once again, in Appendix A we provide the orbits in the meridional plane calculated up to 1 Gyr (Figure A.4).

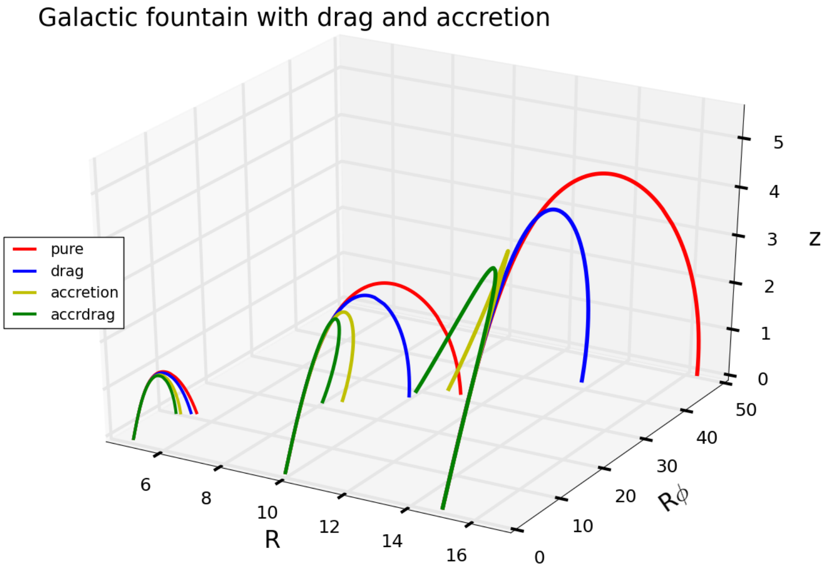

Figure 2.23: Fountain orbits in the pure fountain scenario (red) and with drag only (blue), condensation only (yellow) and both the effects (green) (see Table 2.3). The particles are ejected from the disc at $R_{\rm kick}$ =5 kpc, 10 kpc and 15 kpc with kick velocity $v_{\rm kick}$ = 80 km s^{-1} and they travel in the two-component potential (see Table 2.2).

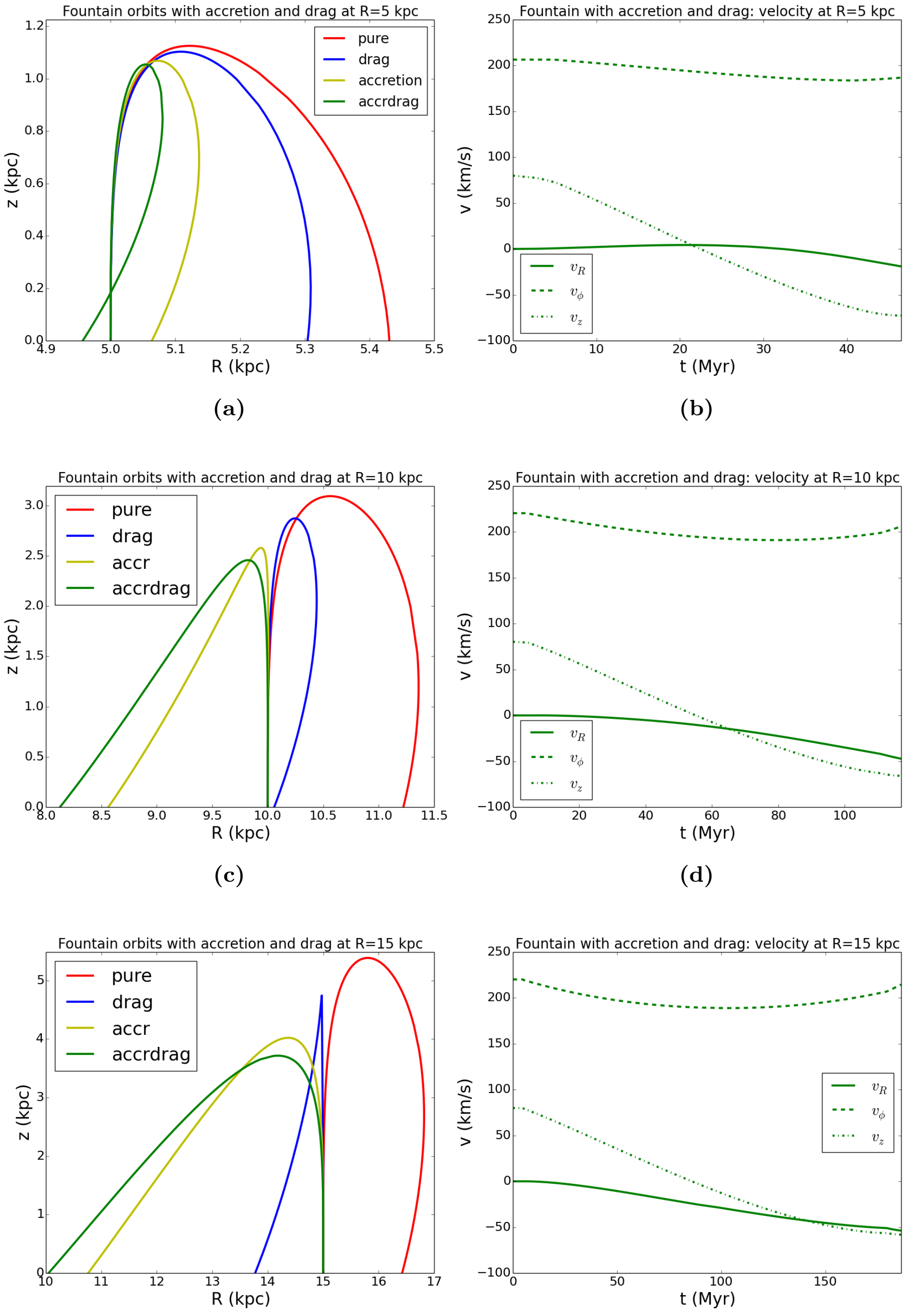

(a) (b)

(c) (d)

(e) (f)

Figure 2.24: *Left*: comparison between the fountain orbits in the meridional plane (R, z) with the effects of coronal interactions (pure fountain (red), drag (blue), accretion (yellow) and both accretion and drag (green)) in the two-component potential (Table 2.2). The clouds and the hot corona are defined as reported in Table 2.3. The kick velocity is $v_{\rm kick} = 80$ km s^{-1} and the kick radii are (from the top to the bottom one) $R_{\rm kick}$ =5 kpc, 10 kpc and 15 kpc. *Right*: radial (v_R), circular (v_ϕ) and vertical (v_z) velocities as a function of time.

Chapter 3

An analytic model for the galactic fountain

In this chapter we introduce an analytical model of the galactic fountain in the presence of the potential of our Galaxy. In Section 3.1, we build a simple model of the Milky Way gravitational potential and we compare it to the numerical results provided in Section 2.1. In Section 3.2, we describe a theoretical model of pure fountain and then we illustrate a simple analytical way to include the drag and the condensation of the hot corona.

3.1 Analytical accelerations

In this section we aim to find a simple analytic model for the Milky Way potential to be used for the integration of the fountain orbits. We are particularly interested in an analytical form for the vertical gravitational accelerations in order to compare them to the numerical accelerations analised in Section 2.1. We apply the method to the Milky Way-like model described in Section 2.1, but this method is absolutely general and it could be used for any galaxy. First, we model the potential of the disc (see Section 2.1.1) and the halo (see Section 2.1.2) separately, then we create a two-component model including both distributions (see Section 2.1.3). All these models share the same assumptions as those of the numerical calculation of the potentials performed by *Galforces* (see Section 2.1): the system is axisymmetric and its plane of symmetry is the equatorial plane. Observations suggest that the Milky Way forms new star only out to 12-13 kpc from the center. In addition, the innermost parts of the Galaxy are characterised by the presence of the bulge, whose stars are old, and by the bar, which is non-axisymmetric. Therefore, we can restrict our analysis to the central parts of the disc between 4 kpc and 12-13 kpc, where where the star formation activity generate galactic fountains (e.g. Case & Bhattacharya 1998) and the potential can be safely considered axisymmetric.

3.1.1 The stellar disc

It is known that there are accurate methods to find the potential of a disc with a non-zero thickness. For example, for a double-exponential disc we could use eq. 2.170 in Binney & Tremaine (2008), which involves Bessel's functions. Unfortunately, this method does not provide a simple form for the vertical acceleration, so the equations for the fountain orbits (see Section 3.2 for details) could not be solved analytically. As a consequence, we must find reasonable approximations that can help us finding a straightforward functional form for the vertical acceleration of the Milky Way's disc.

In Section 2.1.1, we pointed out that the numerical vertical acceleration (see Figure 2.3) rises steeply in the inner parts of the disc and its trend has a clear peak. Then, in the outer parts, the accelerations tend to become approximately constant with z above a certain height that depends on the radius. As a consequence, in order to build our analytic model, we consider two approaches that correspond to the following approximations:

1. a linear vertical acceleration is suitable for the inner parts of the disc, where we expect the fountain to reach low heights as the downward gravitational pull is strong;

2. a constant vertical acceleration for the outer parts of the disc, where the fountain can achieve larger heights.

The maximum height reached by fountain particles depends on the kick velocity, so we will analise the effect of changing the values of the initial vertical velocity. In the next sections, we describe in detail these two approaches and we compare the results to the numerical vertical accelerations (see Section 2.1.1).

Linear vertical acceleration

Let us consider the disc density distribution $\rho_\star$, this is linked to the gravitational accelerations by the Poisson equation:

$$\nabla^2\Phi(R,z) = 4\pi G\rho_\star(R,z) \tag{3.1}$$

which can be written in cylindrical coordinates as:

$$\frac{1}{R}\frac{\partial}{\partial R}\left(R\frac{\partial\Phi(R,z)}{\partial R}\right) + \frac{1}{R^2}\frac{\partial^2\Phi(R,z)}{\partial\phi^2} + \frac{\partial^2\Phi(R,z)}{\partial z^2} = 4\pi G\rho_\star(R,z) \tag{3.2}$$

The first term of the l.h.s. is related to the radial acceleration through the following approximated relation:

$$\frac{\partial\Phi(R,z)}{\partial R} \approx \frac{\partial\Phi(R,0)}{\partial R} = \frac{v_c^2(R)}{R} \tag{3.3}$$

Because of the assumption of axisymmetry, the second term of the l.h.s. is null. Let us consider the third term of the l.h.s. in eq. 3.2. For those orbits that remain near the midplane, the potential Φ can be expanded in the z direction as a Taylor series:

$$\Phi(R,z) \approx (\Phi(R,z))_{z=0} + z\left(\frac{\partial\Phi(R,z)}{\partial z}\right)_{z=0} + \frac{z^2}{2}\left(\frac{\partial^2\Phi(R,z)}{\partial z^2}\right)_{z=0} + O(z^3) \tag{3.4}$$

Using this series up to the third order and remembering that $\frac{\partial\Phi}{\partial z}(R,0) = 0$, we obtain:

$$\frac{\partial\Phi(R,z)}{\partial z} \approx z\left(\frac{\partial^2\Phi(R,z)}{\partial z^2}\right)_{z=0} \tag{3.5}$$

At this point, following Olling (1995), we can introduce the so-called **rotational density** that takes account of the radial gravitational acceleration in the plane $z = 0$. The rotational density can be defined as:

$$\rho_{\rm rot}(R) = -\frac{1}{4\pi G}\frac{1}{R}\frac{\partial}{\partial R}\left(R\frac{\partial\Phi(R,0)}{\partial R}\right) = -\frac{1}{2\pi G}\frac{v_c(R)}{R}\frac{\partial v_c(R)}{\partial R} \tag{3.6}$$

Using eq. 3.6 in eq. 3.2, the Poisson equation becomes:

$$\frac{\partial^2\Phi(R,0)}{\partial z^2} = 4\pi G\left(\rho_\star(R,0) + \rho_{\rm rot}(R)\right) = 4\pi G\rho_{\rm eff}(R) \tag{3.7}$$

where $\rho_{\rm eff}$ is the effective density. The rotational density is non-negligible only if the rotation curve is not flat and its sign varies as a function of to the radial gradient of the rotation curve:

(i) $\frac{\partial v_c}{\partial R} > 0$: rising rotation curve, so $\rho_{\rm rot} < 0$ and $\rho_{\rm eff} < \rho_\star$. As a consequence, the rotational density reduces the disc density and the accelerations are weakened.

(ii) $\frac{\partial v_c}{\partial R} < 0$: falling rotation curve, so $\rho_{\rm rot} > 0$ and $\rho_{\rm eff} > \rho_\star$. As a result, the rotational density increases the effect of the disc density and the accelerations are intensified.

(iii) $\frac{\partial v_c}{\partial R} = 0$: flat rotation curve, so $\rho_{\rm rot} = 0$ and $\rho_{\rm eff} = \rho_\star$. In this case, the rotational density has no effect on the vertical acceleration.

Following Iorio (2014), we can define:

$$\eta_\star \equiv \frac{\rho_{\rm rot}}{\rho_\star} \tag{3.8}$$

thus $\eta_\star$ has the same sign as the rotational density. Note that the above analysis (from eq. 3.1 to eq. 3.8) is absolutely generic and it can be applied to any mass distribution by substituting the disc density with a generic mass distribution. In fact, the only condition that must be fulfilled is that the orbits should remain near the midplane. Our approach leads to an analytic form for the vertical acceleration that is written as follows:

$$g_z(R,z) = -\frac{\partial\Phi(R,0)}{\partial z} = -4\pi G\left(\rho_\star(R,0) + \rho_{\rm rot}(R)\right)z \tag{3.9}$$

At this point, we can apply these results to the disc density distribution. As mentioned in Section 2.1.1, the matter distribution of a double exponential thin disc is given by eq. 2.5. We can evaluate its density in the equatorial plane as:

$$\rho_\star(R,0) = \rho_{\star,0}\exp\left(-\frac{R}{R_\star}\right) \tag{3.10}$$

where the central density is $\rho_{\star,0} = \frac{M_\star}{4\pi z_\star R_\star^2}$. Figure 3.1a provides the volume density profile of our model of the Milky Way stellar disc. The circular velocity for an exponential disc (Freeman 1970) is given by:

$$v_{c,\star}(R) = x\sqrt{\pi G \Sigma_{\star,0} R_\star \left[I_0\left(\frac{x}{2}\right)K_0\left(\frac{x}{2}\right) - I_1\left(\frac{x}{2}\right)K_1\left(\frac{x}{2}\right)\right]} \tag{3.11}$$

where $\Sigma_{\star,0}$ is the central surface density (see Table 2.2), I and K are the modified Bessel functions of the first and second kind and $x = \frac{R}{R_\star}$. Figure 3.1b shows that the circular velocity rises out to $\sim 2R_\star$ and falls at large radii.

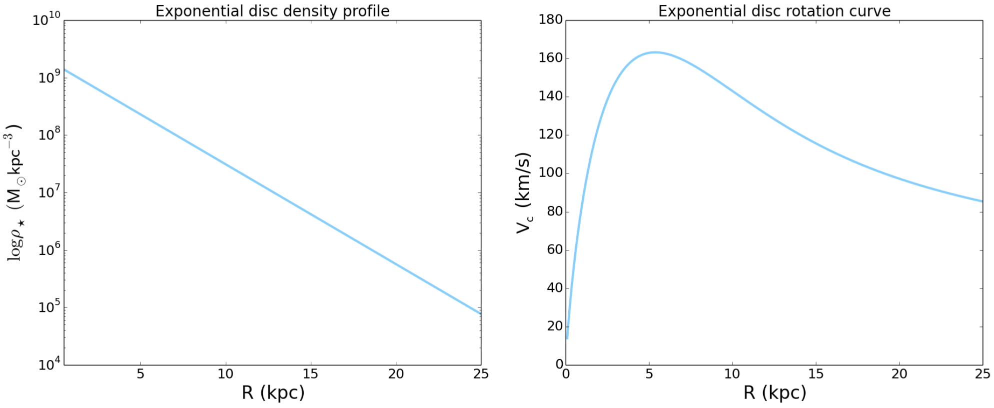

(a) Density distribution.

(b) Rotation curve.

Figure 3.1: *Left*: density distribution (eq. 3.10) for the stellar disc adopted in this thesis (see Table 2.2). *Right*: disc rotation curve (eq. 3.11).

As a consequence, the rotational density contribution to ρ_{eff} is not negligible and it can be calculated through eqs. 3.6 and 3.11:

$$\rho_{\text{rot}}(x) = -\frac{\Sigma_0}{2R_\star}\sqrt{I_0\left(\frac{x}{2}\right)K_0\left(\frac{x}{2}\right) - I_1\left(\frac{x}{2}\right)K_1\left(\frac{x}{2}\right)}\,\frac{\partial\sqrt{I_0\left(\frac{x}{2}\right)K_0\left(\frac{x}{2}\right) - I_1\left(\frac{x}{2}\right)K_1\left(\frac{x}{2}\right)}}{\partial x} \tag{3.12}$$

Eq. 3.12 leads to a form for eq. 3.8:

$$\eta_\star = \frac{e^x}{8T_\star}\left(xA\left(\frac{x}{2}\right) + 8B\left(\frac{x}{2}\right)\right) \tag{3.13}$$

where $A\left(\frac{x}{2}\right) = 3K_0I_1 + K_2I_1 - 3K_1I_0 - I_2K_1$ and $B\left(\frac{x}{2}\right) = I_0K_0 - I_1K_1$. We define the thickness factor $T_\star$ the ratio between the scale lenght and the scale height of the stellar disc. $T_\star$ is equal to 8.33 for our Galaxy model. As shown in Figure 3.2a, $\eta_\star$ is negative where the rotation curve rises ($0 < R \lesssim 2R_\star$), and positive where the circular velocity falls. Then, we can write the vertical acceleration through eqs. 3.6 and 3.13:

$$g_z(R) = -4\pi G\rho_\star(R,0)(1+\eta_\star(R))z \tag{3.14}$$

Figure 3.2b shows g_z at four fixed radii: 5 kpc, 10 kpc, 15 kpc and 20 kpc. The light blue lines represent the vertical accelerations without $\rho_{\rm rot}$, while the black ones are g_z calculated using eq. 3.14. It is clear that the rotational density contribution is slight in the inner parts of the disc (e.g. 5 kpc) but it becomes important in the outer regions.

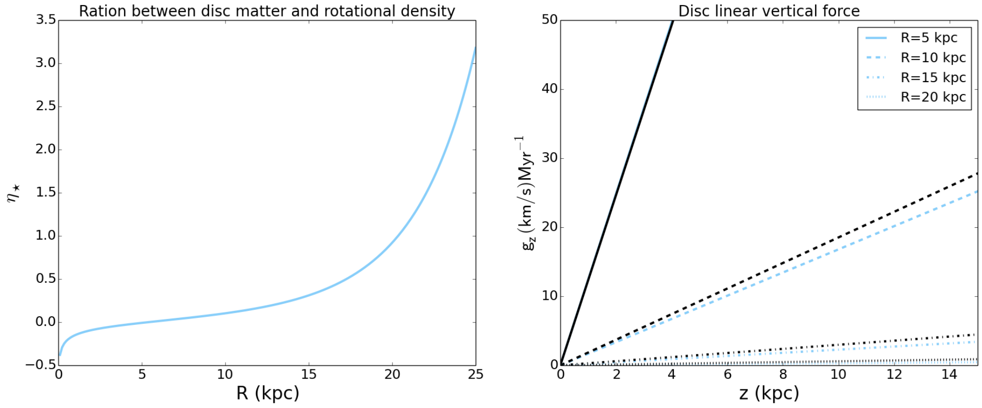

(a) Ratio between $\rho_{\rm rot}$ and $\rho_\star$.

(b) Vertical acceleration.

Figure 3.2: *Left*: the parameter $\eta_\star$ (eq. 3.13) as a function of the radius. *Right*: the linear g_z (eq. 3.14) with (black) and without (light blue) $\rho_{\rm rot}$ at four different radii. The stellar disc parameters are reported in Table 2.2.

Constant vertical acceleration

As mentioned in Section 2.1.1, the gravitational pull of an exponential disc becomes less and less strong as a function of the radius (see Figure 2.3), so fountain particles are expected to reach higher and higher heights. In this case, we can approximate the disc density profile to that of a razor-thin disc with surface density $\Sigma(R)$ equal to the surface density of our exponential disc. Then, if the maximum heights reached by the particles are much lower than the disc extension, we can also consider the disc as a infinite plane.

In order to obtain the vertical acceleration, let us consider an infinite razor-thin disc with an uniform surface density profile Σ. We can apply the Gauss theorem to the gravitational field to estimate its vertical acceleration:

$$\int_S \vec{g} \cdot d\vec{S} = -4\pi G \int_V \rho dV \tag{3.15}$$

where $\vec{g}$ is the gravitational acceleration and $d\vec{S}$ is the unit vector perpendicular to a Gaussian surface with volume V. The Gaussian surface is a closed two-dimensional surface over which the integration is performed. In this case, we choose a cylinder with the curved edge and the flat sides respectively perpendicular and parallel to our razor-thin disc. In this particular case, $\frac{\partial \Phi}{\partial R}$ is null because we assume an infinite disc with no radial density gradient, so the total radial acceleration g_R is equal to zero. The flux of the gravitational acceleration on the top and on the bottom of the box gives:

$$\int_S \vec{g} \cdot d\vec{S} = -2Ag_z \tag{3.16}$$

Then, the volume density profile of the infinite razor-thin disc can be written as $\rho(z) = \Sigma\delta(z)$, where $\delta(z)$ is the Dirac delta function. The integral at the r.h.s. of eq. 3.15 becomes:

$$\int_V \rho dV = A\Sigma \int_{-z}^{+z} \delta(z)dz = A\Sigma(R)(2\theta(z) - 1) \tag{3.17}$$

where $\theta(z)$ is the Heaviside function, which is equal to 0 where $z < 0$ and to 1 where $z > 0$. So, for $z > 0$, the vertical acceleration is $g_z = -2\pi G\Sigma$. Note that, in this particular case, the rotational density is null as the volume density profile does not depend on R.

Finally, we can calculate the approximated g_z of our model of the Milky Way disc by reintroducing the radial dependence:

$$g_z(R) \approx -2\pi G\Sigma(R) \tag{3.18}$$

This equation corresponds to the gravitational pull towards a razor-thin disc with the same surface density profile as the double-exponential disc model we built in Section 2.1.1. This approximation is valid for relatively small z. Figure 3.3 shows the vertical acceleration (eq. 3.18) for this razor-thin disc.

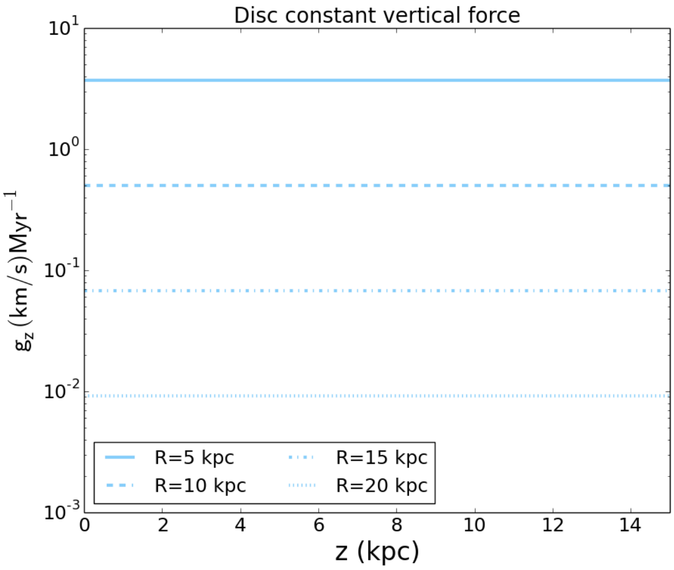

Figure 3.3: Vertical gravitational acceleration of an infinite razor-thin disc with the same surface density as the double-exponential disc model adopted in this thesis (see Table 2.2).

Comparison between analytical and numerical accelerations

In this section we compare the numerical and the analytical vertical accelerations in order to test the validity of our approximations. Figure 3.4a shows this comparison for the case of a linear analytic acceleration (eq. 3.14). Note that, at each radius, the model reproduces *Galforces* results only at very low z, as expected, given the approximation discussed in Section 3.1.1. In Figure 3.4b, we can see that the two trends become very different above z of the order of one scale height ($h_\star = 0.3$ kpc) as the numerical g_z tends to decrease while the analytic one keeps on rising.

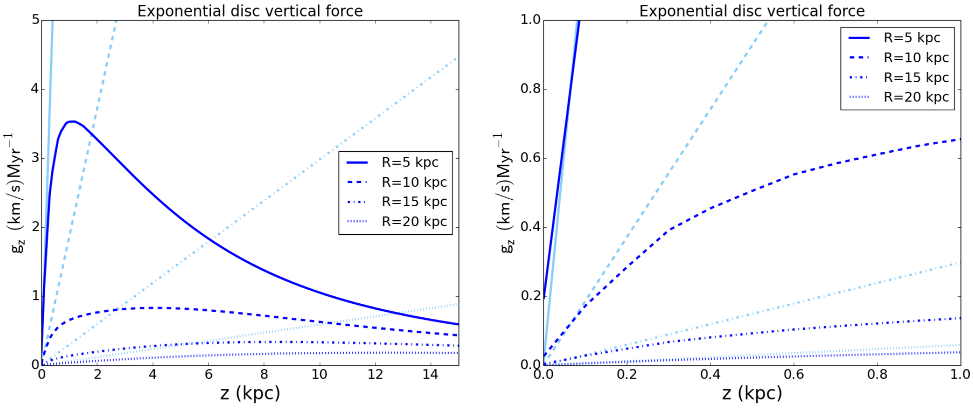

(a) Linear vertical acceleration.

(b) Zoom of 3.4a.

Figure 3.4: *Left*: analytical (light blue) and numerical (blue) accelerations for the Milky Way disc adopted in this thesis (see Table 2.2). *Right*: detail of the inner 1 kpc of the left panel.

Let us consider now the approximation of a constant acceleration (eq. 3.18). In Figures 3.5a and 3.5b, we can see that the constant gravitational acceleration does not reproduce the numerical trend. It however represent a mean value of the vertical acceleration in some parts of the disc, for example at $R = 10$ kpc, but it overestimates the numerical g_z in the central parts (e.g. $R = 5$ kpc) and underestimates the vertical acceleration in the outer regions (e.g. $R = 10 - 15$ kpc).

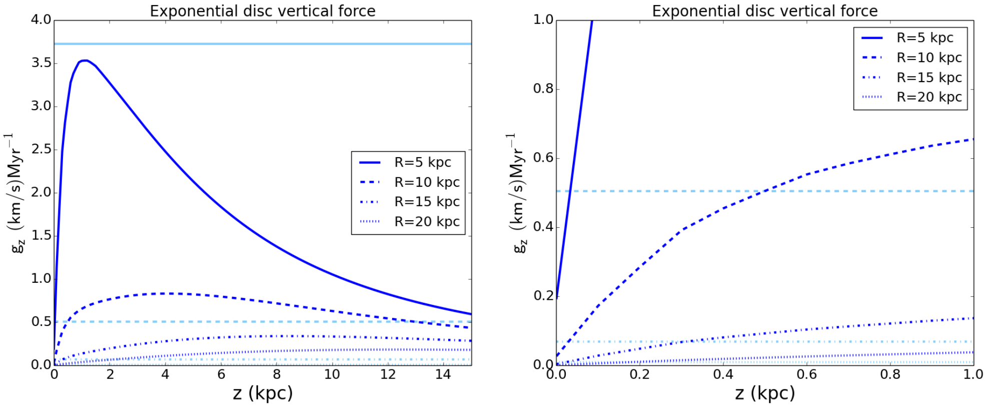

(a) Constant vertical acceleration.

(b) Zoom of 3.5a.

Figure 3.5: Same as 3.4.

In conclusion, a linear g_z does not describe (strongly overestimantes) the numerical acceleration at high z. On the other hand, the numerical g_z is underestimated by the analytic constant g_z in the outer parts of the disc, and overestimanted in the inner regions.

3.1.2 The dark matter halo

In this section, we aim to build an analytical form for the vertical acceleration due to the potential of a dark matter halo. In Section 2.1.2, we have chosen a NFW density profile and a spherical shape for the dark matter halo, so $\rho_{\rm DM}$ depends on the spherical radius r:

$$\rho_{\rm DM}(r) = \frac{\rho_{0,\rm DM}}{\left(\frac{r}{r_s}\right)\left(1+\frac{r}{r_s}\right)^2} \tag{3.19}$$

where $\rho_{0,\rm DM}$ is the halo characteristic density and and r_s is the scale lenght. Figure 3.6 shows the halo density profile as a function of height above the equatorial plane. Note that, in the outer parts of the galaxy (e.g. $R = 10 - 15$ kpc), the density remains almost constant to its value in the midplane within $z \sim 5 - 6$ kpc. Therefore, we can expect that the approximation $\rho_{\rm DM}(R, z) \approx \rho_{\rm DM}(R, 0)$ would be valid even in those external regions of the galaxy where the particles can reach significant heights.

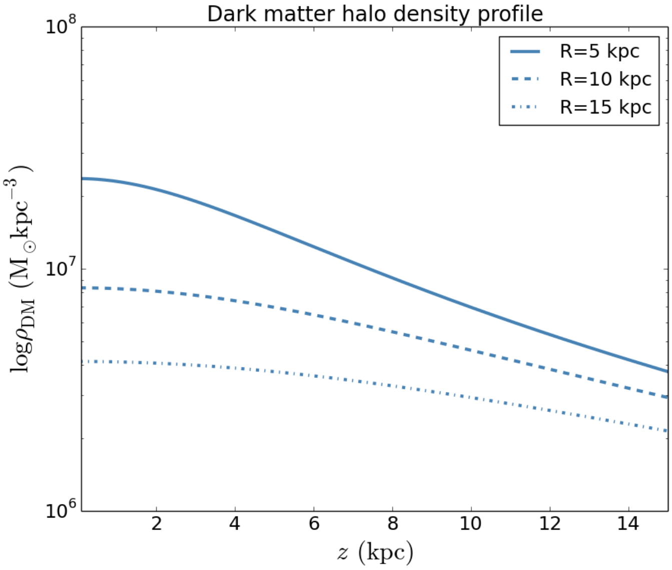

Figure 3.6: Dark matter halo density profile at fixed radii as a function of z (see Table 2.2).

As a result, we can study the halo vertical acceleration performing the same analysis as for the case of the disc linear g_z. In particular, it possible to apply eqs. from 3.1 to 3.8 to the dark matter halo by simply substituting the disc density $\rho_\star$ with the halo density $\rho_{\rm DM}$.
First, we can evaluate the density in the galactic plane, where $r = R$:

$$\rho_{\rm DM}(R, 0) = \frac{\rho_{0,\rm DM}}{\left(\frac{R}{R_s}\right)\left(1+\frac{R}{R_s}\right)^2} \tag{3.20}$$

Figure 3.7a shows the density profile for our halo (see Table 2.2). The rotation curve of a NFW mass distribution is given by:

$$v_c^2(R) = v_{200}^2 \frac{c}{x} \frac{[\log(1+x) - x/(1+x)]}{[\log(1+c) - c/(1+c)]} \tag{3.21}$$

where $x = R/R_s$ and c is the concentration parameter. This parameter is related to the characteristic density $\rho_{0,\mathrm{DM}}$ through:

$$\rho_{0,\mathrm{DM}} = \rho_{\mathrm{crit}}\delta_c \tag{3.22}$$

where $\rho_{\mathrm{crit}} = \frac{3H^2}{8\pi G}$ is the critical density of the Universe and δ_c is the so-called concentration factor:

$$\delta_c = \frac{200}{3}\frac{c^3}{[\ln(1+c) - c/(1+c)]} \tag{3.23}$$

Neto et al. 2007 showed that for the typical range of masses of spiral galaxies ($\mathrm{M_{vir}} = 10^{11} - 10^{12}\mathrm{M}_\odot$) the mean concentration parameter is approximately 10. Assuming an Hubble constant $H = 70\,\mathrm{km\ s^{-1}Mpc^{-1}}$, the characteristic density of our halo is reproduced by a concentration parameter equal to 11.3 (see Table 2.2). Figure 3.7b shows the rotation curve for the dark matter halo adopted in this thesis.

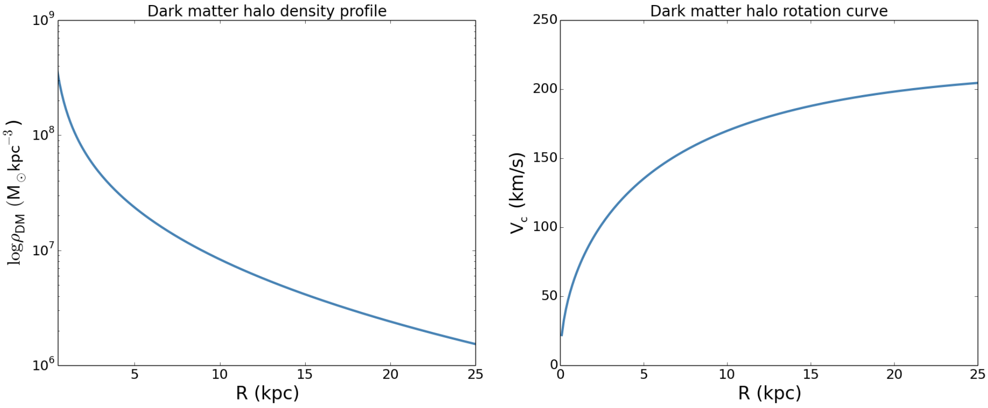

(a) Density distribution.

(b) Rotation curve.

Figure 3.7: *Left*: density distribution (eq. 3.20) for the dark matter halo adopted in this thesis (see Table 2.2). *Right*: halo rotation curve (eq. 3.21).

Then, it is possible to calculate the rotational density:

$$\rho_{\mathrm{rot}} = -\rho_0\left(\frac{x(2x+1) - (1+x)^2\ln(x+1)}{x^3(1+x)^2}\right) \tag{3.24}$$

and η_{DM}:

$$\eta_{\mathrm{DM}} = -\left(\frac{x(2x+1) - (1+x)^2\ln(x+1)}{x^2}\right) \tag{3.25}$$

Figure 3.8a shows that η_{DM} is negative and growing, given that the rotation curve (Figure 3.7b) rises out to 25 kpc. We obtain the linear vertical acceleration for the dark matter halo:

$$g_z(R,z) = -4\pi G\rho_{\mathrm{DM}}(R,0)(1+\eta_{\mathrm{DM}}(R))z \tag{3.26}$$

Figure 3.8b provides the vertical acceleration at four fixed radii (5 kpc, 10 kpc, 15 kpc and 20 kpc) without (blue lines) and with ρ_{rot} (black). It is clear that the rotational density is important both in the inner and in the outer parts as it significantly reduces the effective density.

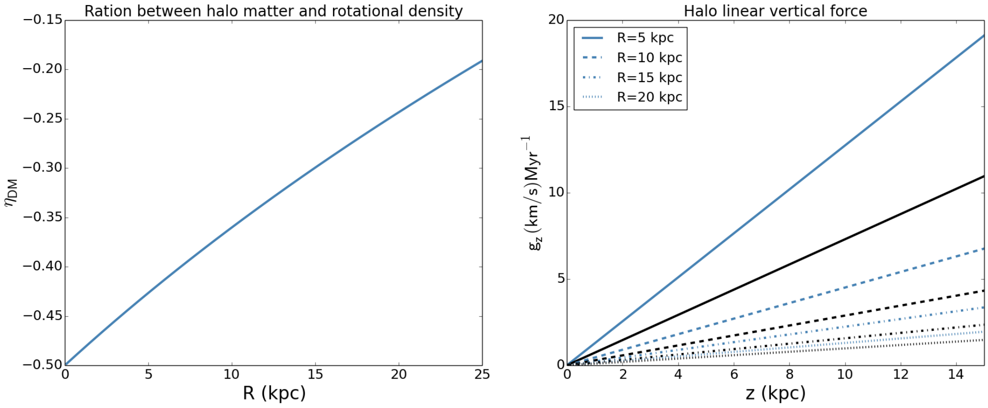

(a) Ratio between $\rho_{\rm rot}$ and $\rho_{\rm DM}$.

(b) Vertical acceleration.

Figure 3.8: *Left*: the parameter $\eta_{\rm DM}$ (eq. 3.25) as a function of the radius. *Right*: the linear vertical acceleration (eq. 3.26) with (black) and without (blue) $\rho_{\rm rot}$. The dark matter halo parameters are reported in Table 2.2.

Comparison between analytical and numerical accelerations

This comparison can help us to understand the validity of our approximations for the Milky Way dark matter halo. Figure 3.9 contrasts the numerical and analytical accelerations (eq. 3.26). Note that the analytical approximation reproduces *Galforces* results up to a certain height, which depends on R. Above that height, at all the radii, the two trends become very different and the numerical acceleration tend to decrease while the analytic g_z keeps on rising.

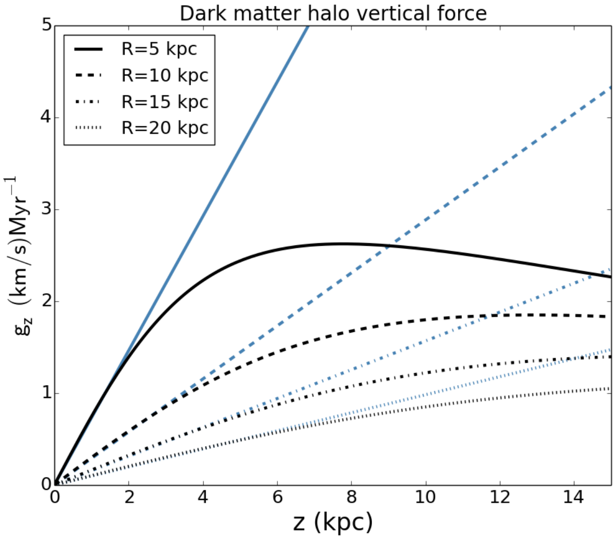

Figure 3.9: Analytical (blue) and numerical (black) accelerations for the dark matter halo adopted in this thesis (see Table 2.2).

In conclusion, we can expect that the gravitational pull effect on fountain orbits will be well described by the linear g_z, if they do not reach very high z.

3.1.3 Two-component model

As mentioned in Section 2.1, our Galaxy model is made up of two main mass components: a stellar disc and a dark matter halo. We aim to model the whole Galactic potential and its gravitational accelerations, so both the components must be taken into account. In Section 2.1.1, we followed two approaches to find the analytical g_z for the disc potential, the first yields a constant vertical acceleration while the second a linear form. In this section we combine these two forms (eqs. 3.14 and 3.18) with that for the halo vertical acceleration (eq. 3.26).

Stellar disc linear acceleration

If we assume that both the disc and the halo accelerations linearly depend on z, we can easily combine them by adding the density profiles (Figure 3.10a):

$$\rho_{\text{tot}} = \rho_\star + \rho_{\text{DM}} \tag{3.27}$$

Then, the total rotation curve (Figure 3.10b) is given by the quadratic sum of the two single components:

$$v^2_{\text{c,tot}} = v^2_{\text{c},\star} + v^2_{\text{c,DM}} \tag{3.28}$$

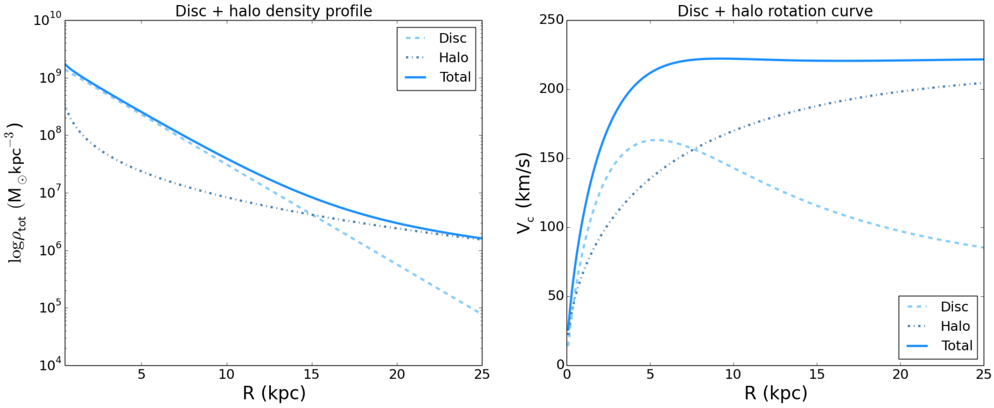

(a) Density distributions. **(b)** Rotation curves.

Figure 3.10: *Left*: density profiles in the plane $z = 0$ for the disc (dashed line), the halo (dot-dashed line) and the two-component (solid line) models (see Table 2.2). *Right*: rotation curves.

Thus, it is possible to evaluate the rotational density (eq. 3.6) and η_{tot}, which is:

$$\eta_{\text{tot}} = \frac{\rho_{\text{rot},\star} + \rho_{\text{rot,DM}}}{\rho_\star + \rho_{\text{DM}}} \tag{3.29}$$

Figure 3.11a shows that the contribution of ρ_{rot} to ρ_{eff} is about 20-40 % in the inner parts of the disc, where the circular velocity is rising. On the other hand, it becomes negligible at larger radii, where the rotation curve is nearly flat (see Figure 3.10b). Then, we can calculate the vertical acceleration for the whole two-component model as:

$$g_z(R, z) = -4\pi G\rho_{\text{tot}}(R, 0)(1 + \eta_{\text{tot}}(R))z \tag{3.30}$$

In Figure 3.11b, the black lines represent the vertical acceleration with (eq. 3.30) and the blue lines without $\eta_{\rm tot}$: note that this correction is essentially negligible from about 5 kpc to 25 kpc.

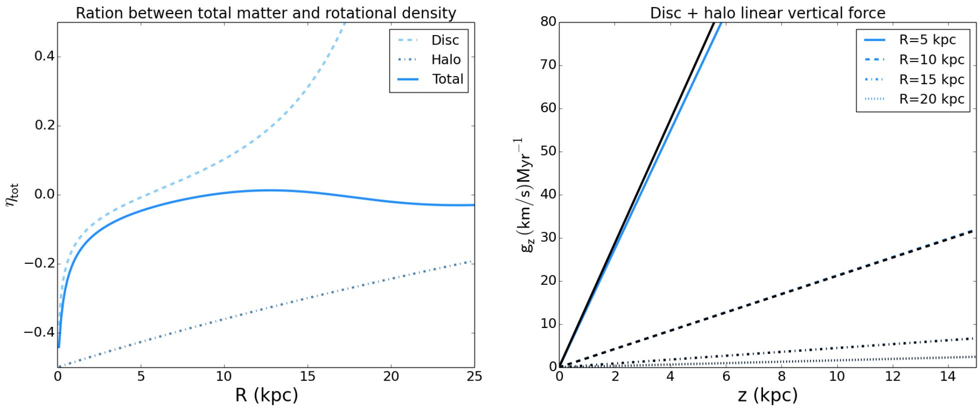

(a) Ratios between $\rho_{\rm rot}$ and $\rho_{\rm tot}$. **(b)** Vertical accelerations.

Figure 3.11: *Left*: the parameters $\eta_\star$, $\eta_{\rm DM}$ and $\eta_{\rm tot}$ (eq. 3.29) as a function of radius. *Right*: the vertical acceleration (eq. 3.30) with (black) and without (blue) $\eta_{\rm tot}$. All the parameters of the models are reported in Table 2.2.

Stellar disc constant acceleration

Alternatively, we can combine the halo linear vertical acceleration with the disc constant g_z. In this case, the gravitational pull (Figure 3.12a) becomes:

$$g_z(R,z) = -4\pi G\rho_{\rm DM}(R,0)(1+\eta_{\rm DM}(R))z - 2\pi G\Sigma_\star(R) \tag{3.31}$$

In eq. 3.31, we include only the rotational density of the dark matter halo while that of the disc is null as we have approximated the disc to a razor-thin infinte layer with constant uniform density.

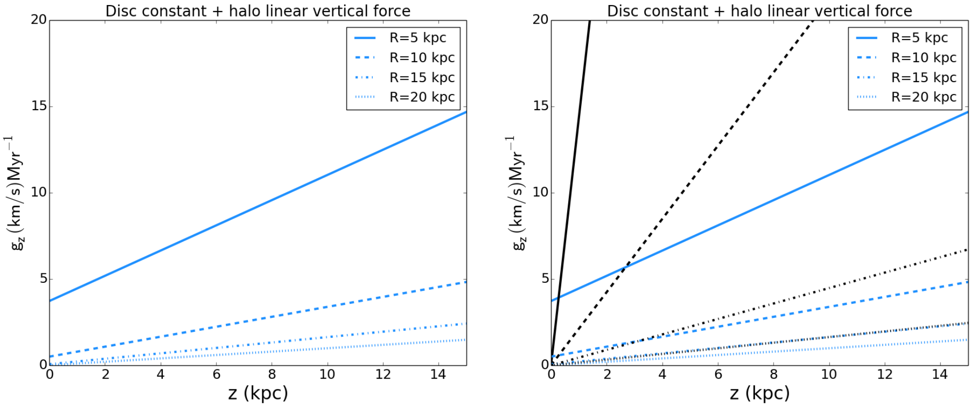

(a) **(b)**

Figure 3.12: *Left*: vertical acceleration (eq. 3.31) for the two-component potential (Table 2.2). *Right*: comparison between the vertical acceleration for the two-component potential as calculated with the linear g_z (black) for the disc (eq. 3.30) and that with the constant g_z (blue, eq. 3.31).

Figure 3.12b provides a comparison between the situation with constant disc acceleration and that with the linear one. It is clear that the difference is significant out to ~ 15 kpc, while it becomes slighter only in the outermost regions.

Comparison between analytical and numerical accelerations

We compare the numerical and the analytical results in order to understand which of the two forms for the vertical acceleration describe better our model of the Milky Way.

Figure 3.13a compares the numerical gravitational pull and the analytic one, which is calculated with a linear g_z for both the disc and the halo (eq. 3.30) and it includes $\eta_{\rm tot}$ (eq. 3.29). In this case, the acceleration is strongly overestimated above a few hundred parsecs in the inner parts and 1-2 kpc in the outermost regions.

On the contrary, the combination of the linear g_z for the halo with a constant for the disc (Figure 3.13b) appears to describe well the numerical g_z for a larger range of z at least for $R > 5$ kpc. Note that, at $R = 10$ kpc, 15 kpc and 20 kpc, the analytic predictions underestimate the vertical acceleration up to $z \sim 6$ kpc, $z \sim 9$ kpc and $z \sim 11$ kpc respectively.

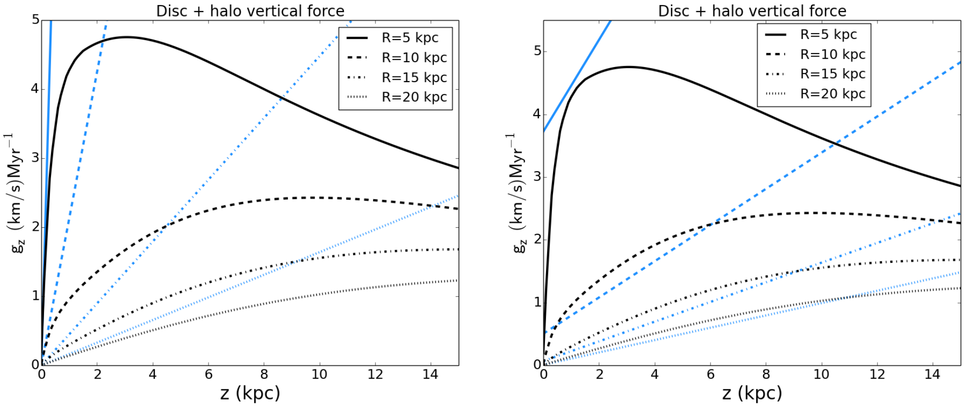

(a) **(b)**

Figure 3.13: Comparison between the analytical (blue) and numerical vertical accelerations (black) for the two-component potential (see Table 2.2). *Left*: the total analytical acceleration (eq. 3.30) is obtained with the linear forms for the disc and the halo components. *Right*: the total analytical g_z (eq. 3.31) is the sum of the constant form for the disc and the linear form for the halo.

In this two-component model, the disc volume density profile causes a strong overestimate of the vertical acceleration (see Figure 3.4). We can conclude that the bi-linear approximation does not describe the numerical vertical acceleration. On the other hand, the constant-linear combination could be suitable to reproduce the numerical g_z for those fountain particles that reach relatively low heights above the equatorial plane.

3.2 Analytical galactic fountain and orbital time

Our aim is to build a model for the galactic fountain in order to obtain an equation for the orbital time of the clouds as a function of radius. This quantity is fundamental to understand how much angular momentum is lost by the clouds and how much coronal material is condensed. Unfortunately, fountain clouds that leave the equatorial plane have more complicated orbits than those in the plane, which have the classical rosette shape. We can semplify the problem by making the same assumptions as done for the numerical potential (see Section 2.3) and the orbits (see Section 2.2). Our approximations can be summarised as follows.

1. Axisymmetric system.
2. Planar symmetry with respect to the equatorial plane.
3. Fountain clouds are represented as particles.
4. The clouds are ejected from the plane with initial velocity $v_{\rm kick} = 80$ km s^{-1} and in a direction completely normal to the plane.

The assumption 1 entails that the azimuthal gradients of the potential is null. Then, the introduction of the rotational density allows us to take account of the radial gradient of the potential in the midplane. In addition, the radial displacement of the orbits with respect to their kick radius is essentially negligible, except for the disc case, in which the particles returns to the disc at a radius much larger than $R_{\rm kick}$ (see 2.3.1). Therefore, for the sake of semplicity, we limit our analysis of the orbits to the vertical direction, introducing a fifth approximation:

5. The motion takes place only along z.

At this point, we can write the equation that describes the motion of the fountain particles as:

$$\ddot{z}(t) = g_z(R, z(t)) \tag{3.32}$$

where g_z is the vertical acceleration that we obtained in Section 3.1. Eq. 3.32 is a second order ordinary differential equation (ODE) in z, which is the position of the particle, with constant coefficient [1]. Then, we know the initial conditions ($t = 0$) of the orbits as the particles are kicked out from the equatorial plane ($z = 0$) with $v_{\rm kick}$:

$$z(0) = 0 \tag{3.33a}$$

$$\dot{z}(0) = v_{\rm kick} \tag{3.33b}$$

Therefore, the analytical integration of these orbits is an initial value Cauchy problem and its solution exists and is unique.

Following the same strategy as in Section 2.3, first we analise the pure fountain, then we try to improve the model by including drag and accretion.

---

[1] The coefficient will be constant with z but not with R

3.2.1 Pure fountain

In this section, we introduce a theoretical model for the pure fountain, which does not include any coronal interaction. This is the base case crucial to test our model and understand the behaviour of fountain clouds. Following the same approach as in Section 3.1, we first analise the disc and halo individually, then we combine them together in order to study the fountain in the whole Galactic potential.

The stellar disc

In Section 3.1.1, we introduced two ways to estimate the vertical acceleration due to a disc mass distribution. Therefore, we can obtain two equations for the orbital time: the first with a linear g_z, which should describe the orbits in the innermost regions, and the second with a constant g_z, which should be more suitable for the orbits in the other parts of the disc.

Linear vertical acceleration

First, we analise the linear form for g_z (eq. 3.14). We can write the Cauchy problem that describe the behaviour of the single orbits as:

$$\begin{cases} \ddot{z} = -4\pi G\rho_\star(1+\eta_\star)z \\ z(0) = 0 \\ \dot{z}(0) = v_{\text{kick}} \end{cases} \tag{3.34}$$

It is clear that this equation describes an harmonic oscillator in the z-direction:

$$\ddot{z} + \omega_\star^2 z = 0 \tag{3.35}$$

where the angular frequency $\omega_\star$ is defined as $\omega_\star^2 = 4\pi G\rho_\star(1+\eta_\star)$ and it hides the dependence on galaxy radius through the density profile, so $\omega_\star = \omega_\star(R)$. Note that the numerical integration of the orbits up to 1 Gyr (see Appendix A) already suggested the harmonic oscillator to describe the particle motion. Then, the assumed solution of this Cauchy problem is $z(t) = e^{\lambda t}$, thus the characteristic polynomial can be written as:

$$\lambda^2 + \omega_\star^2 = 0 \tag{3.36}$$

The polynomial roots of eq. 3.36 are $\lambda_{1,2} = \pm i\omega_\star$, so the solution and its derivative are:

$$z(t) = C_1 e^{-i\omega_\star t} + C_2 e^{i\omega_\star t} \tag{3.37a}$$

$$\dot{z}(t) = -i\omega_\star C_1 e^{-i\omega_\star t} + i\omega C_2 e^{i\omega_\star t} \tag{3.37b}$$

The constants C_1 and C_2 can be calculated through the initial conditions (eq. 3.33):

$$\begin{cases} C_1 + C_2 = 0 \\ -i\omega_\star C_1 + i\omega_\star C_2 = v_{\text{kick}} \end{cases} \Rightarrow \begin{cases} C_1 = -\frac{v_{\text{kick}}}{2i\omega_\star} \\ C_2 = -C_1 = \frac{v_{\text{kick}}}{2i\omega_\star} \end{cases}$$

Therefore, through the Euler's formula $\sin x = \frac{e^{ix}-e^{-ix}}{2i}$, the solution and its derivative can be written as:

$$z(t) = \frac{v_{\text{kick}}}{\omega_\star}\sin(\omega_\star t) \tag{3.38a}$$

$$\dot{z}(t) = v_z(t) = v_{\text{kick}}\cos(\omega_\star t) \tag{3.38b}$$

These solutions correspond to periodic motions that repeat themselves as sinusoids with constant amplitudes. Figures 3.14a and 3.14b illustrate $z(t)$ and $v_z(t)$ calculated at radii 5 kpc, 10 kpc and 15 kpc using eqs. 3.38a and 3.38b. As expected, the maximum height increases as a function of the kick radius, as the vertical pull to the disc weakens, and the vertical velocity ranges from 80 km s^{-1} to -80 km s^{-1}.

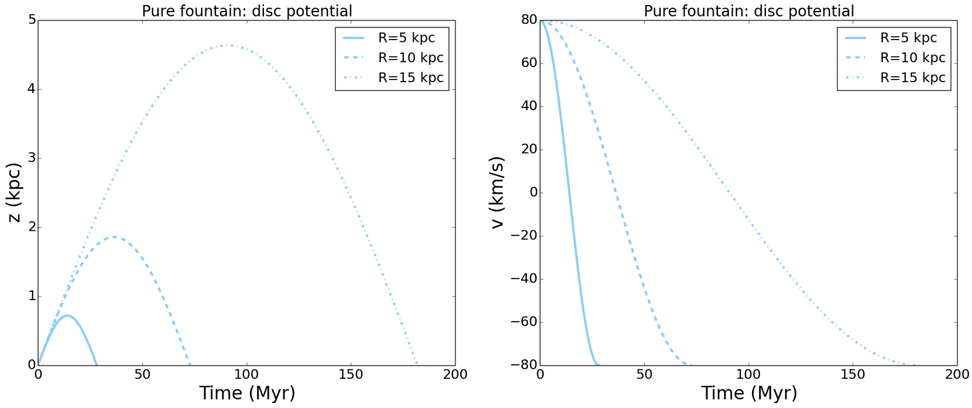

(a) Orbits $z(t)$. **(b)** Velocities $v_z(t)$.

Figure 3.14: Pure fountain orbits (left) and vertical velocities (right) at fixed radii in the presence of a linear vertical acceleration of the disc potential adopted in this thesis (see Table 2.2).

The first zero of eq. 3.38a provides the time to cross the midplane (orbital time) at the end of the orbits:

$$\sin(\omega_\star t) = 0 \Leftrightarrow \omega_\star t = \pi$$

So, we find that the orbital time in the presence of a disc density distribution $\rho_\star$ is:

$$t_{\text{orb},\star}(R) = \frac{\pi}{\sqrt{4\pi G\rho_\star(R,0)(1+\eta_\star(R))}} \tag{3.39}$$

Note that $t_{\text{orb},\star}$ does not explicitly depends on the kick velocity while the heights reached by the particles does. Therefore, the inital velocity is crucial in establishing the validity of our model: the higher is the velocity, the larger are the heights reached by the particles, so our approximation becomes progressively rougher.

Figure 3.15 shows the theoretical orbital time calculated using eq. 3.39.

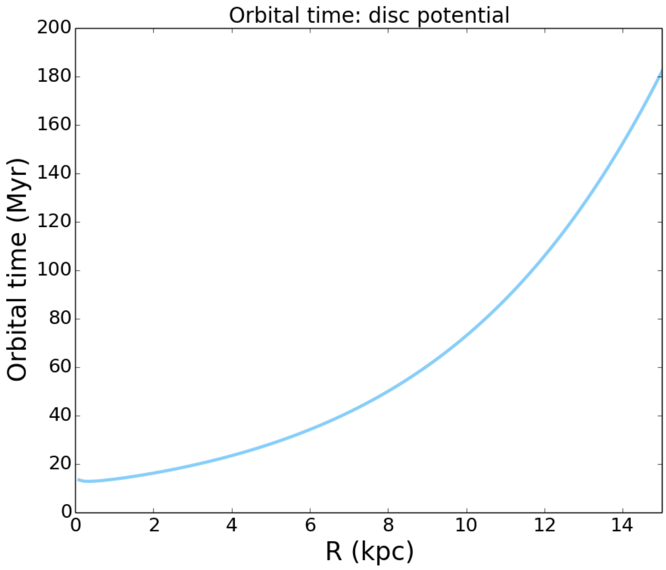

Figure 3.15: Pure fountain orbital time as a function of radius (eq. 3.39) and in the presence of a linear vertical acceleration for disc potential (see Table 2.2).

Constant vertical acceleration

Let us now consider g_z as constant with z (eq. 3.18). As mentioned in Section 3.1.1, we expect that the constant form for the vertical acceleration should approximately describe g_z in the outermost parts of a disc, where the particles can reach significant heights. In other words, they experience the effect of the vertical acceleration of an infinitely razor-thin disc with the same surface density of the double-exponential disc adopted so far. Therefore, the equation of motion can be written as:

$$\ddot{z}(t) = -2\pi G\Sigma(R) \tag{3.40}$$

The solution can be found by integrating two times eq. 3.40 from $t = 0$ to t and taking into account the initial conditions (eq. 3.33). Thus, we obtain the vertical velocity as a function of time:

$$\int_{\dot{z}(0)}^{\dot{z}} dz = -\int_0^t 2\pi G\Sigma(R)dt$$

$$\dot{z}(t) = v_z(t) = v_{\rm kick} - 2\pi G\Sigma(R)t \tag{3.41}$$

and the particles position as a function of time [2]:

$$z(t) = v_{\rm kick}t - \pi G\Sigma(R)t^2 \tag{3.42}$$

Figure 3.16a shows the orbits in the presence of this constant vertical acceleration. Note the dramatic increase of the maximum height as g_z becomes very weak in the outer parts of the disc.

---

[2] Note that these solutions (eqs. 3.41 and 3.42) have the same form as that for a body under the influence of Earth's gravity.

Figure 3.16b provides the vertical velocities at three fixed radii. Note that the orbits correspond to an uniformly decelerated motion, so v_z linearly decreases with time.

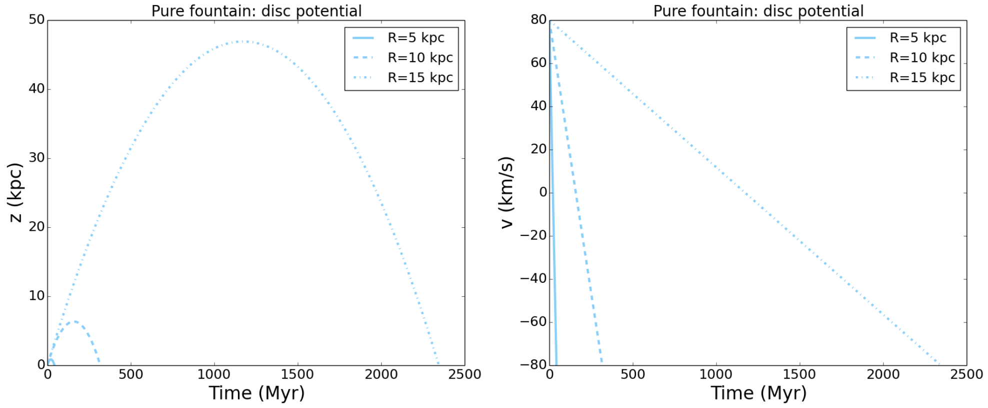

(a) Orbits $z(t)$. **(b)** Velocities $v_z(t)$.

Figure 3.16: Pure fountain orbits (left) and vertical velocities (right) at fixed radii in the presence of a constant vertical acceleration.

The orbital time can be found by solving the equation $z(t) = 0$, which has two solutions: $t = 0$, when the particle is in the plane at the moment before the ejection, and the orbital time $t_{\mathrm{orb},\star}$:

$$t_{\mathrm{orb},\star}(R) = \frac{v_{\mathrm{kick}}}{\pi G \Sigma(R)} \tag{3.43}$$

which can be rewritten as:

$$t_{\mathrm{orb},\star}(R) = 5.43 \left(\frac{v_{\mathrm{kick}}}{80\,\mathrm{km\ s}^{-1}}\right) \left(\frac{1.09 \times 10^9\, M_\odot \mathrm{kpc}^{-2}}{\Sigma_{0,\star}}\right) \exp\left(\frac{R}{R_\star}\right)\ \mathrm{Myr} \tag{3.44}$$

Figure 3.17 compares the linear (eq. 3.39) and the constant (eq. 3.44) forms for orbital time as a function of radius. Note that the two equations give quite different results: the orbital time calculated using eq. 3.44 suddenly shoots up starting form 4 kpc, reaching 600 Myr at $R \approx 12$ kpc, while the other (eq. 3.39) mildly increases.

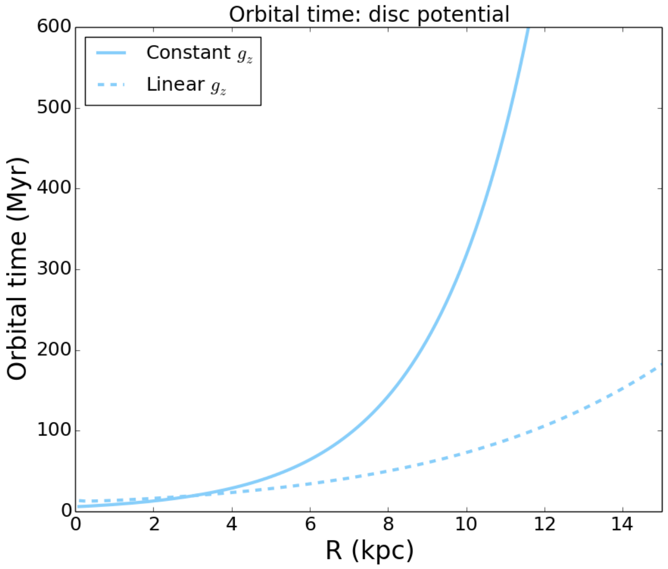

Figure 3.17: Comparison between the linear (dashed, eq. 3.39) and the constant (solid, eq. 3.44) forms for orbital time in the presence of the disc potential alone (see Table 2.2).

Comparison between analytical and numerical orbits

In Figure 3.18, we see a comparison between the orbits $z(t)$ and the velocities at fixed radii: 5 kpc, 10 kpc and 15 kpc.

Let us first consider the orbits calculated with constant g_z (solid). At 5 kpc (Figure 3.18a), the analytical and the numerical orbits are quite different and the analytical model can reach a maximum height that is ~ 35 % of the numerical height. Then, at 10 kpc (Figure 3.18c), the analytical model seems to be a good approximation of the numerical results, at least for the orbital time and the vertical velocity. Finally, our model does not reproduce the numerical orbits at 15 kpc (Figure 3.18e) as both the maximum height and the orbital time dramatically grow.

On the other hand, as expected, the linear form for g_z turns out to be quite a poor approximation, as the analytical predictions are very far from the numerical results at all radii.

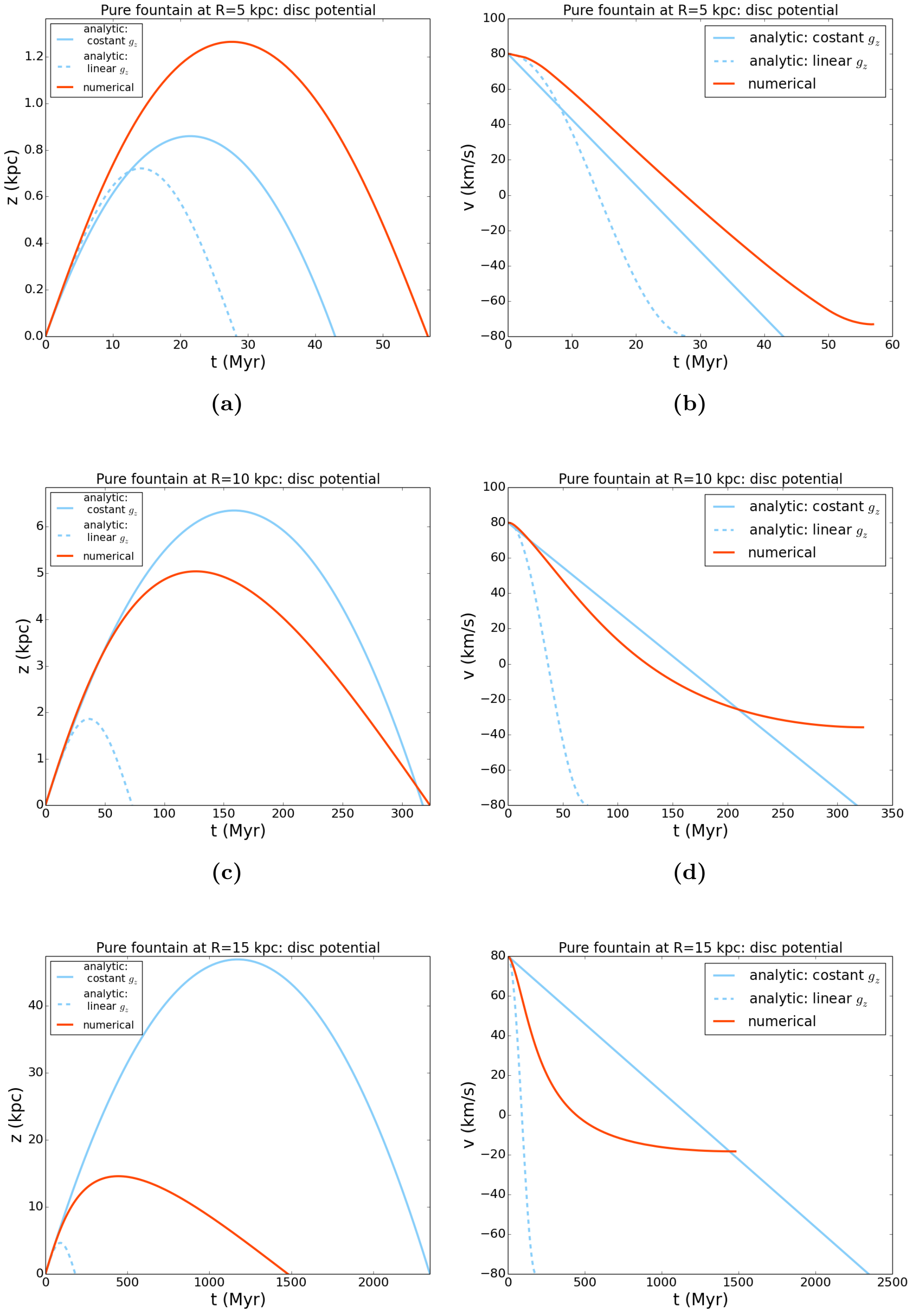

(a) **(b)**

(c) **(d)**

(e) **(f)**

Figure 3.18: Pure fountain orbits (left) and velocities (right) in the stellar disc potential: comparison of analytical (light blue) and numerical (orange) results. The solid lines represent the orbits with the constant vertical acceleration while the dashed lines show the results of the linear approximation.

The dark matter halo

In section 3.1.2, we pointed out that the dark matter density remains almost constant to its value in the midplane up to a scale height that is much higher than that for the disc. Therefore, we can expect that our analytical model successfully reproduces the numerical results. In this case, the particles experience the linear acceleration given by eq. 3.26, so the orbits are described by the following Cauchy problem:

$$\begin{cases} \ddot{z} = -4\pi G\rho_{\mathrm{DM}}(1+\eta_{\mathrm{DM}})z \\ z(0) = 0 \\ \dot{z}(0) = v_{\mathrm{kick}} \end{cases} \tag{3.45}$$

Again, the motion is an harmonic oscillator and the solution is the similar to eq. 3.38a:

$$z(t) = \frac{v_{\mathrm{kick}}}{\omega_{\mathrm{DM}}}\sin(\omega_{\mathrm{DM}}t) \tag{3.46a}$$

$$\dot{z}(t) = v_z(t) = v_{\mathrm{kick}}\cos(\omega_{\mathrm{DM}}t) \tag{3.46b}$$

Figures 3.19a and 3.19b illustrate $z(t)$ and $v_z(t)$ respectively at 5 kpc, 10 kpc and 15 kpc.

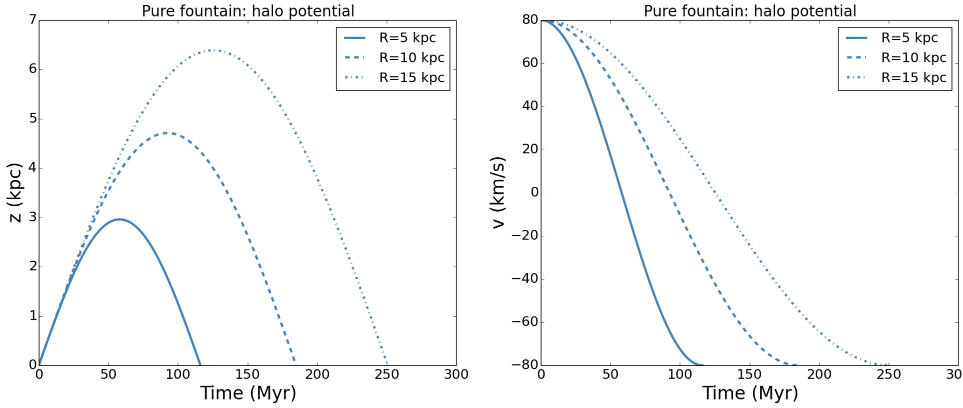

(a) Orbits $z(t)$.

(b) Velocities $v_z(t)$.

Figure 3.19: Pure fountain orbits (left) and velocities (right) at fixed radii in the presence of a linear vertical acceleration for the dark matter halo potential adopted in this thesis (see Table 2.2).

The orbital time equation is identical to that for the disc case (eq. 3.39) except that we must use the halo density profile:

$$t_{\mathrm{orb,DM}}(R) = \frac{\pi}{\sqrt{4\pi G\rho_{\mathrm{DM}}(R,0)(1+\eta_{\mathrm{DM}}(R))}} \tag{3.47}$$

Figure 3.20 shows the orbital time as a function of radius.

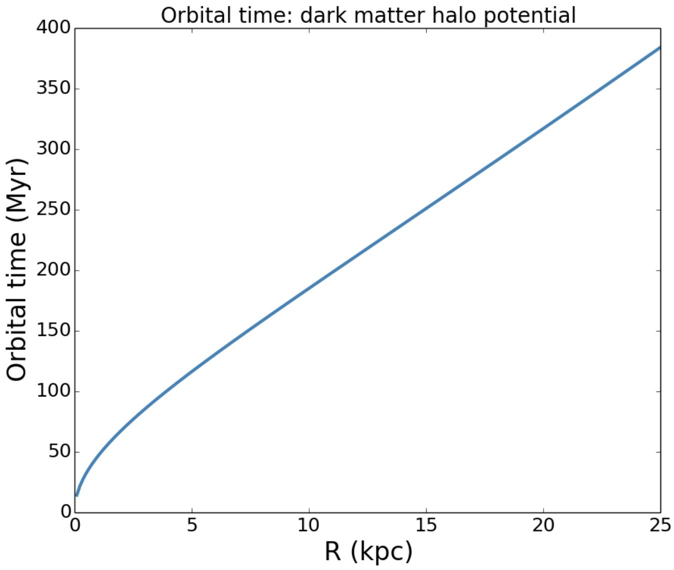

Figure 3.20: Pure fountain orbital time as a function of radius and in the presence of a linear vertical acceleration for the dark matter halo potential adopted in this thesis (see Table 2.2).

Comparison between analytical and numerical orbits

Figures 3.21a, 3.21c and 3.21e show that our model can reproduce the numerical orbits quite well up to $z \sim 2.5$ kpc, $z \sim 4.5$ kpc and $z \sim 6$ kpc for the orbits at $R = 5$ kpc, $R = 10$ kpc and $R = 15$ kpc respectively. Then, the numerical and the analytical results slighly differ in the second part of the orbits (after the maximum height). This difference is due to the combination of two effects: the first is the variation of the density profile of the halo as a function of z (see Figure 3.6), the second is the radial displacement during the orbit, which entails a slight variation of the density. Indeed, during the first part of the orbit (before the maximum height), the dark matter density decreases and it becomes progressively lower than the density in the midplane ($\rho_{\rm DM}(R, z) < \rho_{\rm DM}(R, 0)$). As a result, the analytic vertical acceleration is overestimanted by our model and the analytic orbital time is systematically underestimated. The kick radii of our particles are 5 kpc, 10 kpc and 15 kpc, where the density profile as a function of R would vary significantly with z (see Figure 3.6). These factors also affect the theoretical velocity that are compared to the numerical $v_z(t)$ in Figures 3.21b, 3.21d and 3.21f. As expected, the velocity ranges from 80 km s^{-1} to -80km s^{-1} as the total energy is conserved during the orbits (see Section 2.3.1).

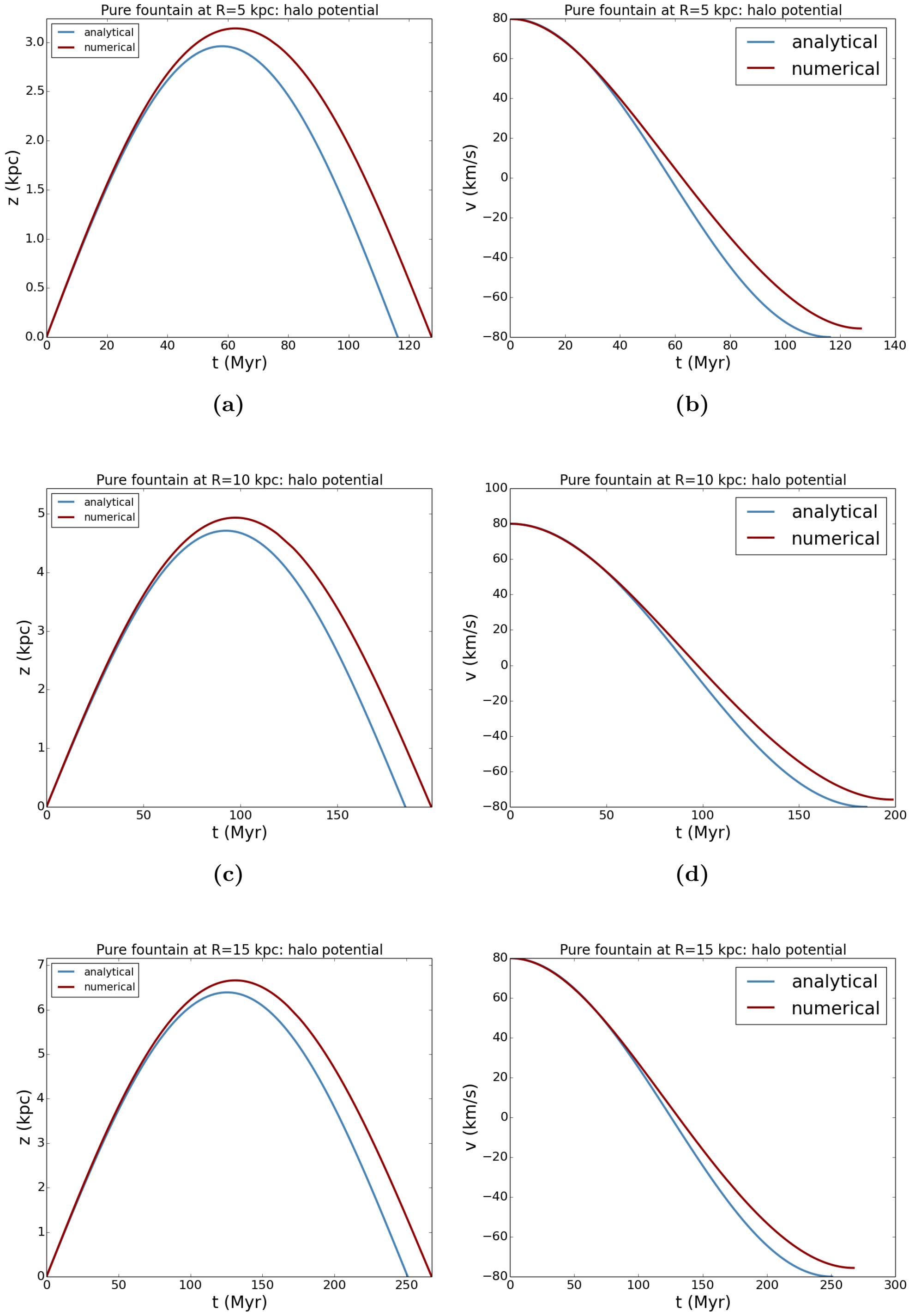

(a) (b)

(c) (d)

(e) (f)

Figure 3.21: Pure fountain orbits (left) and velocities (right) in the presence of the dark matter halo potential: comparison of analytical (blue) and numerical (dark red) results.

Two-component model

In this section, we try to integrate the fountain orbits in the whole Galactic potential in order to obtain an analytical functional form for the orbital time. Following the same approach as in Section 3.1.3, we combine the vertical accelerations for the disc and the halo and we analise the two cases for the disc separately: first the linear (eq. 3.14) and then the constant (eq. 3.18) approximation for the g_z.

Linear vertical acceleration

Let us consider the vertical accelerations of the disc and the halo as linear with z. We can describe the orbits behaviour using the following Cauchy problem:

$$\begin{cases} \ddot{z} = -4\pi G \rho_{\rm tot}(1+\eta_{\rm tot})z \\ z(0) = 0 \\ \dot{z}(0) = v_{\rm kick} \end{cases} \tag{3.48}$$

where $\eta_{\rm tot}$ is the ratio between the rotational density $\rho_{\rm rot,tot}$ and the total density (disc and halo). The solution has the same form as that in eq. 3.39 but the angular frequency of the harmonic oscillator depends on the total density profile:

$$z(t) = \frac{v_{\rm kick}}{\omega_{\rm tot}} \sin(\omega_{\rm tot} t) \tag{3.49a}$$

$$\dot{z}(t) = v_z(t) = v_{\rm kick} \cos(\omega_{\rm tot} t) \tag{3.49b}$$

Figures 3.22a and 3.22b shows $z(t)$ and $v_z(t)$ at 5 kpc, 10 kpc and 15 kpc.

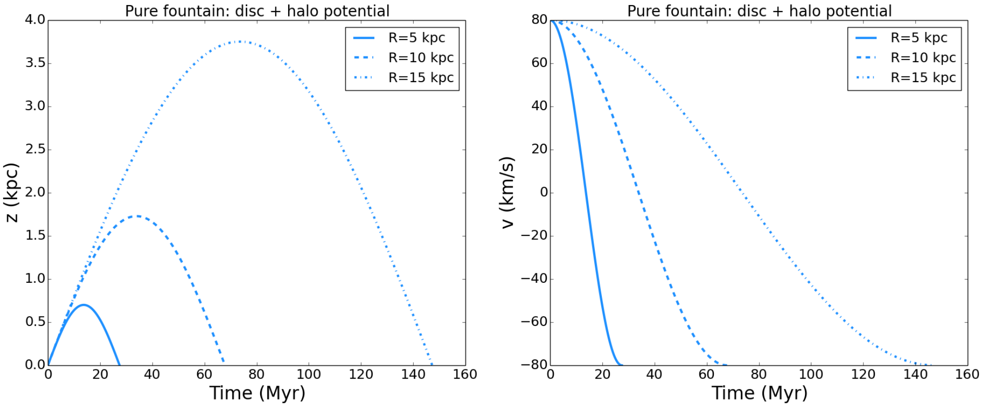

(a) Orbits $z(t)$. **(b)** Velocities $v_z(t)$.

Figure 3.22: Pure fountain orbits (left) and vertical velocities (right) at fixed radii in the presence of the two-component potential (see Table 2.2). The vertical acceleration is linear both for the disc and for the halo.

Then, we can write the orbital time as:

$$t_{\text{orb,tot}}(R) = \frac{\pi}{\sqrt{4\pi G\rho_{\text{tot}}(R,0)(1+\eta_{\text{tot}}(R))}} \tag{3.50}$$

Figure 3.23 shows the orbital time for the whole Galactic potential (eq. 3.50) and compares it to the orbital times for the disc (eq. 3.39) and the halo alone (eq. 3.47). Note that the trend of the total orbital time (eq. 3.50) is determined by the disc in the inner parts and by the halo at larger radii.

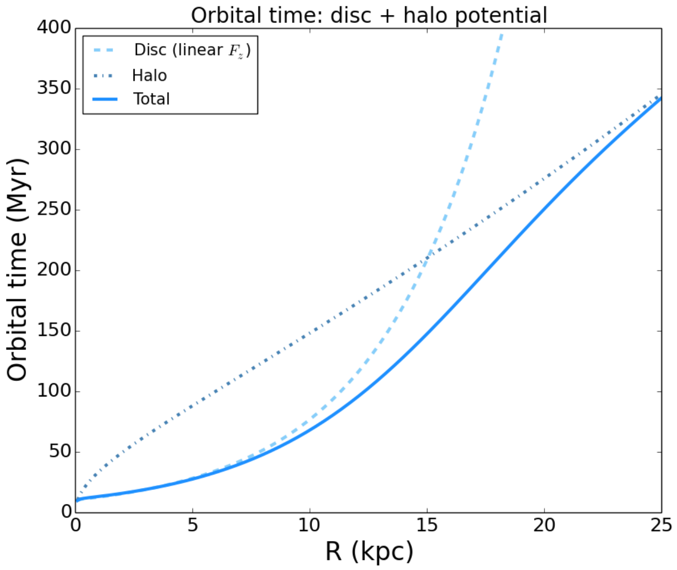

Figure 3.23: Orbital time for the two-component potential: comparison between eq. 3.39 for the disc, eq. 3.47 for the halo and eq. 3.50 for the whole Galaxy.

Constant vertical acceleration

In this section, we analise how the constant approximation for the disc vertical acceleration influence the equation of the motion and the analytical results. If we choose a constant dependence on z for the disc g_z (3.18) and a linear one for the halo g_z (3.26), the equation of motion becomes:

$$\ddot{z}(t) = -2\pi G\Sigma(R) - 4\pi G\rho_{\text{DM}}(R,0)(1+\eta_{\text{DM}}(R))z \tag{3.51}$$

This non homogeneous differential equation is satisfied by the sum of the solution of the homogeneous equation (eq. 3.46a) and a particular solution of eq. 3.51. Therefore, the position of the particles as a function of time is given by:

$$z(t) = \frac{v_{\text{kick}}}{\omega_{\text{DM}}}\sin(\omega_{\text{DM}}t) - \frac{\Sigma(R)}{2\rho_{\text{DM}}(R,0)}(1-\cos(\omega_{\text{DM}}t)) \tag{3.52}$$

where the angular frequency is $\omega_{\text{DM}} = \sqrt{4\pi G\rho_{\text{DM}}(R,0)(1+\eta_{\text{DM}}(R))}$ and $\Sigma(R)$ is the surface density profile of the razor-thin disc described in Section 3.1.1.

Then, the vertical velocity is:

$$\dot{z}(t) = v_z(t) = v_{\rm kick}\cos(\omega_{\rm DM}t) - \frac{\omega_{\rm DM}\Sigma(R)}{2\rho_{\rm DM}(R,0)}\sin(\omega_{\rm DM}t) \tag{3.53}$$

Figures 3.24a and 3.24b illustrate $z(t)$ and $v_z(t)$ respectively. Note that the particles reach higher heights that those for the bi-linear g_z case (see Figure 3.22a) as the razor-thin disc vertical acceleration (eq. 3.18) is lower that the linear approximation (eq. 3.14).

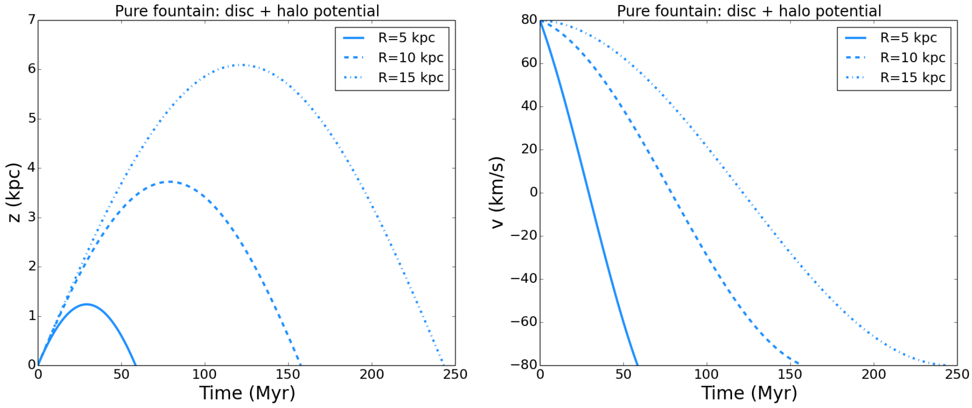

(a) Orbits $z(t)$.

(b) Velocities $v_z(t)$.

Figure 3.24: Pure fountain orbits (left) and velocities (right) at fixed radii in the presence of the two-component potential (see Table 2.2). The vertical acceleration is constant with z for the disc and linear for the halo.

Then, remembering that $\sin x/(1-\cos x) = \cot(x/2)$, we can find the orbital time as:

$$t_{\rm orb,tot}(R) = \left(\frac{2}{\omega_{\rm DM}}\right)\arctan\left(\frac{2\rho_{\rm DM}(R,0)v_{\rm kick}}{\Sigma(R)\omega_{\rm DM}}\right) \tag{3.54}$$

The solid line in Figure 3.25 represents the orbital time (eq. 3.54) in the two-component potential. Note that eq. 3.54 follows the orbital time obtained with the constant approximation (eq. 3.39) out to 5-6 kpc. Then, the solid line becomes nearly linear with R and starts following the halo orbital time (eq. 3.47).

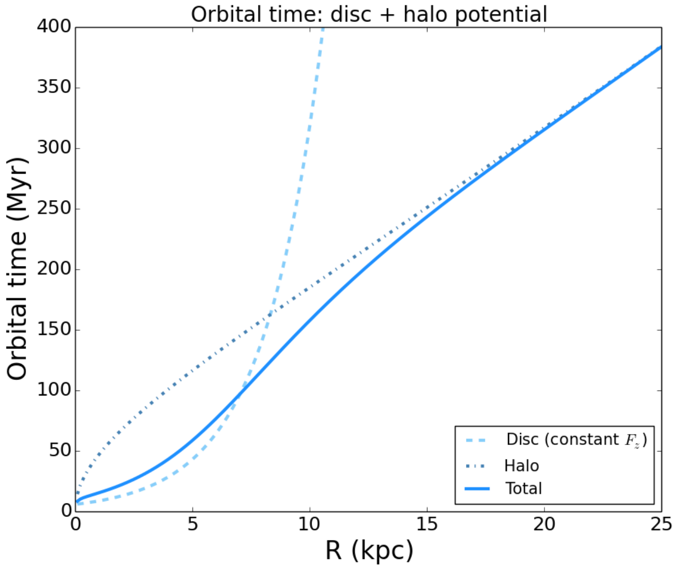

Figure 3.25: Orbital time for the two-component potential: comparison between eq. 3.39 for the disc, eq. 3.47 for the halo and eq. 3.54 for the whole Galaxy.

Comparison between analytical and numerical orbits

Figures 3.26a, 3.26c and 3.26e provide a comparison between the numerical (red) and the analytical orbits (blue).

Let us consider the case with the linear approximation for both the disc and the halo (dashed lines): the analytical orbits reproduce the numerical trends only up to $z \sim 0.3$ kpc, $z \sim 1.5$ kpc and $z \sim 3$ kpc. Beyond these heights, it is clear that the vertical acceleration is dramatically overestimanted by the linear approximation as the analytical trajectories are much shorter than the numerical orbits.

On the other hand, the solid blue lines represent the orbits and the vertical velocities obtained using the constant approximation for the disc g_z. Note that, at 5 kpc, the vertical acceleration is slightly underestimated with respect to the numerical results, so the particle reaches $z \sim 1.2$ kpc instead of $z \sim 1.1$ kpc. Then, at 10 kpc and 15 kpc, the analytic predictions well reproduce the numerical orbits and the vertical velocities, although there is a slight difference between the predicted and the numerical maximum heights of $\gtrsim 0.5$ kpc.

In conclusion, the combination of the constant g_z for the disc and the linear g_z for the halo provides an equation for the orbits that can successfully reproduce the numerical orbits calculated by *Extragas*.

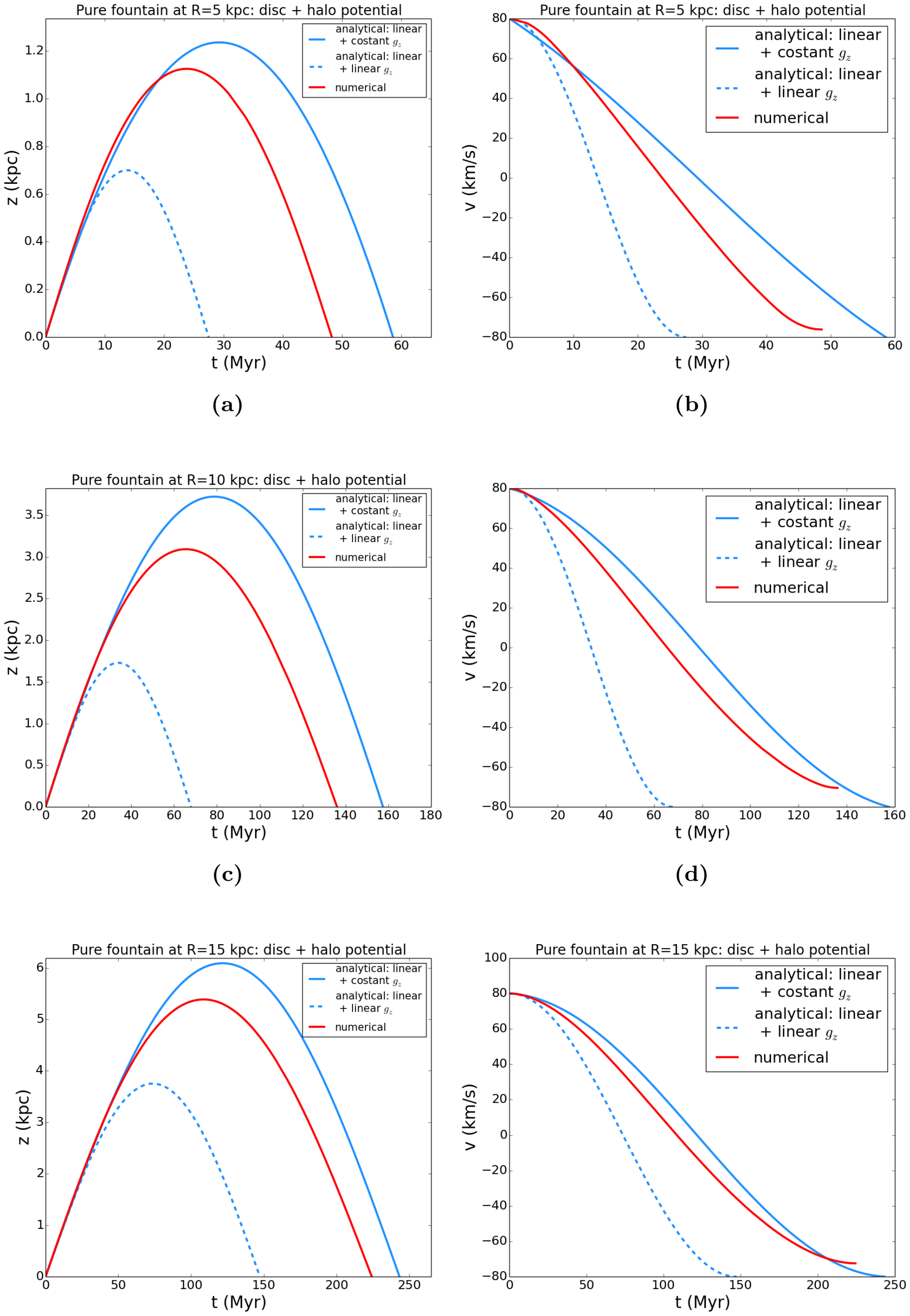

(a) **(b)**

(c) **(d)**

(e) **(f)**

Figure 3.26: Pure fountain orbits (left) and velocities (right) in the presence of the two-component potential: comparison of analytical (blue) and numerical (red) results. The solid lines represent the orbits with the constant vertical acceleration for the disc while the dashed lines show the results of the linear approximation.

3.2.2 Coronal drag

In this section, we aim to model the drag effect on the fountain orbits described in Section 3.2.1. Fraternali & Binney (2008) pointed out that fountain clouds experience a drag as they move through the hot corona. This interaction slows down the clouds and makes them transfer angular momentum to the corona. In order to include the drag in our pure fountain model, we follow Fraternali & Binney 2008 and Marasco et al. 2012 (Section 2.2.2) and correct the gravitational acceleration by adding the drag contribution. Fraternali & Binney (2008) assumed that the drag acceleration is proportional to the square of the flow velocity of the corona past the cloud as this motion has a high Reynolds number. This choice affects the form of the equation of the motion, which becomes non-linear and does not have an analytical solution. Therefore, we have chosen a simpler form for the drag acceleration and assumed a linear dependence on the actual vertical velocity follows:

$$g_{\mathrm{drag},z} = -\frac{C}{L} < v_z > v_z \tag{3.55}$$

where C and L are defined as in Section 2.2.2 and $< v_z >$ is the mean vertical velocity. As mentioned in Section 2.3.1, the kick velocity is equal to 80 km s^{-1} while that at the maximum z reached during the orbits is null, so the mean vertical velocity is $< v_z > \sim 40$ km s^{-1}(see Figure 2.18, left panels).

In order to build the equation of motion for the two-component model, we can follow the same approach as in Section 3.2.1, so we analise the bi-linear and the constant-linear approximations separately.

Stellar disc linear acceleration

First, we analise the case with the linear vertical accelerations both for the disc and the halo as the solving method is simpler and the its general solution can be used to determine the that in the constant-linear approximation. The Cauchy problem can be written as:

$$\begin{cases} \ddot{z} = -\frac{C}{L} < v_z > \dot{z} - 4\pi G \rho_{\mathrm{tot}}(1+\eta_{\mathrm{tot}})z \\ z(0) = 0 \\ \dot{z}(0) = v_{\mathrm{kick}} \end{cases} \tag{3.56}$$

Let us define $\gamma = \frac{C}{L} < v_z >$ and $\omega_{\mathrm{tot}}^2 = 4\pi G \rho_{\mathrm{tot}}(1+\eta_{\mathrm{tot}})$. Thus, we obtain the equation for the damped harmonic oscillator:

$$\ddot{z} + \gamma \dot{z} + \omega_{\mathrm{tot}}^2 z = 0 \tag{3.57}$$

where ω_{tot} is the angular frequency and γ is related to the damping coefficient. Then, the characteristic polynomial is:

$$\lambda^2 + \gamma\lambda + \omega_{\mathrm{tot}}^2 = 0 \tag{3.58}$$

whose roots are:

$$\lambda_{1,2} = \frac{-\gamma \pm \sqrt{\gamma^2 - 4\omega_{\text{tot}}^2}}{2} \tag{3.59}$$

We can distinguish three cases for the damped oscillator:

1. Overdamped: $\gamma^2 - 4\omega_{\text{tot}}^2 > 0$, which has two different real solutions;
2. Critical damping: $\gamma^2 - 4\omega_{\text{tot}}^2 = 0$, with two identical real solutions;
3. Underdamped: $\gamma^2 - 4\omega_{\text{tot}}^2 < 0$, , two different imaginary solutions.

In order to understand which is our case, we must study the sign of $\gamma^2 - 4\omega_{\text{tot}}^2$ as a function of the radius R.

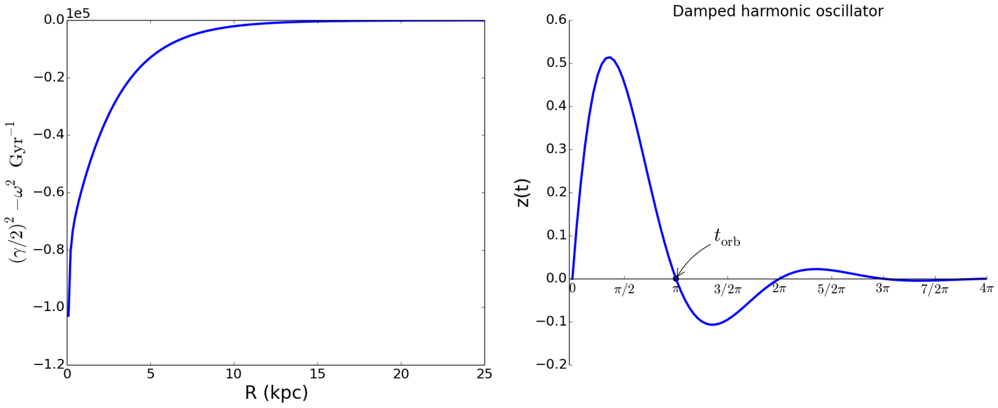

(a) **(b)**

Figure 3.27: *Left*: argument of the roots $\sqrt{(\gamma/2) - \omega_{\text{tot}}^2}$ as a function of radius. *Right*: damped oscillator trajectory as a function of time.

Figure 3.27a shows that argument of the square root in eq. 3.59 is always negative, so both roots are imaginary and equal to:

$$\lambda_{1,2} = \frac{-\gamma \pm i\sqrt{4\omega_{\text{tot}}^2 - \gamma^2}}{2} \tag{3.60}$$

The general solution and its derivative are the same as eqs. 3.37a and 3.37b. We can calculate the constants C_1 and C_2 using the initial conditions:

$$\begin{cases} C_1 = -\frac{v_{\text{kick}}}{i\sqrt{4\omega_{\text{tot}}^2 - \gamma^2}} \\ C_2 = \frac{v_{\text{kick}}}{i\sqrt{4\omega_{\text{tot}}^2 - \gamma^2}} \end{cases} \tag{3.61}$$

Thus, the solution is:

$$z(t) = \frac{v_{\text{kick}}}{i\sqrt{4\omega_{\text{tot}}^2 - \gamma^2}} e^{-\frac{\gamma}{2}t} \left[\exp\left(\frac{i\sqrt{4\omega_{\text{tot}}^2 - \gamma^2}}{2} t \right) - \exp\left(\frac{-i\sqrt{4\omega_{\text{tot}}^2 - \gamma^2}}{2} t \right) \right] \tag{3.62}$$

Through the Euler's formula, eq. 3.62 can be written as:

$$z(t) = \frac{v_{\rm kick}}{\sqrt{\omega_{\rm tot}^2 - (\gamma/2)^2}} e^{-\frac{\gamma}{2}t} \sin\left(\sqrt{\omega_{\rm tot}^2 - (\gamma/2)^2 t}\right) \tag{3.63}$$

So, the amplitudes of the oscillations fall exponentially with time. The position $z(t)$ and the vertical velocity $v_z(t)$ are shown in Figure 3.28a and 3.28b.

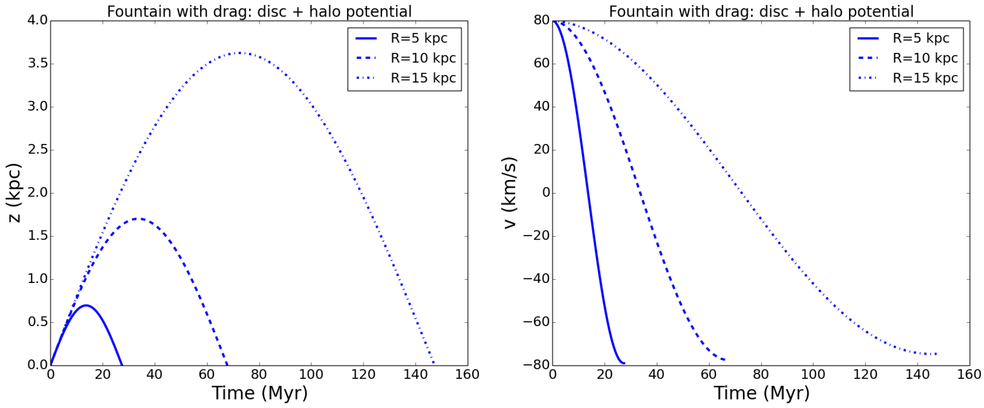

(a) Positions $z(t)$.

(b) Vertical velocities $v_z(t)$.

Figure 3.28: Fountain with drag: orbits (left) and velocities (right) at fixed radii in the two-component potential (see Table 2.2). The vertical acceleration is linear with z for the disc and the halo.

Clearly, $z(t)$ must be null when the particle comes back to the disc (orbital time), so the first zero is:

$$\sqrt{\omega_{\rm tot}^2 - (\gamma/2)^2 t_{\rm orb,drag}} = \pi \tag{3.64}$$

and we can write the orbital time as follows:

$$t_{\rm orb,drag} = \frac{\pi}{\sqrt{\omega_{\rm tot}^2 - (\gamma/2)^2}} = \frac{\pi}{\sqrt{4\pi G\rho_{\rm tot}(R,0)(1+\eta_{\rm tot}(R)) - (C < v_z > /2L)^2}} \tag{3.65}$$

Figure 3.29 shows the difference between the pure fountain orbital times and those with drag: note that they are essentially identical, which means that the drag deceleration is negligible with respect to the gravitational g_z.

We can try to understand if an increase of the drag influence can modify the orbital time in Figure 3.29. To this purpose, we can follow the same approach as in Section 2.3.2 and study three cases with different $t_{\rm drag}$: 270 Myr, 530 Myr and 800 Myr. Figure 3.30 shows a comparison between the three situations. We can conlude that, in our model, the gravity is completely dominant with respect to the effect of drag.

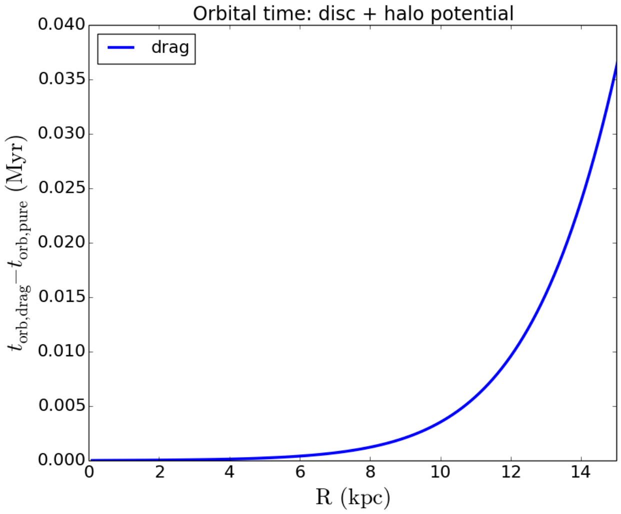

Figure 3.29: Difference between the orbital time for the galactic fountain with drag (blue, eq. 3.65) and that for the pure fountain (red, eq. 3.50) in the presence of the two-component potential.

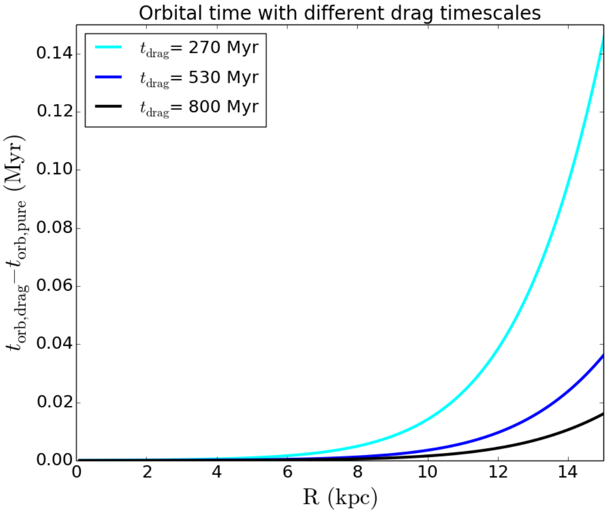

Figure 3.30: Difference between the orbital times for the fountain with drag with different drag timescales (270 Myr (light blue), 530 Myr (blue) and 800 Myr (black)) and that in the pure fountain case, in the two-component potential.

Stellar disc constant acceleration

Let us consider the constant-linear case, the equation of the motion eq. 3.51 becomes:

$$\ddot{z} = -4\pi G \rho_{\rm DM}(R,0)(1+\eta_{\rm DM}(R))z - \frac{C}{L} < v_z > \dot{z} - 2\pi G \Sigma(R) \tag{3.66}$$

This is a non-homogeneous ODE and its solution is given by the sum of the general solution of the homogeneous equation, which is eq. 3.63, and a particular solution of eq. 3.66. We can expect that the form of the particular solution might be similar to that in eq. 3.52, so finding the orbital time could not be as simple as the previous case (Section 3.2.2). Therefore, we put aside the constant-linear approximation for the moment as it is beyond the aim of this thesis.

3.2.3 Coronal condensation

In this section, we provide a simple method to model the condensation of the coronal material. The hot coronal gas is expected to have low angular momentum with respect to the disc, so the mixing of this material with the clouds gas makes them lose angular momentum. First of all, we can try to find an analytical form for the de-acceleration due to the condensation. The conservation of the momentum can be written by equating the initial momentum of a clouds and the total momentum during the interaction with the corona:

$$m(t)\vec{v}(t) = m_0\vec{v}_0 + m_{\text{acc}}(t)\vec{v}_{\text{cor}} \tag{3.67}$$

where $m(t)$ and $\vec{v}(t)$ are the clouds mass and velocity at the time t, m_0 and $\vec{v}_0$ are the same quantities at $t = 0$, and m_{acc} and $\vec{v}_{\text{cor}}$ are the accreted mass of the corona and its rotational velocity. The numerical simulations performed by Marinacci et al. (2011) suggest that the mass of the clouds increases exponentially with time:

$$m(t) = m_0 e^{\alpha t} \tag{3.68}$$

Then, the mass of the condensed coronal material m_{acc} can be written as:

$$m_{\text{acc}}(t) = m(t) - m_0 = m_0\left(e^{\alpha t} - 1\right) \tag{3.69}$$

Substituting eq. 3.69 in eq. 3.67, we find:

$$m_0 e^{\alpha t}\vec{v}(t) = m_0\vec{v}_0 + m_0\left(e^{\alpha t} - 1\right)\vec{v}_{\text{cor}} \tag{3.70}$$

which can be written as:

$$\vec{v}(t) - \vec{v}_{\text{cor}} = (\vec{v}_0 - \vec{v}_{\text{cor}})e^{-\alpha t} \tag{3.71}$$

Note that the l.h.s. of this equation is the relative velocity between the cloud and the corona. Then, the derivative of eq. 3.71 yields the acceleration:

$$\vec{a}(t) = -\alpha(\vec{v}_0 - \vec{v}_{\text{cor}})e^{-\alpha t} \tag{3.72}$$

which can be rewritten using eq. 3.71:

$$\vec{a}(t) = -\alpha(\vec{v}(t) - \vec{v}_{\text{cor}}) \tag{3.73}$$

Let us consider only the z components. The hot corona rotates (tangential velocity) and it has no other motions. Thus, the acceleration due to the accretion can be written as (see also Marasco et al. 2012):

$$\ddot{z} = -\alpha\dot{z} \tag{3.74}$$

At this point, we can study the motion in the two-component potential. As for the drag case, we examine only the bi-linear approximation (eq. 3.30) for the vertical acceleration as the constant-linear g_z (eq. 3.18) is likely to be more complicated to modify with the accretion acceleration.

Therefore, once again, the motion can be described by the Cauchy problem with initial values:

$$\begin{cases} \ddot{z} = -\alpha\dot{z} - 4\pi G\rho_{\text{tot}}(1+\eta_{\text{tot}})z \\ z(0) = 0 \\ \dot{z}(0) = v_{\text{kick}} \end{cases} \tag{3.75}$$

We can define $\omega_{\text{tot}}^2 = 4\pi G\rho_{\text{tot}}(1+\eta_{\text{tot}})$, obtaining the equation which describes the motion of a damped oscillator with angular frequency ω_{tot}:

$$\ddot{z} + \alpha\dot{z} + \omega_{\text{tot}}^2 z = 0 \tag{3.76}$$

Clearly, the solving method is the same as that for the oscillator damped by the drag, so the characteristic polynomial and its roots are the same as eqs. 3.58 and 3.59 with α instead of γ. Then, according to Marasco et al. (2012), we assume $\alpha = 6.3\,\text{Gyr}^{-1}$. So, let us analise the sign of $\alpha^2 - 4\omega_{\text{tot}}^2$ as a function of the radius. As shown in Figure 3.31, this choice makes the argument of the square root always negative.

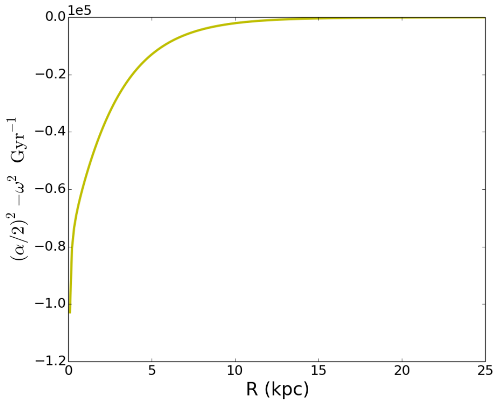

Figure 3.31: Argument of the root $\sqrt{(\alpha/2)^2 - \omega_{\text{tot}}}$ as a function of the radius.

Therefore, both the roots are imaginary and the solution of the Cauchy problem has the same form as eq. 3.63 but with α instead of γ:

$$z(t) = \frac{v_{\text{kick}}}{\sqrt{\omega_{\text{tot}}^2 - (\alpha/2)^2}} e^{-\frac{\alpha}{2}t} \sin\left(\sqrt{\omega_{\text{tot}}^2 - (\alpha/2)^2}t\right) \tag{3.77}$$

The position $z(t)$ and the velocity $v_z(t)$ are shown in Figure 3.32a and 3.32b respectively. The orbital time as a function of the radius can be evaluated by:

$$t_{\text{orb,accr}}(R) = \frac{\pi}{\sqrt{\omega_{\text{tot}}^2 - (\alpha/2)^2}} = \frac{\pi}{\sqrt{4\pi G\rho_{\text{tot}}(R,0)(1+\eta_{\text{tot}}(R)) - (\alpha/2)^2}} \tag{3.78}$$

Figure 3.33 shows the difference between the pure fountain orbital time and that with accretion. Note that this difference is larger than that in the drag case (see Figure 3.29), as the condensation causes a slight increase of the orbital times, but still very small (e.g. ~ 1.6 Myr at 15 kpc).

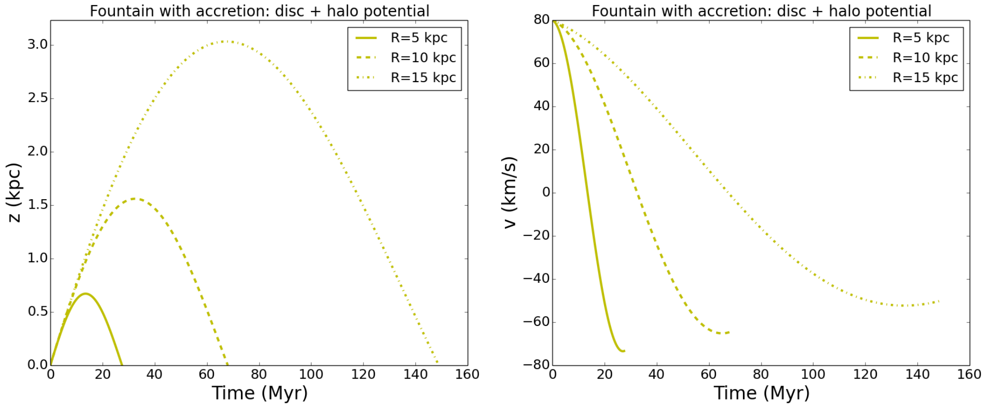

(a) Positions $z(t)$.

(b) Vertical velocities $v_z(t)$.

Figure 3.32: Same as 3.28 but with the accretion instead of the drag.

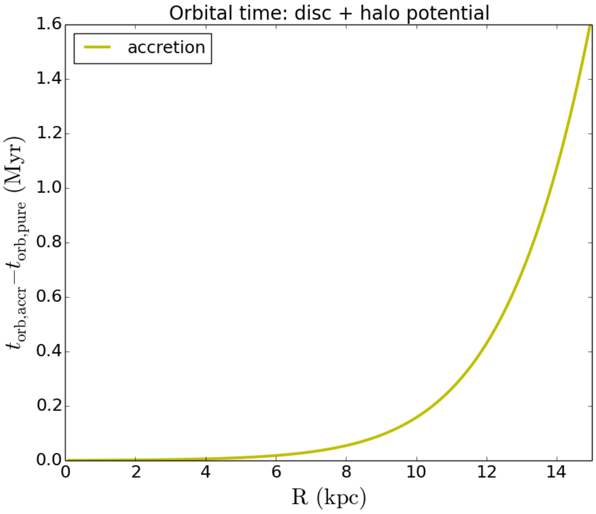

Figure 3.33: Difference between the orbital time for the galactic fountain with the accretion (eq. 3.78) and that for the pure fountain (eq. 3.50) in the presence of the two-component potential.

In a more realistic scenario, fountain clouds experience the effect of both the drag and the accretion as they travel through the hot corona. In our model, the decelerations due to these effects depend on the vertical velocity ($\dot{z}(t)$) and on a constant that is γ for the drag (Section 3.2.2) and α for the accretion. As a result, combining both the interactions is very simple and the form of the solution for the position ($z(t)$) and the orbital time as a function of radius are the same as eqs. 3.77 and 3.78 but with $\gamma + \alpha$ instead of α alone. As we pointed out in Section 3.2.2, the effect of the drag is essentially negligible, so we can expect that the results in the case with drag and accretion would be the same as the situation described in this section.

Chapter 4

Testing the pure fountain orbital times

In this chapter, we test our model for the orbits by comparing the analytical (see Chapter 3) and numerical orbital times (see Chapter 2) in the pure fountain scenario. In Section 4.1, we analise single-component and two-component potentials. In Section 4.2, we present two models of the dark matter halo whose rotation curve is similar to that of the Milky Way, then we calculate their orbital times and compare them to the numerical orbital times for the two-component potential.

4.1 Milky Way components

The pure fountain is the best test case for our analytical model. So, we can check if our equations for the orbital time (see Section 3.2.1) lead to similar results as the numerical code *Extragas* (see Section 2.2). We restrict our study to radii out to 15 kpc as, in the Milky Way disc, most stars form between ∼ 4 kpc and 12-13 kpc (e.g. Case & Bhattacharya 1998). *Extragas* can integrate the orbits of a great number of particles and provide their orbital parameters. Among these, the quantities of interest here are:

1. the orbital time $t_{\rm orb}$ of each particle ejected at radius $R_{\rm kick}$;
2. the landing radius, where each particle returns to the disc, $R_{\rm land}$.

As mentioned in Section 2.3.1, the radial displacement is small in potentials such as the halo and the total one, but it is significant in the case of the disc alone. On the other hand, our analytical model is restricted to the z-direction, so it can not provide the radial displacement and take account of the density variation due to this effect. However, we can define a mean radius $R_{\rm mean}$, which is the average between $R_{\rm kick}$ and $R_{\rm land}$. We compare the analytical and the numerical orbital times at $R_{\rm kick}$ and $R_{\rm mean}$, where the density is approximately the average between those at $R_{\rm kick}$ and $R_{\rm land}$.

In the following sections, we first compare the single-component models in the pure fountain scenario, then we analise the two-component cases.

4.1.1 The stellar disc

In Section 3.2.1, we examined the motion of a particle that experiences a constant or a linear gravitational pull due to the disc potential (see Table 2.2). The first (constant) form of the vertical acceleration yields:

$$t_{\mathrm{orb},\star}(R) = \frac{v_0}{\pi G \Sigma(R)} \tag{4.1}$$

while the second (linear) gives:

$$t_{\mathrm{orb},\star}(R) = \frac{\pi}{\sqrt{4\pi G \rho_\star(R,0)(1+\eta_\star(R))}} \tag{4.2}$$

We can expect that eq. 4.1 will be more suitable to describe the orbits that reach high z because, in this case, the disc can be seen as a razor-thin layer of matter. The linear acceleration (eq. 4.2) is a good approximation of g_z only for those particles that achieve extremely low heights. Figure 4.1 compares the numerical and the analytic orbital times: the green points represent the orbital time as a function of the kick radius, while the blue triangles are the orbital times as a function of the mean radius.

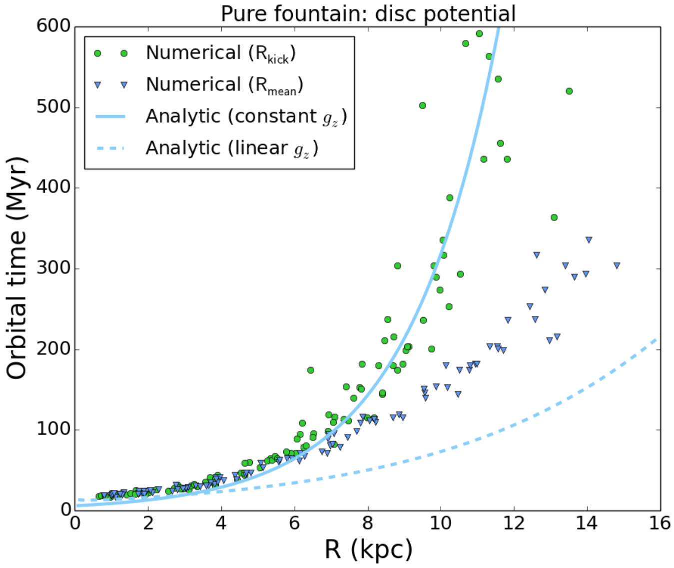

Figure 4.1: Orbital time in the presence of the disc potential: the particles are kicked out of the disc with initial velocity v_{kick}= 80 km s^{-1}. The green points and the blue triangles are the numerical orbital times as a function of R_{kick} and of R_{mean} respectively. The lines represent the analytical orbits assuming the constant (dashed) and a the linear (solid) approximation for g_z (eqs. 4.1 and 4.2).

In the innermost parts ($R \lesssim 3$ kpc) of the Galaxy, the disc vertical acceleration strongly pulls the particles to the equatorial plane. As a consequence, they reach low heights and experience an acceleration that is almost linear with z. In fact, in these regions ($R \lesssim 3$ kpc) eq. 4.2 (linear g_z) approximates the numerical orbital times better than eq. 4.1 (constant g_z). However, we are not very interested in these parts of the disc, which are occupied by the stellar bulge and where star formation is not very high. On the other hand, eq. 4.1 provides a very good estimate of the numerical orbital time (as a function of the kick radius) from about 4 kpc to the outer parts of the disc. Note however that it overestimates the orbital time if R_{mean} is used.

In conclusion, the constant acceleration provides a better evaluation of the orbital time as the particles reach significant heights in the regions of interest.

We can try to set a lower initial velocity for the particles to test whether the linear g_z supplies a good evaluation of the orbital time in this case. In this way, the particles reach low heights everywhere and we can expect that the linear acceleration and eq. 4.2 should be relatively good approximations. Figure 4.2 shows the orbits obtained with kick velocity equal to 30 km s^{-1}. Note the clear improvement of the linear approximation: eq. 4.2 (linear, dashed line) resebles the numerical results up to 5 kpc while, in the other parts, it leads to an underestimate of the orbital time.

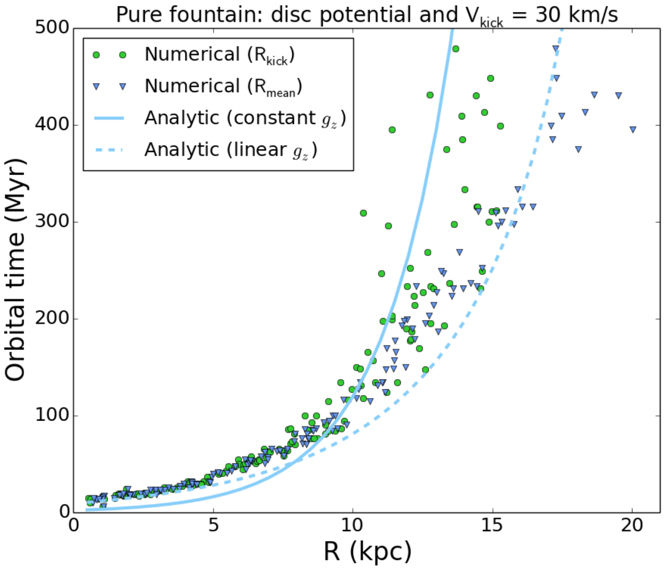

Figure 4.2: Same as Figure 4.1, but with v_{kick}= 30 km s^{-1}.

4.1.2 The dark matter halo

We have shown that the motion of particles in a dark matter only potential is essentially an harmonic oscillator. In addition, the radial displacements at the end of the orbits can be considered to be negligible and the vertical acceleration grows almost linearly with z (see Section 2.1.2). Therefore, we can expect that the numerical orbital time is well approximated by (see Section 3.1.2):

$$t_{\mathrm{orb,DM}}(R) = \frac{\pi}{\sqrt{4\pi G \rho_{\mathrm{DM}}(R,0)(1+\eta_{\mathrm{DM}}(R))}} \tag{4.3}$$

Figure 4.3 shows the orbital time as a function of R_{kick} and R_{mean}. The analytical trend resembles the overall numerical one, although the latter is slightly lower than the former.

The main reason for this underestimate is that we calculate the density in the midplane, where the cylindrical radius R is equal to the spherical one r, and then we assume it to be constant with z. However, the halo profile (3.19) depends on r, which becomes greater than R as the heigh above the disc grows because $r = \sqrt{R^2 + z^2}$. As a consequence, we slightly overestimate the density and the vertical acceleration above the disc, decreasing the analytical orbital time. Note that using R_{mean}, as expected, slightly improves the match.

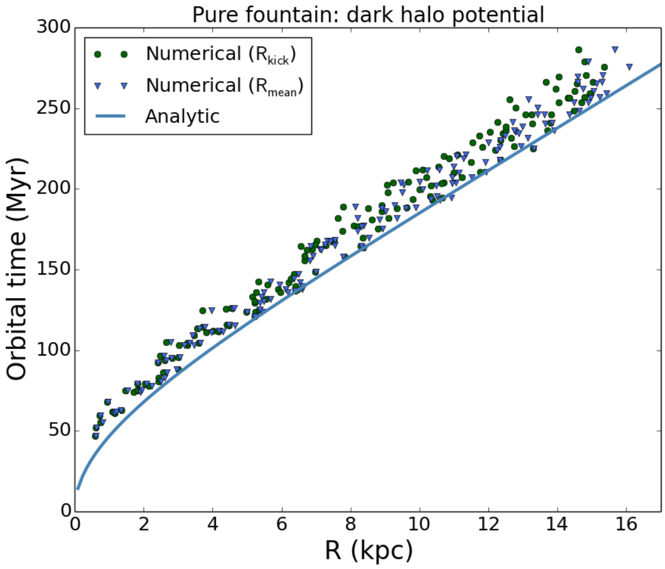

Figure 4.3: Orbital time in the dark matter halo (NFW) potential: the particles are kicked vertically with initial velocity v_{kick}= 80 km s^{-1}. The green points and the blue triangles are the numerical orbital times as a function of R_{kick} and of R_{mean} respectively. The solid line represents the analytic orbital time calculated with eq. 4.3.

As for the disc, we can check what is the origin of the underestimate of the orbital time by setting a lower inital velocity for the particles. Figure 4.4 shows the orbital times as a function of the radius for particles kicked with $v_{\mathrm{kick}} = 30\mathrm{km\ s}^{-1}$.

With this choice, we decrease the heights reached by the particles, so the spherical and cylindrical radii are almost equal to each other and the analytical orbital time perfectly reproduces the numerical results.

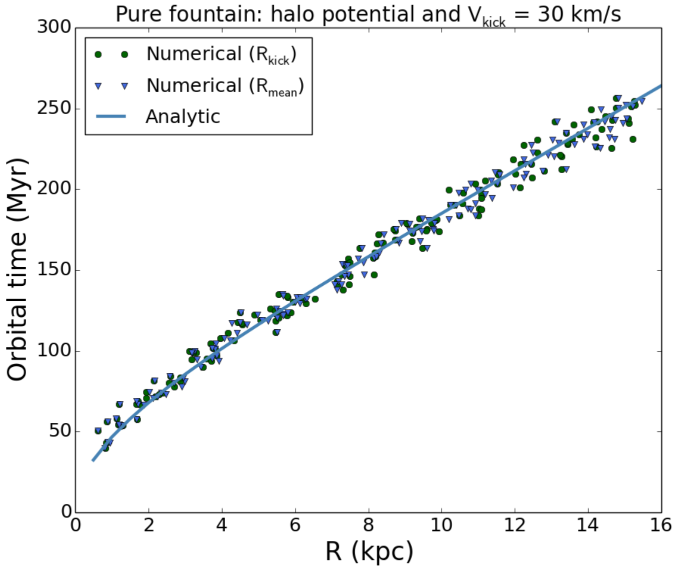

Figure 4.4: Same as Figure 4.3 except that $v_{\rm kick}$= 30 km s^{-1}.

4.1.3 Two-component potential

In Sections 4.1.1 and 4.1.2, we have shown that the constant and the linear accelerations are more suitable to describe the disc and the halo vertical accelerations respectively. Therefore, we can expect that their combination will reproduce the numerical results in the whole potential of the Milky Way (see Table 2.2).

Figure 4.5 shows that, at small radii, the disc strongly affects the orbital time, thus the constant acceleration for the disc component is a good approximation between 4 kpc and 7 kpc. Then, in the outer parts (from 10 kpc to 15 kpc), the halo orbital time follows the trend of the numerical points. In Section 3.2.1, we studied two approaches to model the pure galactic fountain in the two-component potential: the first assumes that the vertical accelerations of the disc and the halo grows linearly with z while the second approximates the disc g_z as constant with z. Then, we obtained two different functional forms for the orbital time of the pure fountain. For completeness, we show both solutions and we compare them to the numerical orbital time provided by *Extragas*.

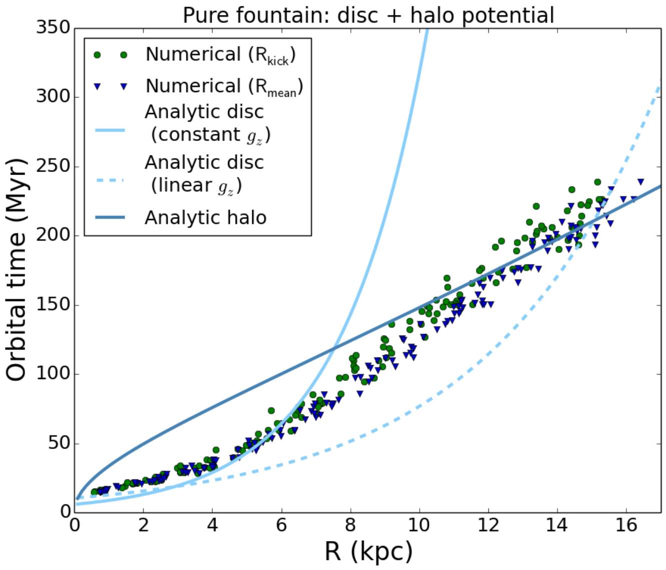

Figure 4.5: Comparison of the single-component analytical and the two-component numerical orbital times. The green points and the blue triangles are the numerical orbital times as a function of $R_{\rm kick}$ and of $R_{\rm mean}$ respectively. The light blue lines represents the analytic orbital times for the disc as calculated with the constant (solid, eq. 4.1) or the linear (dashed, eq. 4.2) g_z. The blue solid line is the orbital time for the dark matter halo (eq. 4.3).

Linear vertical acceleration

Let us first consider the case in which both accelerations are linear with z. In Section 3.2.1, we found that the orbital time is give by:

$$t_{\rm orb,tot}(R) = \frac{\pi}{\sqrt{4\pi G\rho_{\rm tot}(R,0)(1+\eta_{\rm tot}(R))}} \tag{4.4}$$

where $\rho_{\rm tot}$ and $\eta_{\rm tot}$ are the total density profile and rotational density contribution (see Section 3.1.3).

Figure 4.6 compares the theoretical and numerical results in the presence of the two-component potential. The green and the blue points are the numerical orbital times as a function of $R_{\rm kick}$ and $R_{\rm mean}$. The solid line is provided by eq. 4.4. The assumed gravitational pull of the disc is so strong in this case (see Figure 3.13a) that the analytical orbital time is reduced by a factor about 2 in the outer parts, where the dark matter halo should be dominant.

In conclusion, the bi-linear model fails to reproduces the *Extragas* data both in the inner and in the outer regions. With this formulation, the disc component influences the analytical orbital time also in the the those regions of the Galaxy where the dark matter halo should be dominant.

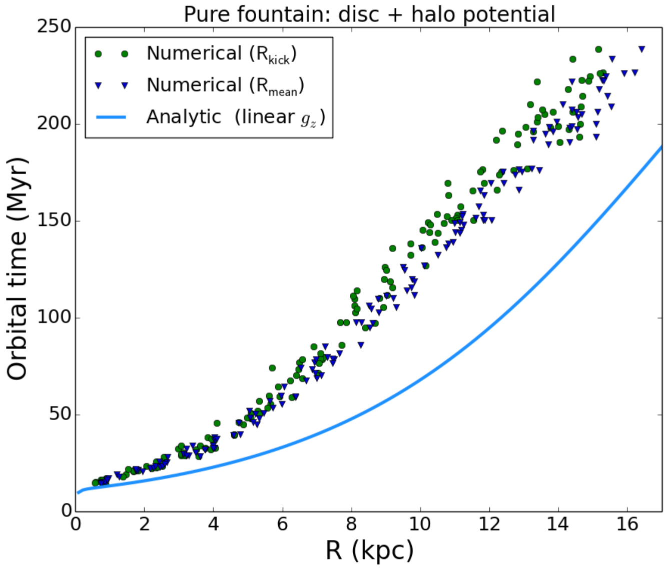

Figure 4.6: Same as 4.3 except that the particles travel in the two-component potential. The solid line represents the orbital time as calculated using eq. 4.4.

Constant vertical acceleration

In Section 3.2.1, we assumed a constant vertical acceleration for the disc and a linear g_z for the halo. The solution of the equation of motion under the influence of these forces (eq. 3.31) provides the following analytic form for the orbital time:

$$t_{\mathrm{orb,tot}}(R) = \left(\frac{2}{\omega_{\mathrm{DM}}}\right) \arctan\left(\frac{2\rho_{\mathrm{DM}}(R,0)v_{\mathrm{kick}}}{\Sigma(R)\omega_{\mathrm{DM}}}\right) \tag{4.5}$$

where the angular frequency is $\omega_{\mathrm{DM}} = \sqrt{4\pi G\rho_{\mathrm{DM}}(R,0)(1+\eta_{\mathrm{DM}}(R))}$ and $\Sigma(R)$ is the surface density profile of the razor-thin disc described in Section 3.1.1.

Figure 4.7 compares the theoretical and numerical results obtained with the two-component potential. The green and the blue points are the numerical orbital times as a function of R_{kick} and R_{mean} while the solid line is provided by eq. 4.5.

Eq. 4.5 successfully reproduces the trend of the numerical orbital time in the two-component potential. Note that the choice of assuming a razor-thin disc has properly reduced its influence on those parts of the Galaxy where the halo potential is dominant. The theoretical prediction is slightly higher than the numerical results as our approach includes only the dark matter halo rotational density. Within $R \sim 4$ kpc, there is an excellent match between the numerical and the analytic orbital times. Beyond 4 kpc, our model overestimates the *Extragas* data of $\gtrsim 10$ % but our analytic prediction is still satisfactory.

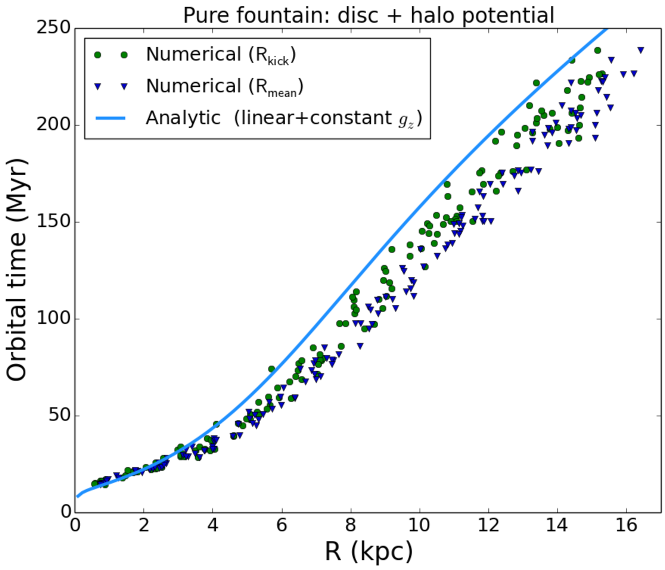

Figure 4.7: Same as 4.3 except that the particles travel in the two-component potential. The solid line represents the orbital time as calculated using eq. 4.5.

Moving towards the inclusion of interactions

As mentioned in Section 3.2.2, including the interaction between the cold clouds and the hot galactic corona in our constant-linear model might not be simple and an analytic solution may not exist. Therefore, we have built three models for the fountain with the drag and the condensation (see Sections 3.2.2 and 3.2.3) using the bi-linear model for the vertical acceleration. Unfortunately, the bi-linear model for the gravitational pull is not suitable to reproduce the pure fountain orbital times. However, Figure 4.5 suggests that some combination of the disc solution in the inner parts with the halo solution in the outer regions may return acceptable orbital times. We can try to combine eqs. 4.1, 4.2 and 4.3 in order to reproduce the numerical trend of the orbital times in the presence of the whole Galactic potential. Then, we could incorporate the models with drag and accretion into this combination of the single-component orbital times. As a first attempt, we can calculate an average between the disc and the halo orbital times weighting them on their density:

$$< t_{\rm orb} >= \frac{t_{{\rm orb},\star}\rho_\star + t_{\rm orb,DM}\rho_{\rm DM}}{\rho_\star + \rho_{\rm DM}} \tag{4.6}$$

In Section 3.2.1, we analised two possible forms for the disc orbital time, so we follow two approaches and calculate the mean using eq. 4.2 (linear g_z) or eq. 4.1 (constant g_z). Figure 4.8 [1] shows the results in these two cases: in particular, the orange line is given by eq. 4.6 using the constant approximation for the disc while the yellow line is obtained by assuming the linear g_z. Unfortunately, none of them reproduces the numerical trend. Concerning the orange line, it

---

[1] In this section, we omit to plot the numerical orbital times as a function of $R_{\rm mean}$ as they do not differ considerably from the others.

seems that the disc orbital time is too high in the outer parts, so its influence on the weighted mean is too strong at large raddi. Then, the yellow line remains below the *Extragas* data from 4 kpc to 14 kpc as the disc orbital time is much lower than that of the halo, so the weighting on the density is not enough to 'switch off' the disc contribution in the outer regions.

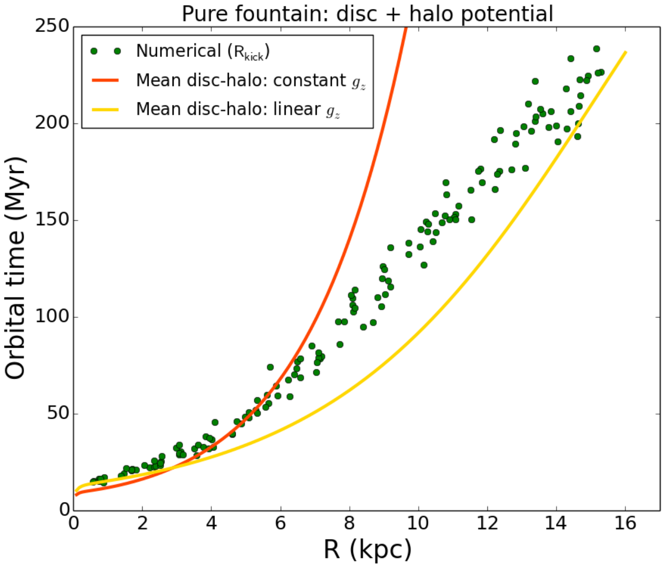

Figure 4.8: Comparison of the numerical orbital time (green points) for the two-component potential and the weighted averages for the analytical model (eq. 4.6). The orange line is calculated with the constant g_z for the disc and the yellow line is given by the linear g_z for both the components.

In the light of these findings, we might find an alternative way to fade the disc contribution at large radii. To this purpose, we can try to build a function which erases the disc contribution starting from a certain transition radius R_t, where the dark matter component begins to dominate over the stellar one. In this way, we can prevent the disc vertical acceleration to outweight the halo in the outer parts of the Galaxy. To avoid introducing another free parameter, we can try to set the transition radius in one of the two following ways:

- the radius where the disc orbital time intersects the halo one, R_cross (see Figure 4.5), so, in this case, $R_\mathrm{t} \approx 7.5$ kpc;
- the half-mass radius of the disc (R_half), which includes the half of the total disc mass. The half-mass radius is about 1.67 times the disc scaleleght $R_\star$, so $R_\mathrm{t} \simeq 1.67 \times R_\star \approx 4.2$ kpc for our model of the disc (see Table 2.2).

Then, we can find a proper function to 'switch off' the disc contribution starting from the transition radius. A convenient choice is an hyperbolic tangent and this function can be written as:

$$\psi(R) = \frac{1}{2}\left[1 + \tanh\left(R_\mathrm{t} - R\right)\right] \tag{4.7}$$

Thus, $\psi(R)$ is equal to ~ 1 at $R = 0$ and starts decreasing 2 kpc before R_{t}, where it reaches $1/2$. Then, its value declines again and becomes null 2 kpc beyond R_{t}. This is quite a sharp transition because ψ declines from 1 to 0 within 4 kpc (Figure 4.9). Therefore, it may be necessary to introduce a softening parameter h_{soft} in order to smooth this gap:

$$\psi(R) = \frac{1}{2}\left(1 + \tanh\left(h_{\mathrm{soft}}(R_{\mathrm{t}} - R)\right)\right) \tag{4.8}$$

Figure 4.9 shows $\psi(R)$ with R_{t} equal to zero, R_{cross} and R_{half}, and with or without the softening parameter ($h_{\mathrm{soft}} = 0.3$). We can use this connecting function to modify either the density profiles, which influence t_{orb}, or directly on the orbital times.

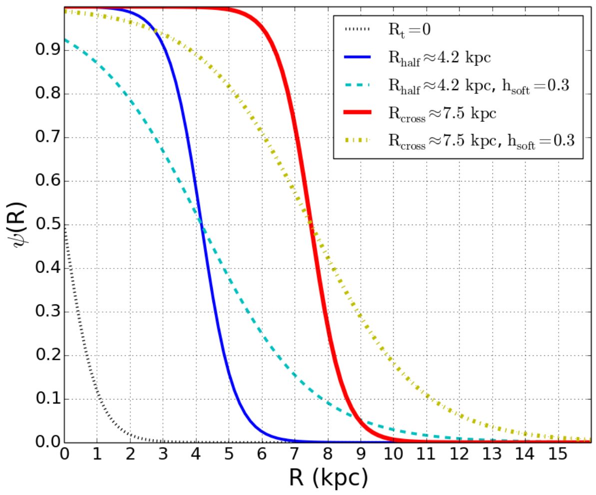

Figure 4.9: Functions to combine the disc and the halo components: eqs. 4.7 and 4.8 with $h_{\mathrm{soft}} = 0.3$ and different transition radii.

First, we start by rewriting the total density ($\rho_{\mathrm{tot}} = \rho_{\star} + \rho_{\mathrm{DM}}$) in eq. 4.4 in the following way:

$$\rho_{\mathrm{tot}}(R) = \rho_{\star}(R)\psi(R) + \rho_{\mathrm{DM}}(R) \tag{4.9}$$

As a result, the disc is made almost negligible in the outer parts, while the halo density is not affected by ψ.

Figure 4.10a shows the orbital time calculated by eqs. 4.4 and 4.9 with $R_{\mathrm{t}} = R_{\mathrm{cross}}$. As expected, the transition is quite sharp (blue line), so we have to include the softening parameter (purple line), which is assumed to be $h_{\mathrm{soft}} = 0.3$. Unfortunately, this choice does not provide a satisfactory improvement as the analytic function underestimates the numerical orbital times. Alternatively, we can choose $R_{\mathrm{t}} = R_{\mathrm{half}}$: we can see in Figure 4.10b that the transition is too sharp (cyan line) but, in this case, the introduction of the softening parameter ($h_{\mathrm{soft}} = 0.3$) clearly improves the analytical estimate (lilac line) of the numerical orbital times. However, the value of h_{soft} is likely to be different from galaxy to galaxy, while our aim is to build an analytical model for the orbital time that could be applied to any galactic potential. Then, we can make a further attempt to combine different solutions for the orbital time.

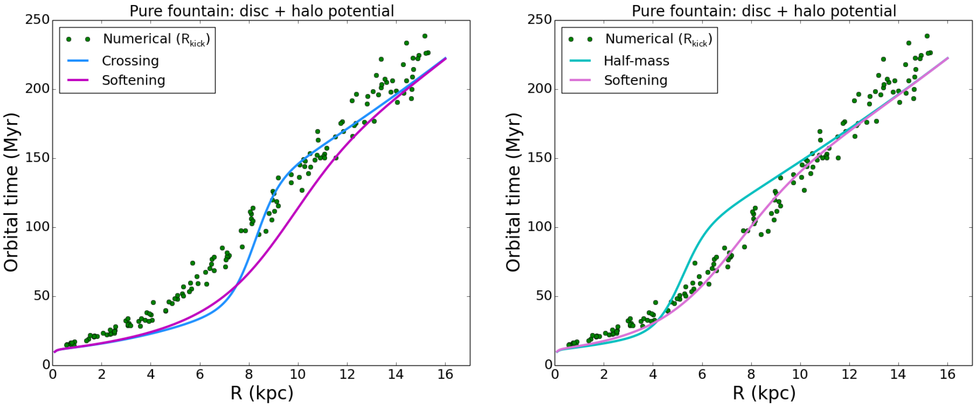

(a) **(b)**

Figure 4.10: Comparison of the numerical orbital time (green points) for the two-component potential and the analytic formula 4.4 with the modified density profile (eq. 4.9). *Left*: eq. 4.7 with $R_{\rm t} = R_{\rm cross}$ (purple line) and eq. 4.8 with $h_{\rm soft} = 0.3$ (blue line). *Right*: eq. 4.7 with $R_{\rm t} = R_{\rm half}$ (lilac line) and eq. 4.8 with $h_{\rm soft} = 0.3$ (cyan line).

Another possible approach is combining the disc and the halo (eq. 4.3) orbital times. We can use the connection function as follows:

$$t_{\rm orb}(R) = t_{{\rm orb},\star}(R)\psi(R) + t_{\rm orb,DM}(R)(1 - \psi(R)) \tag{4.10}$$

In Section 3.2.1, we found two forms for the disc orbital time, so we can examine the two cases separately.

Let us first consider the case with a linear g_z approximation for the disc: eq. 4.10 is built using eq. 4.3 for the halo and eq. 4.2 for the disc, meaning that we are sticking together the orbital times calculated assuming the linear gravitational pulls for both the components. Figures 4.11a and 4.11b show the results of this new combination of the orbital times: the green points are the numerical data, the orange line in the left panel is obtained assuming $R_{\rm t} = R_{\rm cross}$ while we choose $R_{\rm t} = R_{\rm half}$ in the right panel (orange line). Note that, once again, the transition is too sharp to reproduce the numerical trend, therefore we have to introduce the softening parameter $h_{\rm soft} = 0.3$ (purple lines). The result is very safisfactory (Figure 4.11a) but we can not be sure that exporting thise prescriptions to other galaxies (and potentials). Moreover, the choice of $h_{\rm soft}$ remains arbitrary.

As a second attempt, we can try to combine the disc orbital time obtained with the constant approximation (eq. 4.1) and the halo orbital time (eq. 4.3). In Figure 4.12a, we can see that, if we choose $R_{\rm cross}$ as transition radius, the numerical trend is reproduced by the theoretical prediction (Figure 4.12a) and the softening parameter does not provide any improvement. On the other hand, if we choose $R_{\rm half}$ (Figure 4.12b), $h_{\rm soft}$ is needed because the transition is too sharp but the orbital time is overestimated.

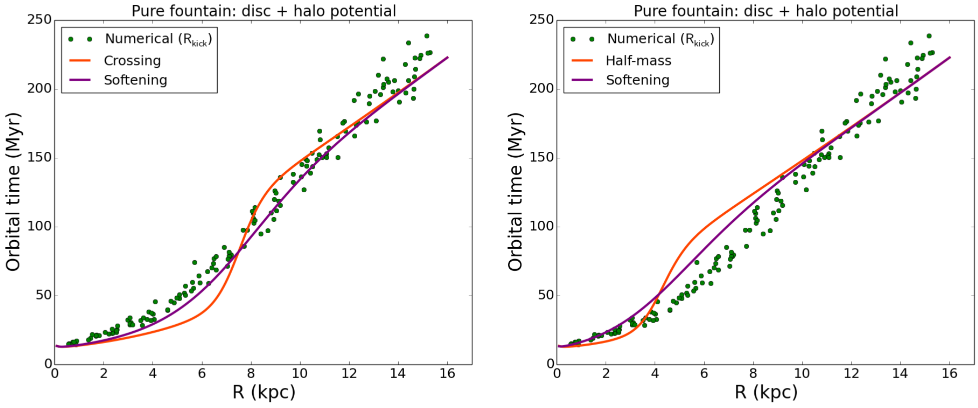

(a) **(b)**

Figure 4.11: Comparison of the numerical orbital time (green points) for the two-component potential and the analytic formula 4.10 assuming the linear g_z for both the disc and the halo. *Left*: eq. 4.7 with $R_t = R_{\rm cross}$ (orange line) and eq. 4.8 with $h_{\rm soft} = 0.3$ (purple line). *Right*: eq. 4.7 with $R_t = R_{\rm half}$ (orange line) and eq. 4.8 with $h_{\rm soft} = 0.3$ (purple line).

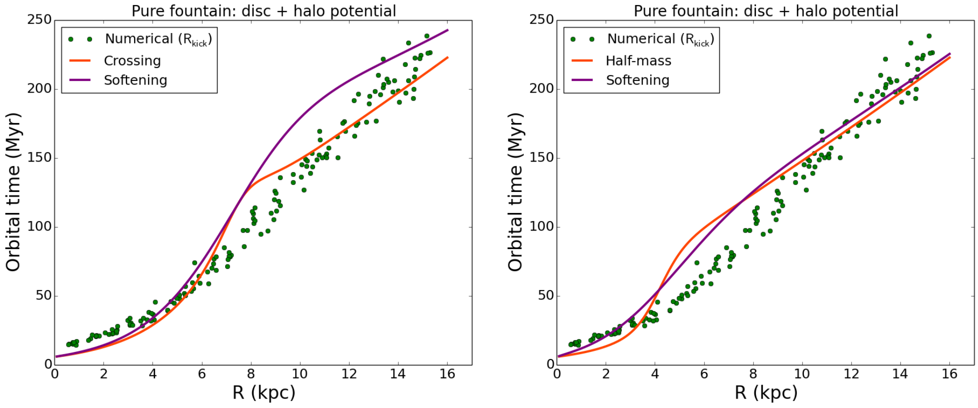

(a) **(b)**

Figure 4.12: Same as Figure 4.11 but the disc orbital time is calculated using eq. 4.1 (costant g_z).

All in all, the best result among those without $h_{\rm soft}$ is achieved by linking the halo (eq. 4.3) and the disc orbital time obtained with the constant approximation (eq. 4.1), although the analytic prediction slight overestimates the numerical results from 7 kpc to 9 kpc (Figure 4.12a).

On the other hand, if we consider the model with $h_{\rm soft} = 0.3$, the best results are shown in Figures 4.10b and 4.11a, where the transition radii are $R_{\rm cross}$ and $R_{\rm half}$ respectively. Unfortunately, the models with the softening parameters are built *ad hoc* for the Mikly Way and we are not sure that these methods can be exported to other galaxies.

4.2 Single-component models with flat rotation curve

In this section, we use an alternative approach and build two models of dark matter haloes which can alone reproduce the Milky Way rotation curve. In practice, we are fully neglecting the presence of the stellar disc. Then, we can calculate the orbital times through eq. 4.3, so the vertical acceleration is assumed to be linearly dependent on z. Lastly, we compare the analytical orbital times for these haloes and those for the Milky Way potential obtained by *Extragas*. Note that, in the following two cases, the vertical acceleration dependes linearly on z, so the introduction of the coronal interactions should be as simple as in the three models described in see Sections 3.2.2 and 3.2.3.

4.2.1 Logarithmic potential

The simplest way to obtain a flat rotation curve is to assume a logarithmic potential (eq. 2.71a in Binney & Tremaine 2008), whose circular velocity is constant at large radii and it is given by:

$$v_{\mathrm{c,log}}(R) = \frac{v_0 R}{\sqrt{R_c^2 + R^2}} \tag{4.11}$$

where v_0 is the asymptotic rotational velocity and R_c is the core radius. For semplicity, we can choose $R_c = 0$ in order to have a totally flat rotation curve, obtaining $v_{\mathrm{c,log}}(R) = v_0$, which is equal to 220 km s^{-1} in the case of the Milky Way. Then, we can evaluate eq. 2.71c in Binney & Tremaine 2008 for $z = 0$ and $R_c = 0$, obtaining the following density profile:

$$\rho_{\mathrm{log}}(R, 0) = \frac{v_0^2}{4\pi G} \frac{1}{R^2} \tag{4.12}$$

and the rotational density is null everywhere (eq. 3.6). Thus, the motion of the particles in the logarithmic potential is an harmonic oscillator and the orbital time can be calculated through eq. 4.3, which yields:

$$t_{\mathrm{orb,log}}(R) = \frac{\pi R}{v_0} \tag{4.13}$$

In this particular case, the orbital time grows linearly with the radius and it can be written as:

$$t_{\mathrm{orb,log}}(R) = 14.3 \left(\frac{v_0}{220\,\mathrm{km\ s^{-1}}} \right)^{-1} \left(\frac{R}{\mathrm{kpc}} \right) \ \mathrm{Myr} \tag{4.14}$$

Figure 4.13 shows the comparison between the numerical results for the two-component potential and eq. 4.14: note that, as the cases discussed in Section 4.1.3, the orbital time is overestimated of $\lesssim 25$ % out to about 8-9 kpc. However, this method is more general and simpler than those described in the previous section.

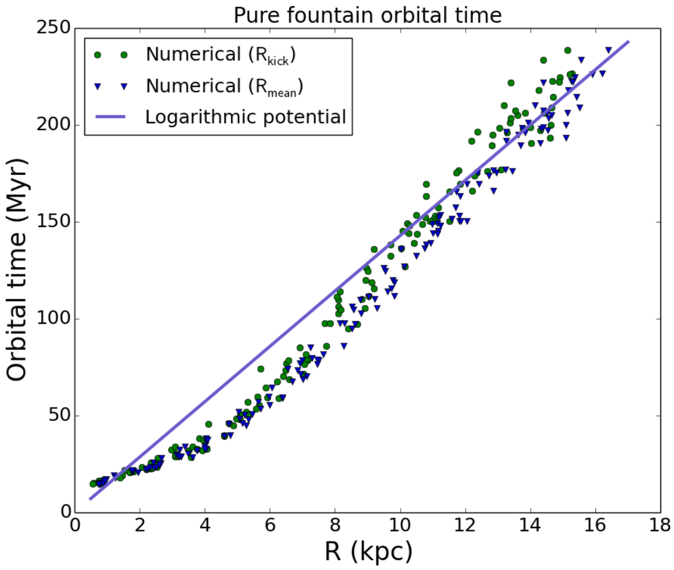

Figure 4.13: Comparison of the numerical orbital time (green points) for the two-component potential and eq. 4.14 (blue line) for the logarithmic potential with v_0 =220 km s^{-1} and R_c=0.

4.2.2 NFW model

A Milky Way-like rotation curve can also be obtained using a NFW density profile alone (eq. 3.19) with proper parameters. For example, we can choose the scale radius $R_s = 4$ kpc and the concentration parameter $c = 43.7$ and calculate the circular velocity using 3.21 (see Section 3.1.2). Figure 4.14 shows the rotational curve, which is not completely flat over the whole galaxy, so the rotational density should be included in this case. However, note that the circular velocity is approximately 220 km s^{-1} from 5 kpc to 15 kpc, which is our range of interest.

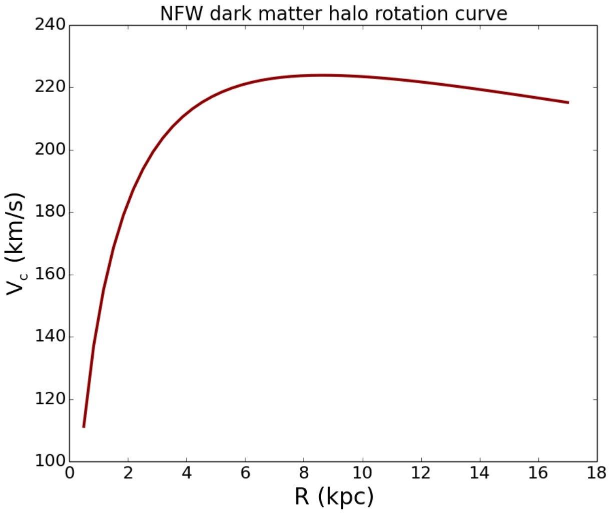

Figure 4.14: NFW halo rotation curve with $R_s = 4$ kpc and $c = 43.7$.

Once again, the motion of the particles is described by an harmonic oscillator, so the orbital time can be easily calculated through eq. 4.3. Figure 4.15 provides the orbital time with (purple) and without (orange) the rotational density: note that the orbital time is still overestimated out to 8-9 kpc and that the rotational density worsens this effect in the inner regions, while the results are positively affected in the outer parts.

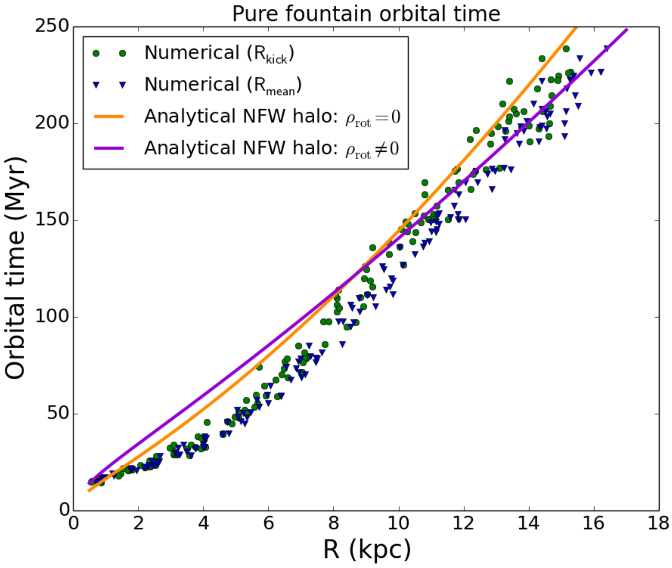

Figure 4.15: Comparison of the numerical orbital time (green points) for the two-component potential and the analytic estimate with (purple) and without rotational density (orange) for the NFW halo with $R_s = 4$ kpc and $c = 43.7$.

Conclusions on the single-component models

Remarkably, the orbital times for these single-component models can reproduce the numerical results quite well. We can see in Figure 4.13 that eq. 4.14 for the isothermal halo can reproduce the *Extragas* data from 9 kpc and beyond, although the orbital times are overestimated for $R \lesssim 8 - 9$ kpc. However, eq. 4.14 might be an useful and practical formula to calculate a rough estimate of the orbital time for any galaxy with a nearly flat rotation curve. Then, the NFW halo model provides an alternative way to calculate the orbital time and the overestimate is slighter than the previous case (Figure 4.15), although the determination of the halo parameters, R_s and c, is less simple. However, both these methods can be exported to other galaxies and they provide better estimate of the orbital time than the models with the connection function. In addition, it is possible to introduce the effect of the interactions with the hot galactic corona in a very simple way, which is described in Sections 3.2.2 and 3.2.3.

Chapter 5

Conclusions

In this chapter, we draw the conclusions of our work and we briefly summarise the content of this thesis.

1. We built a numerical model for the Milky Way potential using the software *Galforces* (Section 2.1), developed by Fraternali & Binney (2006). For semplicity, we chose a two-component model that consists in a stellar disc with a double-exponential profile (Section 2.1.1) and a dark matter halo with a NFW profile and spherical shape (Section 2.1.2). Our model provides a rotation curve similar to that observed for the Milky Way, remaing almost flat at 220 km s^{-1} out to 25 kpc (see Figure 2.7b).

2. We integrated galactic fountain orbits in the Milky Way potential using the software *Extragas* (Section 2.2) developed by Fraternali & Binney (2008) and Marasco et al. (2012). We studied the pure fountain case, which does not involve any interaction with the hot corona, and we analised the shape of orbits of clouds kicked vertically from the plane until they fall back to the disc. We found that the radial displacement at the end of each orbit and the maximum heights reached by the clouds vary with radius because of the variation of the gravitational pull.

3. We introduced the effects of drag (Sections 2.2.2) and accretion (Section 2.2.3) due to the interaction between fountain clouds and the hot galactic halo (corona). We found that the loss of the angular momentum of the clouds causes a clear change in the shape of the orbits: the clouds reach lower heights than in the pure fountain case and there is a significant inward radial displacement.

4. We built an analytic model that describes the vertical acceleration (g_z) of the stellar disc (Section 3.1.1), of the dark matter halo (Section 3.1.2) and of the combined two-component model (Section 3.1.3). We used the results of the code *Galforces* to test if our models resemble the numerical vertical profile of g_z. Concerning the disc, we found that a constant vertical acceleration is suitable to describe the numerical trend of g_z at large

radii (see Figure 3.5). On the other hand, our model for the dark matter halo vertical acceleration can reproduce the *Galforces* results quite well up to heights of a few kpc (see Figure 3.9). Finally, we found that the combination of the constant approximation for the stellar disc and the linear approximation for the dark matter halo successfully represent g_z for the two-component model (see Figure 3.13b).

5. In Chapter 4, we compared the orbital times provided by our analytic model for the pure fountain with those calculated by *Extragas*. In the disc case, the orbital time obtained assuming the constant g_z can reproduce the numerical data beyond 4 kpc (see Figure 4.1). The analytic orbital time for the halo resembles quite well the numerical trend (see Figure 4.3), although there is a systematic underestimate (~ 10 %). Concerning the two-component model, assuming a constant g_z for the disc and a linear g_z for the halo provides a very good estimate of the numerical orbital time (see Figure 4.7), although there is only a slight residual overestimate ($\gtrsim 10$ %).

6. In Section 4.2, we built two models of dark matter haloes that produce a rotation curve similar to that of the Milky Way. Then, we assume a linear g_z to calculate analytically the orbital times and we compare our results to the *Extragas* data: the theoretical predictions of the orbital time can reproduce the numerical trend in the outer parts of the disc but there is an underestimate ($\lesssim 20$ %) in the inner 8 kpc. These models are very simple and can be applied to any galaxy. Their main advantage is that, once known the rotation curve of the galaxy, it is possible to calculate an acceptable estimate of the orbital time.

We can conclude that our analytic models for the pure galactic fountain provide an acceptable estimate of the orbital time, given a simple gravitational potential. These functional forms for the orbital time can be very useful to estimate the gas accretion rate due to the galactic fountain mechanism as a function of the radius. This quantity is quite desirable for the development of evolutionary models of galactic discs: once known the gas accretion rate, it would be possible to study the star formation rate as a function of the disc radius and its evolution across cosmic time. A further development of our work consists in studying in depth how to include the effect of the drag and the accretion in our analytical model of the galactic fountain.

Appendix A

Fountain orbits up to 1 Gyr

In Section 2.3, we provided the numerical fountain orbits until the particles cross the midplane for the first time. However, the behaviour of the orbits over a longer time is very interesting in order to understand how to build the analytical model of the fountain. In this section, we report the orbits calculated up to 1 Gyr, so the particles cross the midplane many times. In particular, for each scenario (pure fountain, drag, accretion and both the interactions), we will see the trajectories of two particles that are kicked from 5 kpc and 10 kpc with initial vertical velocity $v_{\rm kick} = 80$ km s^{-1} and then travel in the two-component potential (Table 2.2).

Pure fountain

Figure A.1a shows the orbits in the pure fountain case. Note that the orbits have a sinusoidal shape: the amplitude at 5 kpc is smaller than that at 10 kpc and its period of oscillations is shorter, so the first orbit crosses the midplane more times than the second. However, both the amplitudes of the orbits remain constant with time. According to the epicycle theory (see Binney & Tremaine 2008), we can say that the vertical period depends on the potential. In fact, the increase of $z_{\rm max}$ with radius is due to the weakening of the vertical gravitational acceleration. In Figure A.1b, we can see that also the vertical velocity has a sinusoidal shape and, once again, the period of oscillation of the orbit at 5 kpc is shorter than that at 10 kpc.

Coronal drag

Figures A.2a and A.2b show the orbits and the vertical velocity of particles travelling under the influence of the coronal drag. The clouds and the corona are defined as reported in Table 2.3. As the pure fountain case, the amplitude of the orbit at 5 kpc is greater than that at 10 kpc. On the other hand, the amplitudes are no more constant with time but there is a clear damping of the sinusoidal oscillations due to the drag deceleration.

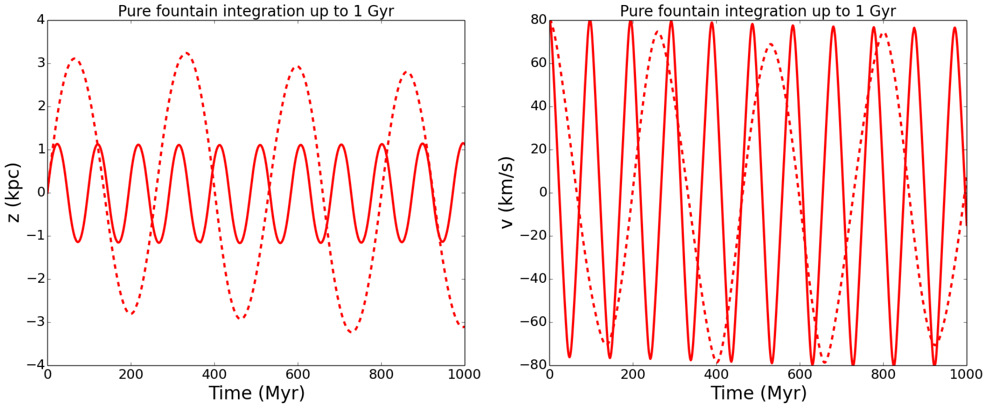

(a) Orbits $z(t)$ **(b)** Vertical velocity $v_z(t)$.

Figure A.1: Pure fountain orbits and vertical velocities as a function of time in the presence of the two-component potential (see Table 2.2). The kick velocity is $v_{\rm kick}$ = 80 km s^{-1} and the kick radii are $R_{\rm kick}$ =5 kpc (solid line) and 10 kpc (dashed line).

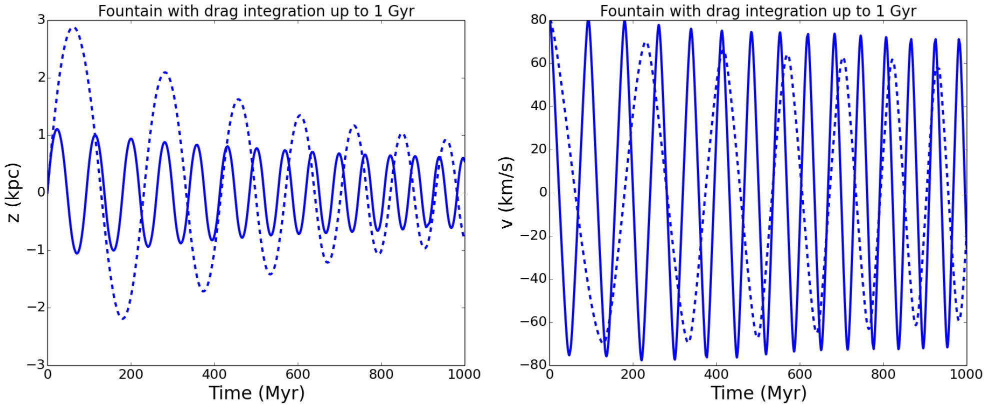

(a) Orbits $z(t)$. **(b)** Vertical velocity $v_z(t)$.

Figure A.2: Fountain orbits and vertical velocities as a function of time in the presence of the drag effect and of the two-component potential (see Table 2.2). The kick velocity is $v_{\rm kick}$ = 80 km s^{-1} and the kick radii are $R_{\rm kick}$ =5 kpc (solid line) and 10 kpc (dashed line).

Coronal condensation

As in the previous case, the condensation of coronal material entails a damping of the oscillations, for both the orbits (Figure A.3a) and the vertical velocities (Figure A.3b). In this case, the damping is more evident and the amplitudes fall more quickly.

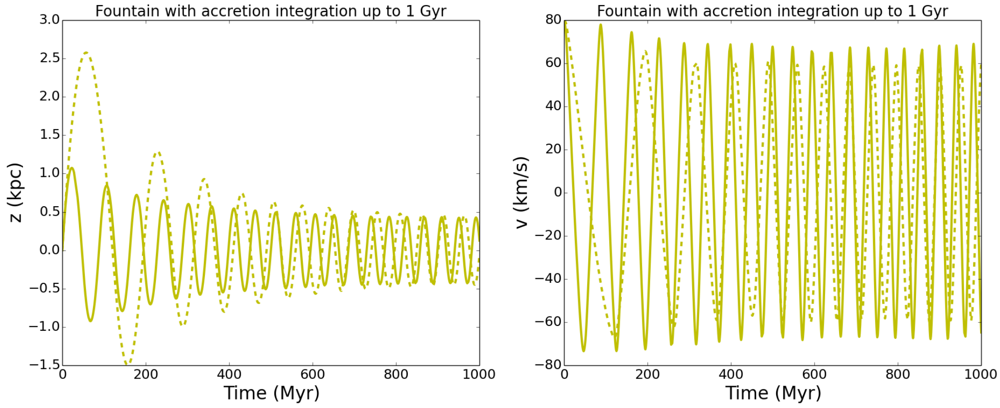

(a) Orbits $z(t)$. **(b)** Vertical velocity $v_z(t)$.

Figure A.3: Fountain orbits and vertical velocities as a function of time in the presence of accretion and of the two-component potential (see Table 2.2). The kick velocity is $v_{\rm kick} = 80$ km s^{-1} and the kick radii are $R_{\rm kick}$ =5 kpc (solid line) and 10 kpc (dashed line).

Realistic galactic fountain

Figures A.4a and A.4b show the orbits and the vertical velocity of particles travelling under the influence of both coronal drag and accretion. Once again, the oscillations are damped, so the amplitudes decrease with time.

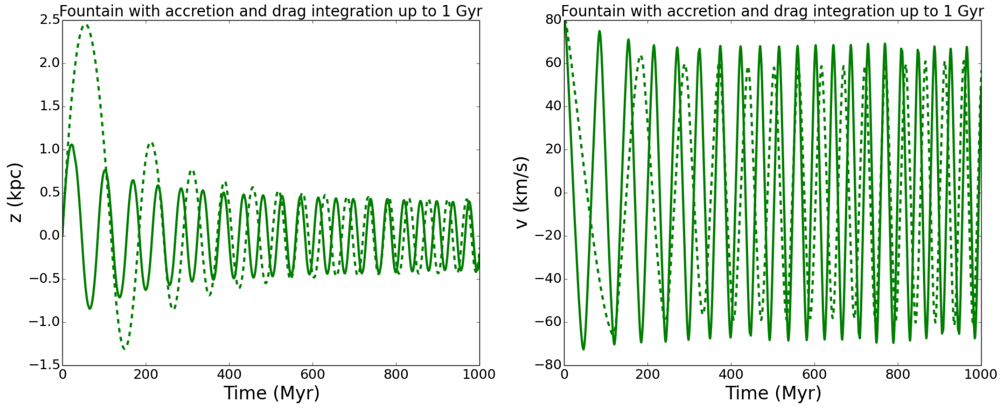

(a) Orbits $z(t)$. **(b)** Vertical velocity $v_z(t)$.

Figure A.4: Fountain orbits and vertical velocities as a function of time in the presence of the drag and the accretion effect in the Milky Way-like potential (see Table 2.2). The kick velocity is $v_{\rm kick} = 80$ km s^{-1} and the kick radii are $R_{\rm kick}$ =5 kpc (solid line) and 10 kpc (dashed line).

Bibliography

Amendt P., Lanza A., Abramowicz M. A., 1989, Astrophysical Journal, 343, 437

Anderson M. E., Bregman J. N., 2010, Astrophysical Journal, 714, 320

Anderson M. E., Churazov E., Bregman J. N., 2016, Monthly Notices of the RAS, 455, 227

Armillotta L., Fraternali F., Marinacci F., 2016, Monthly Notices of the RAS,

Aumer M., Binney J. J., 2009, Monthly Notices of the RAS, 397, 1286

Barnabè M., Ciotti L., Fraternali F., Sancisi R., 2006, Astronomy and Astrophysics, 446, 61

Bilitewski T., Schönrich R., 2012, Monthly Notices of the RAS, 426, 2266

Binney J., Tremaine S., 2008, Princeton University Press, 1, 868

Binney J., Nipoti C., Fraternali F., 2009, Monthly Notices of the RAS, 397, 1804

Birnboim Y., Dekel A., 2003, Monthly Notices of the RAS, 345, 349

Bogdán Á., Forman W. R., Kraft R. P., Jones C., 2013, Astrophysical Journal, 772, 98

Bond J. R., Cole S., Efstathiou G., Kaiser N., 1991, Astrophysical Journal, 379, 440

Boomsma R., 2007, PhD thesis, Kapteyn Astronomical Institute, University of Groningen

Boomsma R., Oosterloo T. A., Fraternali F., van der Hulst J. M., Sancisi R., 2008, Astronomy and Astrophysics, 490, 555

Bregman J. N., 1980, Astrophysical Journal, 236, 577

Bregman J. N., 2007, Annual Review of Astron and Astrophys, 45, 221

Case G. L., Bhattacharya D., 1998, Astrophysical Journal, 504, 761

Cavichia O., Mollá M., Costa R. D. D., Maciel W. J., 2014, Monthly Notices of the RAS, 437, 3688

Chiappini C., Matteucci F., Gratton R., 1997, Astrophysical Journal, 477, 765

Cignoni M., Degl'Innocenti S., Prada Moroni P. G., Shore S. N., 2006, Astronomy and Astrophysics, 459, 783

Collins J. A., Benjamin R. A., Rand R. J., 2002, Astrophysical Journal, 578, 98

Cuddeford P., 1993, Monthly Notices of the RAS, 262, 1076

Dai X., Anderson M. E., Bregman J. N., Miller J. M., 2012, Astrophysical Journal, 755, 107

Dehnen W., Binney J. J., 1998, Monthly Notices of the RAS, 298, 387

Di Teodoro E. M., Fraternali F., 2014, Astronomy and Astrophysics, 567, A68

Fraternali F., Binney J. J., 2006, Monthly Notices of the RAS, 366, 449

Fraternali F., Binney J. J., 2008, Monthly Notices of the RAS, 386, 935

Fraternali F., Tomassetti M., 2012, Monthly Notices of the RAS, 426, 2166

Fraternali F., Oosterloo T., Sancisi R., van Moorsel G., 2001, Astrophysical Journal, Letters, 562, L47

Fraternali F., Oosterloo T. A., Sancisi R., Swaters R., 2005, in Braun R., ed., Astronomical Society of the Pacific Conference Series Vol. 331, Extra-Planar Gas. p. 239 (`arXiv:astro-ph/0410375`)

Freeman K. C., 1970, Astrophysical Journal, 160, 811

Fukugita M., Peebles P. J. E., 2006, Astrophysical Journal, 639, 590

Gatto A., Fraternali F., Read J. I., Marinacci F., Lux H., Walch S., 2013, Monthly Notices of the RAS, 433, 2749

Hernquist L., 1990, Astrophysical Journal, 356, 359

Hodges-Kluck E. J., Miller M. J., Bregman J. N., 2016, Astrophysical Journal, 822, 21

Hulsbosch A. N. M., Wakker B. P., 1988, Astronomy and Astrophysics, Supplement, 75, 191

Iorio G., 2014, Master of Science Thesis, Bologna University, 1, 185

Jaffe W., 1983, Monthly Notices of the RAS, 202, 995

Kaufmann T., Mayer L., Wadsley J., Stadel J., Moore B., 2006, Monthly Notices of the RAS, 370, 1612

Kennicutt Jr. R. C., 1998, Astrophysical Journal, 498, 541

Kereš D., Katz N., Fardal M., Davé R., Weinberg D. H., 2009, Monthly Notices of the RAS, 395, 160

Klypin A., Zhao H., Somerville R. S., 2002, Astrophysical Journal, 573, 597

Lacey C., Cole S., 1993, Monthly Notices of the RAS, 262, 627

Maller A. H., Bullock J. S., 2004, Monthly Notices of the RAS, 355, 694

Marasco A., Fraternali F., 2011, Astronomy and Astrophysics, 525, A134

Marasco A., Fraternali F., Binney J. J., 2012, Monthly Notices of the RAS, 419, 1107

Marinacci F., Binney J., Fraternali F., Nipoti C., Ciotti L., Londrillo P., 2010, Monthly Notices of the RAS, 404, 1464

Marinacci F., Fraternali F., Nipoti C., Binney J., Ciotti L., Londrillo P., 2011, Monthly Notices of the RAS, 415, 1534

Matteucci F., 2012, Chemical Evolution of Galaxies, doi:10.1007/978-3-642-22491-1.

McMillan P. J., 2011, Monthly Notices of the RAS, 414, 2446

Melioli C., Brighenti F., D'Ercole A., de Gouveia Dal Pino E. M., 2008, Monthly Notices of the RAS, 388, 573

Melioli C., Brighenti F., D'Ercole A., de Gouveia Dal Pino E. M., 2009, Monthly Notices of the RAS, 399, 1089

Miller M. J., Bregman J. N., 2015, Astrophysical Journal, 800, 14

Misiriotis A., Xilouris E. M., Papamastorakis J., Boumis P., Goudis C. D., 2006, Astronomy and Astrophysics, 459, 113

Mollá M., Díaz Á. I., Gibson B. K., Cavichia O., López-Sánchez Á.-R., 2016, Monthly Notices of the RAS, 462, 1329

Morras R., Bajaja E., Arnal E. M., Pöppel W. G. L., 2000, Astronomy and Astrophysics, Supplement, 142, 25

Murray N., Rahman M., 2010, Astrophysical Journal, 709, 424

Navarro J. F., Frenk C. S., White S. D. M., 1996, Astrophysical Journal, 462, 563

Neto A. F., et al., 2007, Monthly Notices of the RAS, 381, 1450

Nipoti C., 2010, Monthly Notices of the RAS, 406, 247

Nipoti C., Posti L., 2013, Monthly Notices of the RAS, 428, 815

Olling R. P., 1995, Astronomical Journal, 110, 591

Oosterloo T., Fraternali F., Sancisi R., 2007, Astronomical Journal, 134, 1019

Pagel B. E. J., 2009, Nucleosynthesis and Chemical Evolution of Galaxies

Pezzulli G., Fraternali F., 2016, Monthly Notices of the RAS, 455, 2308

Pezzulli G., Fraternali F., Boissier S., Muñoz-Mateos J. C., 2015, Monthly Notices of the RAS, 451, 2324

Pidopryhora Y., Lockman F. J., Shields J. C., 2007, Astrophysical Journal, 656, 928

Pisano D. J., Barnes D. G., Gibson B. K., Staveley-Smith L., Freeman K. C., Kilborn V. A., 2007, Astrophysical Journal, 662, 959

Putman M. E., Saul D. R., Mets E., 2011, Monthly Notices of the RAS, 418, 1575

Putman M. E., Peek J. E. G., Joung M. R., 2012, Annual Review of Astron and Astrophys, 50, 491

Sancisi R., Fraternali F., Oosterloo T., van der Hulst T., 2008, Astronomy and Astrophysics Reviews, 15, 189

Schmidt M., 1959, Astrophysical Journal, 129, 243

Schönrich R., Binney J., 2009, Monthly Notices of the RAS, 396, 203

Sembach K. R., et al., 2003, Astrophysical Journal, Supplement, 146, 165

Shapiro P. R., Field G. B., 1976, Astrophysical Journal, 205, 762

Spitzer Jr. L., 1956, Astrophysical Journal, 124, 20

Swaters R. A., Sancisi R., van der Hulst J. M., 1997, Astrophysical Journal, 491, 140

Tassoul J.-L., 2000, Stellar Rotation

Wakker B. P., van Woerden H., 1997, Annual Review of Astron and Astrophys, 35, 217

Wakker B. P., Kalberla P. M. W., van Woerden H., de Boer K. S., Putman M. E., 2001, Astrophysical Journal, Supplement, 136, 537

Wakker B. P., et al., 2007, Astrophysical Journal, Letters, 670, L113

White S. D. M., Rees M. J., 1978, Monthly Notices of the RAS, 183, 341

de Vaucouleurs G., 1948, Annales d'Astrophysique, 11, 247

van Albada T. S., Bahcall J. N., Begeman K., Sancisi R., 1985, Astrophysical Journal, 295, 305